HHS Public Access

Author manuscript

Prog Nucl Magn Reson Spectrosc. Author manuscript; available in PMC 2017 February 06.

Published in final edited form as:

Prog Nucl Magn Reson Spectrosc. 2016 February ; 92-93: 18–53. doi:10.1016/j.pnmrs.2016.01.005.

Applications of NMR spectroscopy to systems biochemistry

Teresa W.-M. Fan[*] and **Andrew N. Lane**

Department of Toxicology and Cancer Biology, University of Kentucky, 789 S. Limestone St., Lexington, KY 40506, United States

Teresa W.-M. Fan: twmfan@gmail.com; Andrew N. Lane: andrew.lane@uky.edu

Abstract

The past decades of advancements in NMR have made it a very powerful tool for metabolic research. Despite its limitations in sensitivity relative to mass spectrometric techniques, NMR has a number of unparalleled advantages for metabolic studies, most notably the rigor and versatility in structure elucidation, isotope-filtered selection of molecules, and analysis of positional isotopomer distributions in complex mixtures afforded by multinuclear and multidimensional experiments. In addition, NMR has the capacity for spatially selective *in vivo* imaging and dynamical analysis of metabolism in tissues of living organisms. In conjunction with the use of stable isotope tracers, NMR is a method of choice for exploring the dynamics and compartmentation of metabolic pathways and networks, for which our current understanding is grossly insufficient. In this review, we describe how various direct and isotope-edited 1D and 2D NMR methods can be employed to profile metabolites and their isotopomer distributions by stable isotope-resolved metabolomic (SIRM) analysis. We also highlight the importance of sample preparation methods including rapid cryoquenching, efficient extraction, and chemoselective derivatization to facilitate robust and reproducible NMR-based metabolomic analysis. We further illustrate how NMR has been applied *in vitro*, *ex vivo*, or *in vivo* in various stable isotope tracer-based metabolic studies, to gain systematic and novel metabolic insights in different biological systems, including human subjects. The pathway and network knowledge generated from NMR- and MS-based tracing of isotopically enriched substrates will be invaluable for directing functional analysis of other ‘omics data to achieve understanding of regulation of biochemical systems, as demonstrated in a case study. Future developments in NMR technologies and reagents to enhance both detection sensitivity and resolution should further empower NMR in systems biochemical research.

Graphical abstract

[*]Corresponding author: Tel.: +1 859 218 1028.

8. Uncited reference

[157].

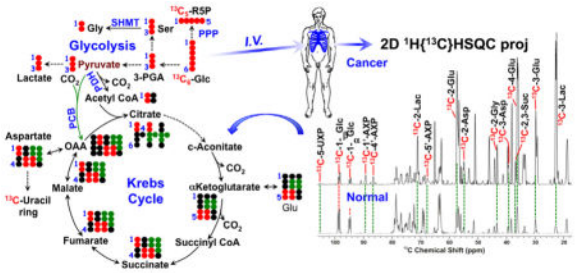

Keywords

Stable isotope tracers; Stable isotope resolved metabolomics; *In vivo* NMR; Hyperpolarization; Metabolic network and flux

1. Introduction

Since the discovery of nuclear magnetic resonance phenomenon in solids and liquids by Bloch and Purcell in 1945 [1,2], NMR spectroscopy has proven to be a powerful and versatile tool for structure elucidation for organic chemists, followed by structural and dynamic determination of macromolecules for the structural biologists, and more recently metabolite profiling for the field of metabolomics. The value of NMR for molecular structural and quantitative analysis is attributable to its element-selective detection and sensitivity of nuclear spin properties to the intra- and inter-molecular environment, as well as to the robust and quantitative nature of NMR measurement. These advantages have made NMR an early choice for metabolite profiling efforts [3–6] and an excellent partner for mass spectrometry (MS)-based metabolite profiling. For example, NMR analysis provides crucial structural parameters including functional groups, covalent linkages, and non-covalent interactions including stereochemistry, which are difficult to acquire by MS methods. On the other hand, high-resolution MS provides molecular formula information, which is an important parameter for NMR structural analysis, particularly when NMR-invisible elements (^{32}S, ^{16}O) are present.

Since the advent of metabolomics development, the superior sensitivity, resolution of MS (including chromatography-based MS and ultra high resolution MS), and its relative ease of data analysis, have contributed to its popularity in steady-state metabolite profiling to date [7–10]. In a PubMed search for metabolomic articles, only 30% of the studies involve NMR analysis. However, for the next-generation metabolomic applications involving stable isotope tracers for robust reconstruction of metabolic pathways and networks, NMR methodologies afford some unique advantages such as detailed positional isotopomer analysis for enriched metabolites, *de novo* structure determination of unknown metabolites (both unenriched and enriched) without the need for standards, and *in situ* analysis of pathway dynamics from cells to whole organisms [11].

This review will focus on the utility of NMR spectroscopy in metabolomics, with an emphasis on NMR applications in stable isotope-enriched tracer research for elucidating biochemical pathways and networks such as those shown in Figs. 18 and 19. The knowledge

gained from this area of research provides a ready link to genomic, epigenomic, transcriptomic, and proteomic information to achieve systems biochemical understanding of living cells and organisms.

2. NMR is a powerful tool for metabolite identification and quantification

2.1. Identification and determination of metabolite structures

NMR has long been employed to determine the chemical structures and conformations of molecules [12,13] and is second only to single crystal X-ray diffraction in determination of absolute stereochemistry. Because of the rich structural information and multinuclear capability of NMR, it is practical to determine the structure of a purified small molecule *ab initio*. In metabolomic applications, however, it is customary to work with complex extracts from cells, tissues or biofluids, which comprise mixtures of hundreds to thousands of molecules covering a very wide range of concentrations. Given the finite practical dynamic range, spectral overlap and the low sensitivity of NMR compared with mass spectrometry (MS), only a subset of metabolites in a sample can be identified and quantified (see below).

In metabolomics-based studies, the goal is to determine as many metabolites as possible ("coverage") that represent many pathways within the vast metabolic network. For example, in a non-targeted metabolomic or biomarker study, one generally determines which NMR or MS spectral features are responding most to the varying conditions [14–21], followed by identification of responsive unknown compounds. For mapping known pathways, identifying all of the intermediates is not essential but is desirable. The reality is that a sizable fraction of the spectral features in metabolomic studies remain unidentified. Although one can quantify relative changes of unknown metabolites by NMR without the need for standards, this provides no useful biochemical information.

The assignment of known metabolites in complex mixtures by NMR can be based on a number of NMR parameters, including chemical shifts and their pH dependence, spin multiplicity, homonuclear and heteronuclear covalent connectivity, and the nuclear Overhauser effect. These aspects have been reviewed by us previously and will not be elaborated here [22,23]. The past decade of development in metabolite databases and database search tools has made it practical to assign metabolites by comparing the NMR spectral features of given samples against those of standards compiled in databases. There are now quite a few public (http://www.eurocarbdb.org/databases/nmr-database; http://www.bmrb.wisc.edu/metabolomics/; http://www.hmdb.ca/; http://www.bml-nmr.org/; http://spin.ccic.ohio-state.edu/index.php/toccata2/index) [24,25] and proprietary (e.g. ChenomX, Bruker) databases available for metabolite assignment purpose. As NMR parameters can be sensitive to pH, temperature, concentration, and ionic conditions [26,27], the sample spectra will need to be acquired under matched conditions with the standard spectra acquired in the databases. This is a crucial aspect of NMR database search for metabolite assignment, since many laboratories differ in their extraction protocols. In addition, at some pH values, the chemical shifts can be degenerate for common metabolites, such as lactate and threonine at neutral pH [26]. Furthermore, 1D databases that rely primarily on chemical shifts can be unreliable and only a limited number of features are identified, due to spectral crowding and lack of more rigorous indication of structural features such as covalently linked partners. For

a group of similar samples in a study, it is advisable to verify assignments using a set of multidimensional NMR experiments that map the carbon skeleton, including TOCSY, HSQC, HMBC and/or a combination of the two (HSQC–TOCSY).

For assigning unknown spectral features, multidimensional NMR is essential [28,29], and may need to include heteronuclear NMR methods based on nuclei other than ^{13}C, such as ^{15}N and ^{31}P. One of the significant advantages of small molecules is that long range heteronuclear couplings are sufficiently large to enable assignments via remote couplings from ^{1}H or ^{13}C to these atoms [30–32], which define much of the covalent atom connectivity. The combination of heteronuclear scalar coupling with chemical shift information is often sufficient to identify a compound by reference to databases and by comparison with compiled chemical shifts of compounds with different functional groups. However, the functional classes of compounds may not be clear unless additional experiments are carried out, for example by pH titration to ascertain the presence of amino or carboxylate functional groups [26].

An additional means of determining functional groups is to make use of derivatizing reagents that target specific functional groups (i.e. chemically selective, or CS, probes). By introducing an enriched atom (^{13}C or ^{15}N) at a strategic position in the CS probe, one can take advantage of the isotope-editing feature of NMR to detect only those metabolites with the targeted function groups (cf. Section 5.3). For example, ^{15}N ethanolamine and ^{15}N cholamine have been introduced to assign carboxylate-containing metabolites via a 2D $^{1}H\{^{15}N\}$-HSQC experiment with high resolving power. The assignment can be based on the functional group and the combined ^{1}H and ^{15}N chemical shifts [33,34]. Other CS probes have been developed by us that select for functional groups including thiols [35] and carbonyls (aldehydes and ketones) [36,37]. The resulting adducts in biological extracts are optimized for both MS analysis, and ^{15}N edited ^{1}H NMR analysis that makes use of long range 2 and 3-bond couplings [31]. This has been illustrated for the carbonyl-selective aminooxy probe, for which 2D $^{1}H\{^{15}N\}$-HSQC spectra (cf. Section 4.1.4) have been acquired for assignment purpose [31].

^{13}C enrichment in metabolites has also been developed for assignment purposes, as ^{13}C-based NMR analysis at natural abundance is time-consuming, particularly for low-level metabolites [38,39]. Several groups have suggested large-scale enrichments with ^{13}C to enhance detection sensitivity, while enabling 2D HCCH-TOCSY or ^{13}C INADEQUATE types of experiments to be carried out in a reasonable time frame [40–43]. A somewhat different approach has been developed by Beecher, called Isotope Ratio Outlier Analysis, or IROA [44] in which two samples are enriched to 5% and 95% with ^{13}C (which requires growing cells for 5 generations in the respective tracers) and mixed for NMR or MS analysis. This strategy enables the assignment of ^{13}C-enriched metabolites due to biosynthesis (instead of artifacts) and determination of the relative concentrations of detected metabolites [45]. While useful for cultured cell-based assignment, IROA applications to tissue-based analysis appear to be limited.

Finally, it should be noted that the experimentally acquired NMR information can be combined with *ab initio* calculations of NMR parameters [46–50] to inform stereochemistry

of metabolites, which can ultimately be confirmed by chemical synthesis of the correct enantiomer for biological testing. This is critical for the correct assignment of metabolite stereoisomers with different biological activity, as illustrated by the observation of the two enantiomers of 2-hydroxyglutarate with different biological functions [51–56].

2.2. Metabolite quantification

2.2.1. Quantification by 1-D NMR—In addition to metabolite identification, 1-D NMR analysis via common pulse sequences such as ^{1}H PRESAT or NOESY is useful for quantification in metabolomic applications by calibrating the areas of metabolite resonances against those of standards with known concentrations. One important advantage of modern NMR for metabolite quantification is its large linear dynamic range and signal response (10^{6}) with a digitizer of 20 effective bits. This often obviates the need for standard curves in NMR analysis, which are commonly required for MS-based quantification. However, it should be noted that despite the high linear dynamic range of NMR digitizers, in practice this can be compromised by the Lorentzian line shape and non-optimal shimming and therefore be considerably lower.

It is practical to use a single standard for both quantification and internal chemical shift referencing without the need for authentic metabolite standards. Common choices of ^{1}H or ^{13}C NMR standards include DSS (2,2-dimethyl-4-silapentane-4-sulfonic acid)/DSS-d_6 (to eliminate the CH_2 signals that can interfere with analysis of some metabolites), or TSP (3-(trimethylsilyl) propanoic acid)/TSP-2,2,3,3,-d_4 for D_2O and tetramethylsilane (TMS) for $CDCl_3$. When metabolite resonances are well-resolved, 1D NMR quantification can be robust if appropriate signal corrections are made for partial relaxation [23]. This is particularly relevant for compounds with singlet resonances, including the reference compounds, where the T_1 values tend to be long [27,57]. We have chosen a recycle time (acquisition time + relaxation delay) of 6 s for 1D ^{1}H NMR analysis, which is a compromise between speed of acquisition or sample throughput and the magnitude of correction needed for partial saturation. Under these conditions, the majority of metabolite resonances are >99% relaxed. However, for the methyl resonances of DSS or TMS where T_1 values are 2–3 s, the resonances may be 5–15% saturated, and require a correction.

There is an often unappreciated problem with employing internal standards for quantifying metabolites in biofluids (e.g. plasma or urine) or extracts that contain appreciable amounts of protein and/or lipids. Their resonances can be broadened significantly by binding to macromolecules, thereby affecting their signal intensity. Fig. 1 illustrates such a problem, where the 1D ^{1}H NMR spectra of a mouse tumor extract are compared before and after treatment with 80% acetone for efficient protein removal. It is clear that signal intensity increased upon protein removal for the internal DSS standard (Fig. 1 inset) and a number of metabolites. The extent of the signal intensity distortion varies for different compounds, ranging from negative change for glutathiones (GSH + GSSG) to high enhancement for glucose and lactate. This is because when mobile metabolites are in exchange with macromolecules, a fraction of the metabolite signal is lost to NMR detection, and the extent of signal distortion depends on the binding strength, exchange dynamics, number of binding sites, and metabolite concentrations. If strong binding occurs, metabolites can be

precipitated along with proteins, which then lead to signal loss, instead of enhancement with protein removal. The problem for distortion of metabolite signal intensity by interaction with macromolecules is exacerbated when CPMG spin-echo pulse trains are used to suppress broad macromolecular resonances. Human serum contains 35–50 mg/mL or 0.5–0.75 mM of albumin, with several binding sites for different metabolites [58]. Additional binding sites can come from several other abundant serum proteins for a total protein content of 60–80 mg/mL [59]. The NMR-detectable metabolites in plasma or serum also depend on dietary history, as dietary components may compete for the same binding sites [60,61]. Moreover, those metabolites (e.g. Ala) that are in fast exchange on the chemical shift timescale may display chemical shifts notably different from those observed in reference databases, giving rise to problems with metabolite assignment.

One way to circumvent the problem of macromolecule-induced signal intensity distortion of internal standards is to implement direct spiking of the metabolite of interest. However, this is impractical for quantifying a large number of metabolites [26], and is still problematic when metabolite interactions with macromolecules are severe. Another alternative is electronic spiking (ERETIC), where a quantified digital signal is added to the spectrum, which does not suffer from any solute interferences and any frequency can be synthesized to avoid spectral overlaps [62]. The main disadvantage appears to be the calibration of such electronic signal against actual metabolite concentration, which depends on a large number of factors. Nevertheless, this is an attractive approach where high absolute quantitative accuracy is not needed.

Signal intensity distortion problems can be greatly reduced by efficient protein and lipid removal, via a combination of extraction with deproteination and delipidation. However, the nature of deproteination via precipitation is important. If the precipitation method also unfolds the proteins, then any tightly bound metabolites will be released, allowing the total amounts of metabolites to be measured. A method that precipitates or removes protein without denaturation (e.g. ultrafiltration) will remove the tightly bound metabolites, leaving only those that were unbound, or in fast exchange on the time scale of the precipitation process to be analyzed. These considerations may in part account for the differential metabolite yield observed for different sample processing techniques [63,64]. Furthermore, some well established protein precipitation methods can lead to destruction of metabolites, especially those using strong acids such as perchloric acid or trifluoracetic acid ([65], Fan, unpublished data).

Macromolecules can also Interfere with metabolite analysis, due to their multiple and broad resonances. These signals can be removed during data acquisition, using for example CPMG pulse trains [66,67]. In practice, these methods differentially distort signal intensities via the lengthy pulse train, do not always eliminate the lipoprotein contributions, and cannot overcome signal intensity distortion due to differential binding.

Another notable issue with 1D ^{1}H NMR quantification of metabolites in metabolomic applications is spectral crowding. Conventional peak integration for quantification purposes can only be applied to well-resolved ^{1}H resonances. Peak fitting or deconvolution assuming a Lorentz-Gaussian lineshape can provide accurate peak areas in crowded region [27,38],

provided that the peak overlapping is not too severe and that the baseline is correctly determined. However, the assumption of a Lorentz-Gaussian lineshape is not always correct for unresolved features, leading to less reliable peak area determination. Multi-dimensional NMR can circumvent this issue by improving spectral resolution. One complication with 2D NMR quantification is that the peak volumes depend on the appropriate transfer functions, in addition to metabolite concentration. Approaches to metabolite quantification using 2D TOCSY and HSQC data have been described that compare peak volumes or heights of target analytes with those of a given standard acquired under identical spectral conditions [69–71], which helps circumvent such complications.

2.2.2. Quantification in 2D NMR—Fractional distribution of ^{13}C or ^{15}N isotopomers can be determined with acceptable precision in 2D ^{1}H TOCSY spectra without the need for standards. This is achieved by integrating the volumes of the two ^{13}C or ^{15}N satellite cross peaks and normalizing to the sum of the volumes of all cross peaks (cf. Fig. 4). We found that this can achieve an accuracy of 5–10% at natural abundance, and better for isolated resonances at higher enrichment [57,72,73]. This level of accuracy is sufficient for metabolic pathway analysis [74].

2.3. Sensitivity of NMR quantification

With modern cryogenically cooled probes, raw proton sensitivity in a 5 mm tube of 0.1% ethylbenzene (EtBz) can be expected to be 6000–8000:1, or 800–1200:1 for 2 mM sucrose in salt-free water, at 14–18.8 T. In practice the sensitivity (signal height compared with root mean square noise level, which is quoted by the instrument manufacturers) may scale linearly with B_0 (Lane, unpublished observations) rather than the more optimistic $B_0^{7/4}$ [75]. By using matched susceptibility plugs such as Shigemi tubes, the volume needed for a 5 mm probe is about 300 μL, or 3 μmol 0.1% EtBz, 0.6 μmol 2 mM sucrose. Thus to reach a signal-to-noise ratio (SNR) of 10:1 in 10 min acquisition, about 0.6 nmol of material are needed under ideal conditions. Significantly lower quantities are needed in smaller diameter coils such as 1.7 mm or even 1 mm diameter (<10 μL sample needed) where a performance boost of up to 2–3-fold for the same amount of material can be expected, despite the considerably poorer filling factor of a very small diameter tube [76,77]. These probes are best suited for analyzing mass limited samples. However, they do not necessarily perform as well when the sample is too concentrated, which may degrade line shape and alter chemical shifts due to high viscosity, high salt and solute–solute interactions.

Compromised cryoprobe performance, particularly at high magnetic field strength, can be expected for biofluids and some tissue extracts with high ionic strengths. These include human serum, which has an ionic strength of approximately 145 mM and an osmolality of ca. 300 mOsMl [78,79]. Based on Bruker NMR specifications, and observed in practice [80], the signal-to-noise ratio for 5 mm cryoprobes at 18.8 T shows a decrease in sensitivity of at least 2-fold on increasing the concentration of NaCl from 0 to 150 mM. Roughly speaking, the sensitivity of a 5 mm cryogenic probe and a conventional room temperature probe are expected to become equal at around 300 mM sodium chloride, and presumably at lower concentrations at ultrahigh field strengths (e.g. 23 T or higher). Such effects are much smaller in small diameter coils, and can be alleviated to some extent by placing a smaller

diameter tube in a larger coil, e.g. 3 mm in a 5 mm probe or a 1.7 mm tube in a 3 mm coil, provided that the increased solute concentration does not degrade the spectral quality through increased viscosity or aggregation.

Sensitivity enhancement for ^{13}C in cryoprobes is better in larger diameter probes than microprobes, if they are optimized for ^{1}H detection, largely because of the poorer filling factor in the outer coil. When ^{13}C direct detection is desired, ^{13}C optimized inner coils give the best performance, albeit at lower sensitivity than ^{1}H optimized indirect detection for the same sample mass.

3. NMR is uniquely suited for tracking stable isotope labeling at specific atomic positions (isotopomer analysis)

The common isotopes for analysis in metabolic NMR are ^{13}C (1.1%), ^{15}N (0.37%) and ^{31}P (100%). Most metabolites contain carbon atoms with directly attached ^{1}H and/or ^{1}H 2–3 bonds apart, which give rise to ^{13}C-^{1}H couplings. ^{13}C-^{1}H coupling constants (J_{CH}) in common linear metabolites typically scale with the ^{13}C chemical shift, which is exploited in some adiabatic decoupling schemes. $^{1}J_{CH}$ ranges from ca. 125 Hz for alkyl methyl groups to >200 Hz for sp^2 aromatic carbons [30,82]. In addition to ^{13}C-^{1}H coupling, ^{13}C-^{13}C coupling is practical to utilize for ^{13}C isotopomer analysis by NMR. For the common amino acids, $^{3}J_{CC}$ and $^{2}J_{CC}$ range from <1 to ca. 7 Hz [30].

Nitrogen atoms can also have directly attached protons, as in amino and amide groups, or can be two or more covalent bonds from a hydrogen atom (e.g. in cholines). However, amino and amido protons can exchange readily in aqueous solution so may require special conditions to observe ^{15}N-^{1}H coupling [13,81]. Phosphorus atoms with directly attached protons (e.g. phosphonates or phosphines) are not usually natural metabolites, while those with more distantly attached protons are common among nucleotides and sugar phosphate metabolites. Thus, detection of ^{13}P-^{1}H interactions in natural metabolites typically uses long-range coupling. Moreover, as C-C, C-N, and C-P bonds are common in metabolites, it is important to consider also ^{13}C-^{13}C, ^{13}C-^{15}N, and ^{31}P-^{13}C couplings for isotopomer analysis.

One of the great advantages of NMR is the ability to determine elements independently by direct detection, or by the influence of one element on another through coupling interactions, which together can be used for an enormous number of isotope-editing experiments to observe specific isotopomer distributions [28,29,83,84].

There are two general approaches to NMR-based isotopomer analysis, direct observation of the nucleus of interest [85], and indirect detection via an attached spectator spin, usually the proton. Direct detection has the advantage that all sites are generally observed, whereas indirect detection infers the presence of a coupled spin that does not have a directly attached proton. Although carbonyl and quaternary carbons can be observed directly, they do not show a significant NOE, cannot be enhanced by one-bond INEPT or DEPT, and typically have long T_1 values, which means that their signals are likely to be substantially attenuated owing to incomplete relaxation. Direct ^{13}C detection also benefits from a wider chemical

shift range than indirect proton detection, which can be important in crowded 1D spectra of extracts.

However, indirect detection is considerably more sensitive than direct detection. For ^{13}C, the SNR advantage of ^{1}H detection over ^{13}C detection is theoretically $4^{5/2} = 32$ for equal numbers of nuclei (and notably higher when comparing CH_3 or CH_2) under fully relaxed conditions, without NOE or INEPT. This advantage decreases to 8–10-fold if maximal NOE or INEPT transfers are included. Indirect detection through one-bond couplings does not observe carbonyl and quaternary carbons, but they can be inferred from their couplings to neighboring carbon atoms or detected through multiple bond couplings by HMBC experiments for example. For small molecules with long T_2 values, indirect detection can make use of small long-range couplings for more versatile analysis [83,86,87]. The advantages of indirect detection for ^{15}N are very much greater than ^{13}C, due to its much lower γ.

In stable isotope tracer studies, tracers enriched in biologically relevant nuclei such as ^{13}C, ^{15}N, or ^{2}H are introduced to cells, tissues, or whole organisms for transformation into various metabolites. Depending on the transformation pathway(s), isotope labels are incorporated into specific atomic position(s) of given metabolites. For example, ^{13}C-2-glucose is metabolized into ^{13}C-2-lactate via glycolysis and into ^{13}C-1-ribose-5-phosphate via the pentose phosphate pathway (PPP). By determining the positions (positional isotopomers) and the number of the stable isotope labels (mass isotopologues) in transformed metabolites, the transformation pathways can be reconstructed with confidence. It is also practical to discern compartment-specific pathways with this approach, which is not possible with steady-state metabolite profiling alone. NMR is excellently suited for positional isotopomer analysis, while MS is tailor-made for mass isotopologue analysis. A number of 1D and 2D NMR methods have been utilized for this purpose, as described below.

It should also be noted that stable isotope enrichment patterns in metabolites are not only essential for reconstructing metabolic networks, but are also fundamental inputs for flux modeling, which depending on the approach may require isotopic steady state, or be compatible with dynamic conditions, as necessitated by many studies *in vivo* (cf. Section 5.2) [88–90,85,91–95].

3.1. Direct observe methods

3.1.1. 1D methods—Both 1D ^{1}H and ^{13}C NMR methods have been employed to analyze for ^{13}C positional isotopomers [96–139]. The covalent coupling network of ^{1}H and ^{13}C atoms in given metabolites gives rise to pairs of satellite peaks in the 1D ^{1}H NMR spectra. The splitting patterns of the satellites depend on the number and positions of ^{13}C atoms present in the metabolite. For example, the methyl (Me) or H-3 resonance of ^{12}C-lactate (no ^{13}C present) is a doublet with no ^{13}C satellites (Fig. 2A). When C-3 or C-2 of lactate is enriched in ^{13}C, a pair each of doublet satellites arises equidistant from the central methyl doublet of ^{12}C-lactate but with different J coupling constants (Fig. 2B). For the lactate isotopomer labeled with ^{13}C at both C-2 and C-3, a pair of doublet of doublet satellites is expected (Fig. 2C), while a pair of doublet of doublet of doublet satellites arises from

uniformly ^{13}C labeled lactate ([U-^{13}C]-Lac) (Fig. 2D). The very similar coupling constants, as shown in the simulation, result in such observed multiplets. The latter pattern is evident in a polar extract of medium obtained from culturing human cancer cells in [U-^{13}C]-glucose (Fig. 2E), which indicates the transformation of [U-^{13}C]-glucose into [U-^{13}C]-Lac via glycolysis.

Despite the much lower sensitivity of detection than ^{1}H NMR, 1D ^{13}C NMR is more commonly employed for delineating different ^{13}C positional isotopomers due to its superior resolution and interpretability of ^{13}C label position(s) based on the spin coupling patterns within the covalent network. For example, ^{13}C enrichment simultaneously at C-3 and C-4, C-1 and C-2, C-2 and C-3, as well as C-1, C-2, and C-3 can be deduced from a 1D ^{13}C NMR spectrum of methylacetone glucose, a chemically modified plasma glucose (Fig. 3A). The ^{13}C positional isotopomers of fatty acyl chains of lipids can be ascertained from the 1D ^{13}C NMR spectrum of a cell lipid extract, as shown in Fig. 3B. The consecutive ^{13}C labeling of terminal (ω) CH_3 and penultimate ω-1 CH_2 ($^{13}CH_3$-$^{13}CH_2$-) and of ω-CH_3, ω-1 CH_2, and ω-2 CH_2 ($^{13}CH_3$-$^{13}CH_2$-$^{13}CH_2$-) are evident, respectively based on the doublet pattern of ω-CH_3 and ω-1 CH_2 and on the triplet pattern of ω-1 CH_2.

3.1.2. 2D methods—2D ^{1}H NMR methods offer even more versatile and rigorous means for positional isotopomer analysis. This is illustrated by ^{1}H-^{1}H total correlation spectroscopy (TOCSY) detection of three different ^{13}C positional isotopomers of glutamate in a ^{13}C-enriched cell extract (Fig. 4B), when compared with the corresponding unlabeled data (Fig. 4A). Namely, three pairs of ^{13}C satellite cross-peaks distributed at equidistance to the cross-peak of Glu-2H to Glu-4H (both ^{12}C-attached, Fig. 4B) indicate the occurrence of ^{12}C-2,4-Glu, $^{13}C_1$-2-Glu, $^{13}C_1$-4-Glu, and $^{13}C_2$-2,4-Glu (structures shown in Fig. 4C) (cf. [22] for additional satellite cross-peak patterns). The TOCSY analysis not only resolves these isotopomers, but also rigorously confirms their identity based on the chemical shifts, covalent connectivity, and ^{1}H-^{13}C coupling constants.

A ^{13}C-edited version of TOCSY, ^{1}H-^{13}C HCCH-TOCSY, enables selective detection of covalently linked ^{1}H's attached to consecutively ^{13}C labeled carbon atoms (cf. Fig. 5E). Fig. 5D [108] illustrates such a 2D spectrum, acquired from the polar extract of a lung adenocarcinoma A549 cell line grown in $^{13}C_6$-glucose under control conditions. Cross-peaks arising from lactate and glutamate isotopomers with ^{13}C labeled at both C-2 and C-3 positions are clearly observed, along with those derived from $^{13}C_5$-1,2,3,4,5-ribose containing uracil nucleotides (UXP). Also shown are the 1D projection spectra of ^{13}C labeled A549 cell extracts obtained from selenite (Se) and control treatments (Fig. 5A and C, respectively), along with the high-resolution ^{1}H NMR spectrum of the control extract (Fig. 5B). Fig. 5C illustrates the ^{13}C editing capacity of HCCH-TOCSY for enhancing the detection of minor ^{13}C labeled components such as glycerophosphocholine (GPC), and unresolved components such as uracil nucleotides (UXP) (denoted by *), which is difficult to ascertain in the unedited spectrum (Fig. 5B). It is clear from the projection spectra (Fig. 5A versus C) that the selenite treatment blocks the synthesis of $^{13}C_2$-2,3-lactate and Glu as well as $^{13}C_5$-ribose-containing UXP, but enhances the production of $^{13}C_3$-1,2,3-glycerol-containing GPC. These data are consistent with reduced glycolytic capacity ($^{13}C_2$-2,3-lactate as marker) and anaplerotic pyruvate carboxylation ($^{13}C_2$-2,3-Glu as marker) (cf. Fig. 18) as

well as increased degradation of phosphatidylcholine lipids (PCL), elicited by selenite (cf. Fig. 17, [108].

3.2. Indirect observe methods

Indirect detection of ^{1}H attached to ^{13}C, ^{15}N, or other NMR-observable heteroatoms presents a far more sensitive means for analyzing labeled positional isotopomers of metabolites than direct detection of the enriched heteroatoms, due to the larger gyromagnetic ratio of ^{1}H (γ_H) than those of the heteroatoms (γ_X). A sensitivity gain of up to 32-fold is to be expected for $^{1}H\{^{13}C\}$ and $^{1}H\{^{15}N\}$ heteronuclear single quantum coherence spectroscopy (HSQC), as the sensitivity gain is proportional to $(\gamma_H/\gamma_X)^{5/2}$ (cf. also [22]). Usable 1D $^{1}H\{^{13}C\}$-HSQC spectra can be acquired with as little as 0.1 to 0.2 mg of dry cell mass (Fan et al., unpublished data), which is currently not achievable with direct ^{13}C detection methods.

3.2.1. 1D methods—We have routinely employed 1D $^{1}H\{^{13}C\}$-HSQC analysis for a quick overview of metabolites labeled with ^{13}C at different carbon positions [98,101–103,105–107,141]. Fig. 6 shows an example 1D $^{1}H\{^{13}C\}$-HSQC spectrum (the first slice of a 2-D experiment, i.e. a 1D ^{13}C-edited proton spectrum) of a polar extract of lung adenocarcinoma PC9 cells grown in $^{13}C_6$-glucose for 24 h. Except for phosphocholine, of which the N-methyl resonance (NMe-PCholine) arises from the naturally abundant ^{13}C (cf. unlabeled versus $^{13}C_6$-glucose spectra), all other metabolites exhibit ^{13}C enrichment at various carbon positions, indicating transformations of $^{13}C_6$-glucose into lactate, Ala (from glycolysis), Glu, Asp, glutathiones (GSH + GSSG) (via the Krebs cycle), Gly (via glycolysis and the Ser-Gly pathway), purine (AXP, NAD^+) and pyrimidine (UXP, CXP, UDPG, UDP-GlcNAc) nucleotides (via the pentose phosphate and nucleotide ring synthesis pathways) (cf. [98,106]).

Similarly, 1D $^{1}H\{^{15}N\}$-HSQC analysis selectively and sensitively detects ^{15}N-labeled adducts of carbonyl-containing metabolites, as shown in Fig. 7. The ^{15}N label is introduced by reacting metabolites such acetone, pyruvate, and sugar aldehydes with an ^{15}N-aminooxy probe, ^{15}N-QDA, to form the oxime adducts (Fig. 7A). The resulting adducts have ^{15}N coupled to metabolite protons at 2 or 3 bond distance with $^{2}J_{NH}$ or $^{3}J_{NH}$ in the 2–3 Hz range [142]. This coupling enables sensitive detection of ^{15}N via its covalently linked ^{1}H by $^{1}H\{^{15}N\}$-HSQC. The ^{15}N editing eliminates interfering signals from unlabeled metabolites, allowing highly selective detection of low abundance carbonyl-containing metabolites such as pyruvate and acetone (cf. unedited ^{1}H versus ^{15}N-edited HSQC; Fig. 7B). It should also be noted that volatile acetone is detected as the ^{15}N-QDA adduct but will be lost via lyophilization in the untreated extract.

3.2.2. 2D methods—Since the development of multichannel high field spectrometers and of a variety of labeling schemes for macromolecules, there is an enormous number of possible experiments that can select for particular groups of atoms via scalar couplings [143–150]. These are important for analyzing metabolite mixtures, where scalar interactions are key to metabolite identification. In particular, isotope editing experiments that rely on scalar coupling between protons and isotopically enriched X-nuclei are most attractive for

profiling labeling patterns of metabolites in mixtures, for which HSQC (or HMQC) is the simplest experiment available. An important side benefit of such experiment is the ability to determine positional isotopomer distributions in multiple isotope-enriched molecules in a complex mixture. For example, the simultaneous presence of ^{13}C at a specific position in ^{15}N-enriched metabolites in a complex mixture can be readily observed using $^{1}H\{^{15}N\}$ HSQC to select for ^{15}N containing molecules, which also give rise to ^{13}C satellites in the ^{1}H dimension of the 2D data [28,81]. A similar scheme could be applied to select ^{31}P-containing metabolites which are enriched in ^{13}C, for example. Moreover, the topology of a ^{13}C or ^{15}N coupled spin network can be defined by appropriate 2D and 3D heteronuclear experiments. Consider a molecule such as lactate, which can have up to $2^3 = 8$ isotopomers when enriched in ^{13}C (cf. Fig. 2). The uniformly enriched isotopomer would show a very characteristic HSQC spectrum, including the 1-bond ^{1}H-^{13}C coupling and distant coupling to C2 and C3 of lactate. Other editing experiments can be performed to better define the coupling partners, such as HMBC (cf. Fig. 10) [28] and HCACO (cf. Fig. 11) [84,151,152] for linking aliphatic protons to ^{13}C-carbonyl carbons, as well as the HACAN triple resonance experiment for detect ^{15}N amino group. The various 2D or 3D experiments that make use of the spin topology pathways of labeled metabolites are depicted for $^{13}C_5$, ^{15}N-glutamate in Fig. 8. Some of these 2D experiments are illustrated below.

2D $^{1}H\{^{13}C\}$-HSQC acquired in high-resolution (HR) mode represent a powerful technique for resolving and identifying ^{13}C-enriched isotopomers, not only for carbons with attached protons but also for quaternary carbons, which are normally not observable by HSQC. 2D HSQC also provides more rigorous resonance assignment than its 1D version, as ^{13}C chemical shifts and coupling patterns can be obtained, in addition to ^{1}H chemical shifts. Fig. 9 illustrates the 2D $^{1}H\{^{13}C\}$-HR-HSQC spectrum (A) of a ^{13}C-enriched A549 cell extract, along with the 1D projection spectrum in the ^{13}C dimension (B) for a better visualization of the ^{13}C-^{13}C coupling patterns. Highlighted are the coupling patterns for the ribose subunit attached to the adenine ring of NAD^+, where the doublet of C-1′, triplet of C-2′, and doublet of C-5′ patterns indicate the presence of $^{13}C_5$-1,2,3,4,5-ribose-containing NAD^+ isotopomer. Also illustrated is the presence of $^{13}C_3$-1,2,3-lactate (Lac), deduced from the triplet pattern of C-2. Even though the carboxylate carbon (C-1) of lactate is normally not observable by HSQC, its ^{13}C enrichment is inferred from the splitting pattern of C-2.

To observe ^{13}C-^{1}H connectivity for carbons with no attached proton(s) (e.g. carbonyls or quaternary carbons) or carbons bonded to heteroatoms (e.g. C-N), 2D $^{1}H\{^{13}C\}$-HMBC (heteronuclear multiple bond correlation spectroscopy) analysis can be performed, as illustrated in Fig. 10. This experiment complements 2D $^{1}H\{^{13}C\}$-HSQC analysis to provide ^{13}C-^{1}H covalent linkages missing from the latter, thereby enabling more rigorous assignment of ^{13}C positional isotopomers of metabolites. For example, the cross-peaks for C-1 to H-3 of Ala and C-5 to H-4 of Glu in the 2D HMBC plot confirm the 1D ^{13}C resonance at 176.5 ppm as C-1 of Ala, and that at 181.9 ppm as C-5 of Glu. The doublet for the C-1 and doublet of doublets for the C-2 resonances of Ala indicates the presence of $^{13}C_3$-1,2,3-Ala, while the doublet for C-5 of Glu arises from $^{13}C_2$-4,5-Glu. $^{13}C_3$-1,2,3-Ala is derived via glycolysis, while $^{13}C_2$-4,5-Glu is synthesized via glycolysis + canonical Krebs cycle (PDH-initiated) from the tracer $^{13}C_6$-glucose (cf. Fig. 10).

For carbonyl-containing metabolites, 2D HCACO analysis reveals ^{13}C carbon linkages to aliphatic protons via ^{13}C–^{13}C coupling. As shown in Fig. 11 for an A549 cell extract, the cross-peak patterns indicate the presence of different ^{13}C positional isotopomers for Asp, Glu, citrate (Cit), lactate (Lac), reduced (GSH) and oxidized (GSSG) glutathiones, and UDP-glucose (UDPG). In particular, the synthesis of $^{13}C_2$-4,5-Glu and $^{13}C_2$-1,2- or $^{13}C_2$-3,4-Asp from $^{13}C_6$-glucose is indicative of transformations via glycolysis, followed by PDH-initiated Krebs cycle activity. The production of $^{13}C_3$-1,2,3-lactate and $^{13}C_2$-1,2-Gly points to glycolysis, and glycolysis plus the Ser-Gly pathway, respectively.

In addition to ^{13}C-edited 2D methods, the 2D ^{13}C-^{13}C INADE-QUATE (Incredible Natural Abundance DoublE QUAntum Transfer Experiment) method [153] can be performed on ^{13}C-enriched extracts of low mg amounts (dry mass) of biological samples, which is normally not practical with unenriched samples. Instead of utilizing the attached ^{1}H for detection, this experiment analyzes ^{13}C-^{13}C one-bond coupling in the carbon covalent network with the direct (F_2) dimension as ^{13}C chemical shift axis and the indirect (F_1) dimension as the double quantum frequency axis. It is therefore a powerful technique for tracing the entire ^{13}C carbon skeleton of individual metabolites. Fig. 12 illustrates the ^{13}C-^{13}C cross-peak patterns for ^{13}C-enriched metabolites in the polar extract of a lung adenocarcinoma PC9 cell line grown in $^{13}C_6$-glucose for 24 h. The cross-peaks of ^{13}C-1 to ^{13}C-2 to ^{13}C-3 of Ala and lactate (Lac), ^{13}C-1 to ^{13}C-2 of Gly, and ^{13}C-4 to ^{13}C-5 of Glu, as well as their splitting patterns unambiguously indicate the presence of $^{13}C_3$-1,2,3-Ala and -lactate, $^{13}C_2$-4,5-Glu, and $^{13}C_2$-1,2-Gly, respectively.

For analysis of metabolites with severely overlapping resonances in a narrow spectral region, as exemplified by sugars and phosphosugars, selective 3D experiments, such as a ^{31}P HSQC–TOCSY experiment, can be employed to resolve and identify the components and their isotopomer distributions. The main impediments to the use of 3D experiments are sensitivity and experiment time, though non-uniform sampling in two indirect dimensions [154], GFT or PR reconstructions [155,156] may make such applications practical in some cases.

4. Sample preparation considerations

4.1. Metabolic quenching

At the time of sampling, metabolism, and thus metabolite profiles, can change quickly if samples are not quenched immediately. A common means for metabolic quenching of biological samples is flash-freezing in dry ice or liquid N_2. Liquid N_2 freezing is far more efficient than dry ice freezing, as it is a liquid rather than solid and has a much colder temperature (−196 °C) than dry ice (−78.5 °C). Slow freezing (even in the 10s of second range) can lead to changes in labile metabolites [158]. This aspect must be considered to minimize sampling artifacts, particularly for metabolically active thick specimens such as brain and liver tissues. For bulk tissue freezing, freeze-clamping in liquid N_2 within seconds is the method of choice for arresting metabolism. Example freeze-clamping devices are shown in Fig. 13. These devices press fresh tissues into 1–2 mm thin layers so that they can be frozen evenly within seconds in between two aluminum plates (with excellent thermal conductivity) pre-equilibrated in liquid N_2 or other cryogens [159]. This process eliminates

differential freezing from the surface to the core of thick tissue specimens with simple immersion in cryogens, which can lead to changes in labile metabolites in response to hypoxia [158].

Metabolic quenching by quick homogenization of bulk tissues in ice-cold 0.6 M perchloric acid (PCA) has been shown to give metabolite profiles comparable to quenching and pulverization in liquid N_2 [160]. Although convenient, this method excludes the possibility of sharing tissues for RNA or DNA extraction for transcriptomic or genomic analysis. The extremely low pH of PCA will degrade acid-labile metabolites such as fructose-2,6-bisphosphate, NAD(P)H, ascorbate, high energy phosphate metabolites, and sugar nucleotides, etc. [65]. The process of removing PCA by titration with KOH or K_2CO_3 is also tedious and time-consuming [65].

For adherent mammalian cells on culture plates, quenching by direct freezing is impractical. Cells need to be cleared from the medium components before quenching, which can be achieved by quickly rinsing cells in ice-cold PBS, followed by solvent quenching in cold acetonitrile (e.g. −20 °C) or methanol (e.g. −80 °C) [65,161]. However, this cell quenching method is unsuited to quenching fast-growing microbes, which requires much quicker manipulation before freezing. Direct whole broth quenching with cold solvents, quenching with cold or hot solvents (e.g. cold 60% methanol, hot 90% ethanol, or −23 °C glycerol-saline) prior to cell separation [162–166], and fast filtration methods [162,163,167] have been developed for such difficult cases. Direct whole broth quenching is quick but has the disadvantage of contaminating low levels of cellular metabolites with medium broth components [167]. Methanol quenching coupled with cell separation can circumvent this problem, but suffers a significant loss (>60%) of cellular metabolites due to non-specific leakage. Use of buffered quenching solvents [164,165,168] or isotonic wash solution coupled with fast filtration [167] has been reported to recover relatively high levels of cellular metabolites.

4.2. Choice of extraction solvent

Extraction buffers for NMR-based metabolomic analysis should meet the following criteria: (1) be readily removable; (2) have low ionic strength; (3) be efficient for inactivation and removal of macromolecules; (4) be non-reactive. In fact, the solvent used for quenching metabolism is invariably a component of the extraction buffer. Perchloric acid (PCA) or trichloroacetic acid (TCA) is often used in the literature to extract polar metabolites while quenching the cell or tissue metabolism by denaturing active proteins [3,4,96,97,106,108,114,169–177]. However, as indicated above, these strong acids can lead to metabolite degradation during extraction, and increase the ionic strength of the final extract. Organic solvent-based extraction methods are now widely accepted for efficient extraction of polar and non-polar metabolites while eliminating proteins by precipitation without increasing the ionic strength of the extract. Varying combinations of methanol, H_2O, acetonitrile, $CHCl_3$, and methyl-tert-butyl ether (MTBE) have been used to quench and extract a wide variety of biological samples from biofluids, cells, to tissues [37,98,101,103–105,142,162–164,167,168,175,178–196]. Most of the solvent-based procedures share commonalities with the Folch method [197], in that they involve separation of aqueous and

water-immiscible $CHCl_3$ layers for simultaneous extraction of polar and non-polar metabolites, with protein precipitates situated in between the aqueous and $CHCl_3$ layers. A more recent method replaces $CHCl_3$ with the less toxic and lower density MTBE, which gives comparable lipid recovery while enabling protein precipitates to be pelleted at the bottom of the extraction tube [194–196]. Such an improvement allows for the development of automation of the extraction process, to greatly enhance sample throughput [195]. We also found that the MTBE method gave comparable polar metabolite profiles by ^1H NMR to those from our $CH_3CN–H_2O–CHCl_3$ method [65] (Fig. 14).

4.3. Selective detection via chemical derivatization

To take advantage of the superior sensitivity of ^1H NMR for selective detection of specific functional groups of metabolites, ^{15}N labeled carboxyl-selective tags such as ^{15}N-ethanolamine [198] or ^{15}N-cholamine [199] have been developed (cf. Fig. 15A for reaction) and demonstrated for $^1H\{^{15}N\}$-HSQC analysis of biofluids. An example spectrum of ^{15}N-cholamine-tagged human serum is shown in Fig. 15B, where a number of amino and organic acids are resolved. The permanent positive charge of the tagged metabolites also enhances their detection by mass spectrometry [199]. Similarly, ^{13}C-formylation of the amine group of metabolites coupled with $^1H\{^{13}C\}$-HSQC analysis has been applied to biofluid analysis for amino metabolites at the low μM range [200]. Reliable quantitation by 2D HSQC is also achievable with this tagging method.

For tagging carbonyl and sulfhydryl functional groups, we have respectively developed QDA (*Q*uaternary ammonium *D*odecyl dimethyl *A*minooxy) [37] and QDE (*Q*uaternary ammonium *D*odecyl dimethyl *E*thyl iodoacetamide) [201] probes. The ^{15}N labeled QDA was employed to tag carbonyl-containing metabolites such as pyruvate (Fig. 16A) in A549 cell extracts to enable their detection by 1D and 2D $^1H\{^{15}N\}$-HSQC via 2-bond ($^2J_{NH}$) or 3-bond ($^3J_{NH}$) $^1H–^{15}N$ coupling [142]. The ^{15}N labeled oxime adducts such as ^{15}N-QDA-pyruvate and ^{15}N-QDA-acetone are clearly seen in the ^{15}N-edited 1D ^1H spectrum (red line, Fig. 16B), while they are overwhelmed or missing (acetone removed by lyophilization) in the unedited ^1H spectrum (black line, Fig. 16B). The 2D HSQC spectrum resolves quite a few more ^{15}N-QDA adducts including dihydroxyacetone-3-phosphate (DHAP) and ribose (Fig. 16C).

4.4. Metabolite detection without extraction

The non-invasive nature of NMR analysis has enabled metabolite profiling of intact tissues without extraction. This involves the High Resolution Magic Angle Spinning (HRMAS) approach, where tissue sample (mg quantities) is placed in a small rotor at 4 °C and spun at the magic angle at ca. 4 kHz during NMR measurements. Standard water suppression techniques such as NOESY, presaturation or CPMG are applied, so 2D rotor synchronized adiabatic TOCSY and $^1H/^{13}C$ HSQC experiments can be implemented [202]. The averaging of the spatial variation in magnetic susceptibilities is often excellent, giving very high quality 1D and 2D ^1H NMR spectra for a wide variety of tissues [203–212].

The main advantages of HRMAS analysis are that no tissue extractions are required and that the amount of free metabolite is determined. There are however several uncertainties that

limit HRMAS applications in tracer-based studies. As the excised tissue is frozen, thawed, squeezed and sealed in a tight space with no O_2 and nutrient supply nor provision for removing waste products, the biochemical integrity of the tissue may be severely compromised. It is also impractical to observe physiologically relevant metabolic activity under such stressful conditions, most notably hypoxia and acidosis. Furthermore, HRMAS quantification may be compromised by variable metabolite interactions with macromolecules. To date, HRMAS has not been applied in tracer-based pathway mapping studies.

5. Applications of NMR to metabolomics

5.1. Metabolite profiling studies

The focus of the present review is on the use of stable isotope tracers in conjunction with NMR analysis for advancing metabolomic understanding. This is a relatively less popular area of NMR applications. The majority of NMR applications in metabolomics research are metabolite profiling-based, and do not involve tracer use. These have been extensively reviewed elsewhere [19,213–222] and will not be elaborated here. We emphasize that employing proper sample preparation techniques (cf. Section 4) is essential to realizing the highly reproducible nature of NMR-based metabolite profiling, compared with any other technique. For NMR profiling of biofluids, high reproducibility is readily achieved if standardized protocols are followed [49]. We have also observed good reproducibility of NMR analysis of cell and tissue extracts with standardized procedures [26,223,224].

5.2. Stable isotope tracer studies

The concept of linear metabolic pathways is more didactic than realistic, based on cursory examination of established metabolic charts (e.g. http://www.sigmaaldrich.com/content/dam/sigma-aldrich/docs/Sigma/General_Information/metabolic_pathways_poster.pdf). For example, glycolysis may be defined as the linear path of glucose oxidation to pyruvate (Emden-Meyerhof-Parnas pathway). However, essentially all of the glycolytic intermediates also participate in multiple other pathways, such as lactic fermentation, the Krebs cycle, Ala metabolism (pyruvate), the pentose phosphate pathway (glucose-6-phosphate or G6P, fructose-6-phosphate or F6P, and glyceraldehyde-3-phosphate or GAP), glycogen synthesis (G6P), hexosamine biosynthesis (F6P), fructose metabolism (F6P), regulation of glycolysis (F6P via fructose-2,6-bisphosphate), lipid synthesis (DHAP), serine and Gly synthesis (3-phosphoglycerate or 3PGA), to name just a few (cf. Figs. 18 and 19). Such redundancy of pathway participation is the norm rather than an exception, with Glu as the champion that can participate in some 55 different pathways. Multiple parallel and sequential pathways in the biosynthesis of complex metabolites are common, as exemplified by UDP-hexosamine and nucleotide biosynthesis [90,225,178]. Profiling metabolite content by NMR and/or MS methods can provide an overview of the metabolic status of given biological systems. However, this information is grossly insufficient in resolving the intersecting metabolic networks that underlie the steady-state metabolite changes (cf. Fig. 2in Ref. [11]), nor can it provide the network dynamics that are important for deciphering metabolic regulation.

The use of isotopically enriched tracers is indispensible for elucidating metabolic pathways and pathway dynamics. Due to the high sensitivity and ease for detection of radioactive metabolites, the radiolabeled tracer approach has been used extensively in life sciences for probing metabolic reactions and pathways since its development in the 1950s [226,227]. However, the hazardous nature of radiochemicals adds undesirable experimental complications, and is unsuited for research use in human subjects. Another important disadvantage is that except for ^{3}H, radionuclides are NMR-silent, which compromises the opportunities for the use of NMR in the analysis of isotopically enriched metabolites labeled at different atomic position(s) (i.e. positional isotopomers). The label position(s), together with the number of isotope labels in metabolites (mass isotopologues) is crucially important for robust reconstruction of metabolic pathways and networks [11].

Despite the demonstration of stable isotope use in metabolic research since the early 1900s [228], stable isotope tracers were not widely employed in tracing metabolism until the development of metabolomics techniques. This is at least in part due to the cost of the tracers [229], and challenges in detecting stable isotope-labeled metabolites. The important advantage of the stable isotope tracer approach is that biologically relevant stable isotopes including ^{13}C, ^{15}N, and ^{2}H are NMR active. ^{13}C and ^{15}N in particular can be readily detected using a wealth of direct and indirect detection NMR methods, thanks to the past decades of development in biological NMR [230,143,144,146,148,231–233,229]. Not only the sensitivity and resolution, but also the capacity for structure elucidation, of NMR analysis have improved tremendously, such that comprehensive ^{13}C or ^{15}N labeling patterns of a large number of metabolites can now be ascertained using as little as a sub mg quantity of dry cell or tissue biomass or low μL of biofluids. These NMR advancements, together with revolutionary advances in biological mass spectrometry, have changed the landscape for the use of isotope tracers in metabolic research, with stable isotope tracers now preferred over radiotracers. We will illustrate with some recent studies how NMR in combination with stable isotope tracers has been applied to systematically uncover new metabolic knowledge. It should be noted that these studies are meant as examples, instead of a comprehensive review of the literature.

5.2.1. In vitro measurement

5.2.1.1. Cell-based tracing: The bulk of the stable isotope tracer-based metabolic studies on cell systems have involved ^{13}C labeled metabolite analysis, using both direct and indirect detection methods. ^{13}C-glucose labeled at different positions has been the predominant tracer used in different cell-based studies. One study utilized ^{1}H NMR analysis coupled with 1-$^{13}C_1$-, 2-$^{13}C_1$-, or 6-$^{13}C_1$-glucose tracers to track the time course production of ^{13}C-Ala and -lactate isotopomers in the medium of continuously cultured hybridoma cells in a chemostat. This information was then used to model glucose fluxes through glycolysis, the Krebs cycle, and the pentose phosphate pathway (PPP). The metabolic flux analysis revealed that 20% of the glucose consumed was metabolized via the oxidative branch of the PPP, anaplerotic pyruvate carboxylation was negligible, and malic enzyme flux that supports fatty acid biosynthesis was about 10% of the glucose uptake rate. These data indicate a higher biosynthetic rate of continuously growing cells in a chemostat than adherent cells grown in

perfused hollow-fiber bioreactors, thereby contributing towards improved bioengineering of glucose metabolism in mammalian cells [234].

Uniformly ^{13}C labeled glucose (U-$^{13}C_6$-glucose) coupled with ^{13}C NMR has been employed to track mitochondrial Krebs cycle metabolism in insulinoma cells. The existence of two separate pools of pyruvate was uncovered based on ^{13}C isotopomer analysis; one pool involved pyruvate oxidation via acetyl CoA formation, and the other exchange with the Krebs cycle intermediates or pyruvate cycling [111]. The latter pool was responsive to glucose-stimulated insulin secretion. Such compartmentalized metabolic pathways for regulating insulin release would be very difficult to uncover without the aid of stable isotope tracers and ^{13}C isotopomer analysis.

^{13}C NMR isotopomer analysis of INS-1 cells treated with U-$^{13}C_6$-glucose or U-$^{13}C_6$-Leu revealed a similar contribution of three different anaplerotic pathways under basal glucose treatment, including pyruvate carboxylation (PC) of pyruvate derived from glucose, non-glycolytic sources, and Gln oxidation. When exposed to high glucose (15 mM) tracer but not to Gln addition, PC flux increased several fold and was associated with increased insulin secretion. These data enabled the authors to conclude that anaplerotic pyruvate carboxylation, but not anaplerotic Gln oxidation, plays a major role in modulating insulin secretion [235].

^{13}C NMR coupled with various ^{13}C labeled glucose, acetate, and glutamate tracers was employed to probe metabolic trafficking between astrocytes and neurons, which is essential to neuronal functions. The NMR-based ^{13}C isotopomer analysis helped delineate the modulation of the glutamate-glutamine cycle between astrocytes and neurons by pyruvate cycling in astrocytes, and the Ala-lactate shuttle between astrocytes and neurons. These metabolic exchange processes enable ready supply of neurotransmitter Gln to neurons while maintaining carbon and nitrogen balance between the two cell types [236].

To explore how lithium chloride (a long-established therapeutic for bipolar disorder) can impact glial and neuronal metabolism as well as metabolic trafficking between them, we employed $^{1}H\{^{13}C\}$-HSQC NMR and GC–MS coupled with a U-$^{13}C_6$-glucose, $^{13}C_1$-3-lactate, and $^{13}C_2$-2,3-Ala tracer approach [106]. We found that astrocytes grown in U-$^{13}C_6$-glucose released not only ^{13}C-lactate but also significant amounts of ^{13}C-Ala, -Gln, and -citrate into the culture media, and that this process along with pyruvate carboxylase (PCB)-initiated Krebs cycle activity was enhanced by the lithium treatment. The excretion of the latter metabolites is not commonly observed in other mammalian cells. We then showed that neurons had a high capacity for metabolizing externally supplied $^{13}C_1$-3-lactate and $^{13}C_2$-2,3-Ala and that lithium enhanced the neuronal metabolism of $^{13}C_1$-3-lactate via PCB-initiated Krebs cycle activity. These findings suggest that lithium's therapeutic efficacy may be associated with its ability to improve metabolic trafficking to support the Gln–Glu cycle between astrocytes and neurons as well as neuronal energy metabolism. Without the use of ^{13}C tracers and detailed ^{13}C-isotopomer analysis by NMR, it would not be feasible to uncover the lithium-enhanced PC pathway and intercellular interactions between astrocytes and neurons.

We also applied various 1D and 2D NMR techniques to decipher the anti-cancer action of selenite in U-$^{13}C_6$-glucose-grown lung cancer cells [108]. Detailed ^{13}C labeling patterns of metabolites were systematically determined by NMR methods coupled with GC–MS analysis and used to reconstruct metabolic networks perturbed by the selenite treatment. This information was used to deduce the dysregulation of individual enzyme genes by interrogating the transcriptomic data acquired in parallel (Fig. 17). Such integration of metabolomics and transcriptomics information (Metabolomics-Edited Transcriptomics Analysis or META) can greatly facilitate the functional annotation of transcriptomic data, while enabling the discovery of specific gene expression changes that govern metabolic perturbations elicited by the stressor without prior knowledge (see also Section 6).

By employing U-$^{13}C_6$-glucose tracer, 2D ^1H TOCSY NMR, and high-resolution Fourier transformion cyclotron resonance mass spectrometric (FT-ICR-MS) analyses [180], we measured the time course of ^{13}C incorporation into UDP-N-acetyl-D-glucosamine (UDP-GlcNAc) in prostate cancer Ln3CaP-LN3 cells, which is a key precursor for O- and N-linked glycosylation of proteins that modulate a number of cellular processes such as protein targeting to organelles and nutrient sensing. The time course data were modeled using a *G*enetic *A*lgorithm for *I*sotopologues in *M*etabolic *S*ystems (GAIMS) to deconvolute ^{13}C mass isotopologue data into ^{13}C positional isotopomer species, from which time-dependent ^{13}C incorporation into individual metabolic units (e.g. glucosamine, acetyl, uracil, and ribose) of UDP-GlcNAc was resolved. This in turn yielded the fractional contribution of glycolysis, the Krebs cycle, pentose phosphate pathway, hexosamine biosynthetic pathway, and pyrimidine biosynthetic pathway to UDP-GlcNAc synthesis via GAIMS modeling. Such information will greatly facilitate flux modeling of metabolic networks, without achieving the isotopic steadystate required by most current approaches [89,237].

We then employed both U-$^{13}C_6$-glucose and U-$^{13}C_5$, $^{15}N_2$-Gln tracers coupled with 2D ^1H TOCSY and $^1H\{^{15}N\}$-HSQC analyses to track *de novo* synthesis of nucleotides and RNA in lung cancer A549 cells. We found that Gln is preferred over glucose for pyrimidine ring synthesis, via the synthesis of Asp via the Krebs cycle, and that ^{13}C incorporation from glucose into total RNA is a major sink for nucleotides during cell proliferation. We further demonstrated that an anti-cancer Se agent (methylseleninic acid) inhibits nucleotide turnover and incorporation into RNA, which underlies its toxicity in cancer cells [178].

Using U-$^{13}C_6$-glucose and U-$^{13}C_5$,$^{15}N_2$-Gln tracers and the *S*table *I*sotope-*R*esolved *M*etabolomics (SIRM) approach, the modulation of oxidative glucose and Gln pathways by a prominent oncogene *c-MYC* and hypoxia was investigated in a MYC-inducible human Burkitt lymphoma P493 cell model [98]. The $^1H\{^{13}C\}$-HSQC NMR analysis of labeled isotopomers helped elucidate the functional role of *c-MYC* in sustaining cell survival and proliferation via a novel glucose-independent Krebs cycle oxidation of Gln under hypoxia and glucose deprivation. Such understanding revealed the promising potential for employing glutaminase (a key enzyme in Gln oxidation) inhibitors for anti-cancer therapy.

5.2.1.2. Tissue-based tracing: The use of a $^{13}C_1$-2-acetate tracer coupled with 1D ^{13}C or 2D $^1H\{^{13}C\}$-HMQC-TOCSY analysis of extracts enabled *ex vivo* distinction of the flux through the mitochondrial Krebs cycle (V_{TCA}) from that of the exchange (V_x) between the

mitochondria and the cytoplasm in tracer perfused rat hearts [238]. Both NMR methods gave comparable V_{TCA} and V_x (denoted respectively by Asp or Glu formation from OAA or αKG transamination) under control and aminooxyacetate (AOA, a transaminase inhibitor) treatment. However, the inclusion of ^{13}C malate isotopomer data markedly improved the confidence limit for V_x determination by HMQC-TOCSY analysis, which also provides higher sensitivity of detection than the 1D ^{13}C method. This study illustrates the feasibility of flux analysis of compartmentalized metabolic processes *ex vivo* in functioning organs.

By infusing $^{13}C_1$-2-glucose into live rats, followed by extract analysis of dissected cortical and hippocampal tissues using 1D $^1H\{^{13}C\}$ NMR, Chowdhury et al. were able to ascertain the action mechanism of an anti-depressant drug riluzole in rat brains [239]. The changes in ^{13}C isotopomer patterns of Glu, Gln, and γ-aminobutyrate revealed the enhancing effect of riluzole on neuronal oxidation of glucose via both PDH and PC-mediated Krebs cycle, as well as on Gln/Glu cycling between neurons and glia. It should be noted that total metabolite levels were not altered by the riluzole treatment, which means that it would be impractical to resolve the action of riluzole by metabolite profiling without the aid of the tracer approach. This study also demonstrate the power of NMR-based ^{13}C isotopomer analysis in resolving *in vivo* complex interactions of metabolic networks across different compartments.

In a SIRM study with a bolus injection of U-$^{13}C_6$-glucose into SCID mice, we compared the time course kinetics of ^{13}C incorporation into various metabolites in different mouse organs using a combination of 1D ^1H, $^1H\{^{13}C\}$-HSQC, high-resolution 2D $^1H\{^{13}C\}$-HSQC-TOCSY (for resolving ^{13}C coupling patterns), and GC–MS analyses [105].We found evidence for a high level of pyruvate carboxylation in brain, heart, and liver, which is consistent with their strong PC protein expression. Different organs also differed substantially in their capacity to synthesize Gln/Glu from glucose, with brain, heart, and liver among the highest. This is consistent with the presence of a Gln/Glu cycle, a high demand for Gln as neurotransmitter in brain tissues, and liver being the primary organ for Gln synthesis. We further compared the ^{13}C labeling patterns of metabolites in tumorous lung (orthotopically implanted with human lung cancer PC14PE6 cells) versus paired normal lung from the same mouse. We found evidence for enhanced glycolysis, increased Krebs cycle activity (both PDH and PC-initiated), and Gly biosynthesis in the tumorous lung, which is consistent with the metabolic reprogramming determined for human lung cancer tissues *in vivo* [97,107]. However, the buildup of the glucose tracer differed between the mouse xenograft and human lung tumors, with the former accumulated but the latter depleted relative to the paired normal lung. These metabolic insights gained from the SIRM approach are valuable in delineating the fidelity of the mouse model in reporting human tumor metabolism.

In a separate SIRM study of transgenic tumor mouse models, we compared the metabolic reprogramming elicited by oncogenes *c-MYC* and *MET* in liver and lung using U-$^{13}C_6$-glucose and U-$^{13}C_5$,$^{15}N_2$-Gln as tracers coupled with 1D ^1H, $^1H\{^{13}C\}$-HSQC, and GC–MS analyses [240]. We found that accelerated glycolysis is not always associated with tumorigenesis, and glucose and Gln metabolism depends not only on the oncogenic genotype but also on the tissue context. *C-MYC*-induced liver tumors exhibited increased glucose and Gln catabolism, while *MET*-induced liver tumors synthesized Gln from glucose.

These reprogrammed events were associated with differential protein expression of Gln synthetase (Glu and glutaminase 1 (GLS1). In contrast, *C-MYC*-induced lung tumors had enhanced Glul and GLS1 expression, and accumulated Gln. We further showed that a GLS1 inhibitor killed cells that overexpressed *c-MYC* and catabolized Gln. Such understanding of oncogene- and tissue-dependent metabolic reprogramming is valuable in designing synergistic strategies for cancer therapy.

In two SIRM studies of human non-small cell lung cancer (NSCLC) *in situ*, we employed bolus infusion of U-$^{13}C_6$-glucose into NSCLC patients, followed by surgical resection of the cancerous (CA) and the surrounding non-cancerous (NC) tissues for extraction, and different 1D/2D NMR and MS analyses of the paired tissue extracts [97,107]. Based on the ^{13}C labeling patterns of various metabolites, We found that CA tissues were more active in metabolizing glucose into lactate, the Krebs cycle metabolites, glutathiones, one carbon metabolites, and nucleotide ribose/rings that their NC counterparts, which is consistent with the activation of glycolysis, the Krebs cycle, pentose phosphate pathway, glutathione biosynthesis, and nucleotide biosynthesis (Fig. 18). In particular, we uncovered enhanced pyruvate carboxylase-mediated anaplerosis in 59 patients studied, while there was no evidence for the activation of glutaminase-mediated anaplerosis. We then demonstrated that PCB expression was crucially important for lung cancer cell growth both *in vitro* and *in vivo* in mouse xenografts [107]. These two studies not only illustrate the feasibility of probing human tumor metabolism in the native tumor microenvironment (TME), but also reveal novel reprogrammed metabolic events vitally important for NSCLC development.

We also explored the utility of *ex vivo* culturing of thin tissue slices (pioneered by O. Warburg [241]) in comparison with *in situ* human studies for reprogrammed lung cancer metabolism [107]. These freshly prepared paired CA and NC lung tissue slices have the advantage of maintaining the 3D architecture of the TME without systemic influences, while enabling flexible treatments with various tracers and/or physical/chemical stressors. In addition, since CA and NC tissues of the same patient are compared, interferences from genetic, physiological, and/or environmental factors that can contribute to metabolic distinction are eliminated. Fig. 19 illustrates how 1D $^1H\{^{13}C\}$-HSQC analysis of paired CA and NC lung tissue extracts can be used to delineate metabolic reprogramming in *ex vivo* CA lung tissues that recapitulates *in vivo* metabolic reprogramming in lung cancer acquired from patient studies described above. We then employed this *ex vivo* system for investigating the metabolic perturbations elicited by an experimental LDHA inhibitor using U-$^{13}C_6$-glucose and U-$^{13}C_5$,$^{15}N_2$-Gln as tracers [101]. We confirmed the on-target action of this inhibitor, i.e. blocking lactate synthesis, while revealing the unexpected action of inhibiting glutaminolysis in human lung cancer tissues.

Human glioblastoma (GBM) metabolism was studied by employing continuous infusion of U-$^{13}C_6$-glucose into individual patients, followed by surgical resection of tumor tissues and 1D ^{13}C NMR analysis of the tissue extracts [242]. The authors found that GBM actively metabolized glucose via glycolysis, the Krebs cycle initiated by both canonical PDH and anaplerotic PC, *de novo* Gln biosynthesis, and glycine biosynthesis. They also found that <50% of the acetyl CoA pool (deduced from the ^{13}C positional isotopomer patterns of Glu) was derived from blood-borne U-$^{13}C_6$-glucose, which is unexpected based on the high

demand of brain tissues for glucose. These results suggest that important source(s) other than glucose contribute to brain tumor bioenergetics. The study also demonstrates a practical means for probing the metabolic functions of human brain tumor grown in its native microenvironment.

5.2.2. In vivo spectroscopic measurements—A unique combined advantage of NMR lies in its non-invasive nature along with the capacity for structure elucidation, which makes it excellently suited for tracking metabolic transformations in real time. Such use of NMR can provide detailed kinetics of metabolic pathways using only a single sample, which eliminates sample-to-sample variation while greatly reducing the cost and labor involved. Most importantly, *in vivo* or *ex vivo* NMR enables metabolic reactions and their intracellular compartmentation to be probed directly in tissues or whole organisms, including human subjects, in a tissue-specific manner, which cannot be achieved by any other analytical approach. The more recent development of hyperpolarized NMR methods further enhances ^{13}C NMR's utility in real-time kinetic measurement of specific metabolic reactions *in vivo*. The following examples illustrate the power of *ex vivo* and *in vivo* NMR applications in gaining metabolic insights.

5.2.2.1. Non-hyperpolarized applications

5.2.2.1.1. Cell studies: *In vivo* NMR studies have been performed on live cells ranging from bacteria, yeast, to mammalian cells to investigate *in situ* specific enzyme reaction kinetics [243], protein structures and conformations [244], or metabolic pathways [245]. In the early studies, microbial cell suspensions were commonly investigated under oxygen deficient conditions. Subsequently, a number of means for maintaining cells under more physiologically relevant conditions were explored for *in vivo* NMR applications [246]. For example, 1D ^{13}C NMR was employed to track the metabolism of $^{13}C_1$-3-fructose in the suspension of a new strain of lactic acid bacteria, where fructose catabolism to mannitol via fructose-6-phosphate and mannose-1-phosphate, to acetate via the heterofermentative pathway, and to lactate via glycolysis was delineated [245].

$^{13}C_1$-1-glucose tracer and 1D ^{13}C NMR were employed to measure the *in vivo* reaction kinetics of aldolase and triosephosphate isomerase, which are key to ^{13}C incorporation into $^{13}C_2$-1,6-fructose-1,6-bisphosphate (FBP) by catalyzing the production and exchange between glyceraldehyde-3-phosphate (GAP) and DHAP, in suspensions of *Escherichia coli* [247] and yeast cells [248]. Upon reoxygenation of an anaerobic *E. coli* cell suspension, the time course appearance of ^{13}C-Glu at C2, 3, and 4 positions indicated that glucose carbon entered the Krebs cycle mainly through acetyl CoA [247].

Using a membrane-cyclone-reactor system, Hartbrich et al. tracked the pathway dynamics of Lys biosynthesis in *Corynebacterium glutamicum* from $^{13}C_1$-6-glucose via the time course buildup of ^{13}C labeled pathway metabolites such as lactate, Glu and succinate, in addition to the final Lys product. *C. glutamicum* is an important microbe engineered for industrial Lys production. The *in vivo* kinetic buildup of these metabolites provides key information for evaluating flux distribution through two different Lys synthetic pathways, the classical succinyl-diaminopimelate pathway and the diaminopimelate dehydrogenase bypath [249].

Tholozan et al. studied ethanol metabolism in a strict anaerobe *Clostridium neopropionicum* by measuring the time course buildup of ^{13}C-1-acetate, ^{13}C-2-propionate, ^{13}C-2-propanol, and ^{13}C-3-butyrate from $^{13}C_1$-1-ethanol tracer using 1D ^{13}C NMR [250]. They were able to propose a reaction sequence from ethanol to propionate and propanol via the acrylate pathway based on the *in vivo* NMR data, and subsequently confirmed this pathway by assaying the specific enzymes involved in the pathway in cell-free extracts.

The metabolism of L-$^{13}C_1$-3-lactate was investigated using ^{1}H NMR in superfused biofilm of *Shewanella oneidensis* [251]. The ^{13}C labeled to unlabeled ratio of L-lactate and the acetate product suggested preferential metabolism of D-lactate over L-lactate, which is consistent with the genomic data on the presence of the D-lactate dehydrogenase gene. However, no genes for L-lactate dehydrogenase, D-lactate transport system, or lactate racemase were found in the *S. oneidensis* genome, which raises the question as to how L-lactate is metabolized. This study demonstrates the feasibility of tracking metabolic dynamics of low abundance microbial biofilm *in situ*, whose metabolism can respond rapidly to environmental gradients, thus affecting microbial resistance to antibiotics. It would be impractical to capture the temporal and spatial dependence of metabolic changes in biofilm organisms using the *in vitro* extraction approach.

DeBerardinis et al. employed a two-stage ^{13}C tracer treatment with real-time ^{13}C NMR measurement to investigate the metabolic dynamics that support the fatty acid biosynthesis required for cell proliferation in live human glioblastoma cells grown in a porous microcarrier [129]. $^{13}C_2$-1,6-glucose was administered first, followed by $^{13}C_1$-3-Gl,n so that the time course kinetics of glucose and Gln metabolism via glycolysis, the Krebs cycle, glutaminolysis, and fatty acid biosynthesis were tracked. They found that glioblastoma cells actively synthesize fatty acyl chains of lipids from glucose carbons, and that Gln further enhances this activity. This Gln effect was ascribed to active glutaminase-initiated glutaminolysis in glioma cells that helped replenish the Krebs cycle intermediates and generate NADPH (via the malic enzyme pathway) required for fatty acid biosynthesis. They also concluded that the pyruvate carboxylase-initiated anaplerotic pathway was suppressed in glioblastoma cells, even though this pathway is highly active in the primary astrocytes, as described in Section 5.2.1.1.

A colon cancer cell line (HCT-116) was grown in microcarrier beads with serial administration of $^{13}C_1$-1-glucose and $^{13}C_1$-6-glucose tracers to measure flux through glycolysis and the pentose phosphate pathway (PPP) using 1D ^{13}C NMR [252]. The authors found that close to 12% of the glucose supplied enters PPP, ca. 7% of the glucose utilized is recycled to glucose via PPP, and 4.7% of the glucose metabolized via PPP forms lactate. Such a high rate of recycling via PPP suggests a significant contribution of PPP to cellular NADPH production.

5.2.2.1.2. Ex vivo tissue studies: A ^{13}C-bicarbonate tracer coupled with 1D ^{13}C NMR and ^{13}C saturation transfer experiments was employed to follow *ex vivo* bicarbonate uptake and carbonic anhydrase activity in excised maize root tips during K_2SO_4 treatment [109]. K_2SO_4 stimulates dark inorganic carbon fixation in plant tissues. K_2SO_4 was found to have little effect on bicarbonate uptake, intracellular bicarbonate concentration, or carbonic

anhydrase activity. The measured carbonic anhydrase activity was far greater than that of the phosphoenolpyruvate carboxylase (PEPC) (measured by ^{14}C-bicarbonate); the latter activity was enhanced by K_2SO_4. Together, these results suggested that *in vivo* PEPC activation by ion uptake is not mediated by substrate availability. This study illustrates the power of ^{13}C tracer-based NMR analysis in determining *in vivo* enzyme activity and substrate uptake/availability, which are impractical to acquire by any other means.

Probing metabolic interaction between symbiotic vesicular-arbuscular mycorrhizal (VAM) fungi and a plant host (leek roots) represents another valuable application of *ex vivo* NMR including 1D ^{13}C NMR and ^{31}P NMR [253]. Time course ^{13}C incorporation from $^{13}C_1$-1-glucose into trehalose, glycogen, and mannitol (VAM metabolites) and sucrose (host root metabolite) was acquired in this study. The presence of VAM greatly reduced sucrose synthesis in the host roots despite markedly enhanced glucose consumption. This fungal modulation of host metabolism was not related to improved uptake of phosphate (as evidenced by polyphosphate buildup). Likewise, host interaction with VAM curtailed mannitol production in VAM. These results point to a central role of glucose in modulating host–fungus relations.

We investigated the flood tolerance mechanism of rice coleoptiles by employing $^{13}C_1$-2-acetate tracer with ^{13}C NMR time course analysis [254]. Time-dependent increase in ^{13}C incorporation into different carbons of Glu, Gln, γ-aminobutyrate (GAB), malate, citrate, and glucose was evident in anaerobic rice coleoptiles. The kinetics of ^{13}C-4-Glu and ^{13}C-2-GAB are consistent with GAB production from Glu via Glu decarboxylase activity. The much higher synthesis rate of ^{13}C-3-malate than that of ^{13}C-2-malate points toward an active glyoxylate cycle in the glyoxysome, which produces malate via condensation of acetate with glyoxylate, leading to succinate. This glyoxysome-derived succinate can then be transported to the mitochondria to replenish the Krebs cycle intermediates diverted to GAB synthesis under anaerobiosis. In a separate ^{15}N-nitrate tracer study, we have shown that rice coleoptiles are active in GAB and Ala synthesis as a result of nitrate reduction and assimilation under anaerobiosis, as revealed by 1D 1H and 2D ^{1}H{^{15}N}-HSQC and HSQC–TOCSY analyses [81]. These reactions consume protons and NADH, which are produced in excess via glycolysis under anaerobic conditions. Together these results suggest that rice coleoptiles can better maintain glycolysis and the Krebs cycle for energy production via the pathways of GAB and Ala synthesis and the glyoxylate cycle, in addition to the canonical ethanol fermentation.

Burgess et al. employed different ^{13}C tracers and 1D WET-^{1}H {^{13}C}-HMQC analysis to investigate the substrate-dependence of Krebs cycle kinetics and associated exchange kinetics between Glu and αKG *ex vivo* in perfused mouse heart [255]. They found that the indirect method afforded 6- to 10-fold time savings over direct ^{13}C NMR analysis, enabling time course kinetics to be acquired at 20 s intervals. By fitting the NMR kinetic data to a tca-FLUX model, V_{tca} and V_x (flux through the Krebs cycle and exchange reactions, respectively) were obtained as a function of the ^{13}C tracers used ($^{13}C_1$-2-acetate, $^{13}C_1$-3-lactate, and $^{13}C_4$-2,4,6,8-octanoate). The order of V_{tca} was related to the capacity of the tracers for NADH production external to the Krebs cycle. In addition, the lack of substrate dependence of V_x suggests that malate-Asp shuttle does not significantly contribute to V_x

via Asp aminotransferase, otherwise $^{13}C_1$-3-lactate administration would be expected to post the highest V_x.

Two *ex vivo* tissue studies utilized ^{13}C-glucose and 1D ^{13}C NMR analysis of ^{13}C isotopomers of metabolites to demonstrate functional compartmentation of glycolysis and glycogenolysis in the cytoplasm [256,257]. One study on perfused hog carotid arteries employed sequential administration of $^{13}C_1$-1-glucose to prelabel tissue glycogen, followed by $^{13}C_1$-2-glucose to distinguish glycogenolysis from glycolysis based on the time course of the buildup of $^{13}C_1$-3-lactate (glycogenolysis) and of $^{13}C_1$-2-lactate (glycolysis) [256]. They also found that glycogen did not contribute appreciably to lactate production when mitochondrial activity was intact, but its contribution to lactate synthesis was greatly enhanced by KCN, which inhibited mitochondrial oxidative metabolism. These data are consistent with two separate pools of cytoplasmic glucose with different fates, one pool being derived from external glucose supply to serve primarily as the substrate for glycolysis, and the other pool from glycogen degradation to fuel mitochondrial oxidation. The other study on perfused rat heart substantiated these earlier findings by sequential administration of U-$^{13}C_6$-glucose to prelabel tissue glycogen, followed by $^{13}C_1$-1-glucose to observe both glycogen and glucose metabolism [257]. This labeling scheme enabled discrimination between the pyruvate pools derived from glucose and glycogen by ^{13}C isotopomer analysis of lactate, as well as between the glycolytic and glycogenolytic pyruvate pools that fuel acetyl CoA synthesis based on ^{13}C isotopomer analysis of Glu. The authors concluded that (1) cytoplasmic glycolysis and glycogenolysis are compartmentalized; (2) tissue glycogen carbons are preferentially oxidized via the Krebs cycle while exogenous glucose carbons are the primary source of glycolytic lactate release into the medium; and (3) insulin further polarizes the preference for glycogen as substrate for mitochondrial oxidation.

5.2.2.1.3. Animal studies: Using $^{13}C_1$-3-Ala as tracer coupled with 1D ^{13}C and ^{31}P NMR analyses, energy status in relation to gluconeogenesis was investigated by Morikawa et al. *in vivo* in rat liver [258] They found ^{13}C incorporation into ^{13}C-2 and ^{13}C-3 (but not ^{13}C-4) of Glu/Gln under prolonged fasting, which indicates that entry of Ala-derived pyruvate into the Krebs cycle, is exclusively mediated by pyruvate carboxylase. They also showed ^{13}C incorporation into ^{13}C-1 to 6-glucose and ^{13}C-1-glycogen, which points to active gluconeogenesis from Ala in the rat liver. Both gluconeogenesis and glycogenesis were inhibited under ischemia when liver ATP level was depleted. During recovery from ischemia, ATP level correlated positively with labeled glucose and glycogen signals and negatively with labeled Ala signals. These data provided *in vivo* evidence for the importance of energetics in modulating Ala-mediated gluconeogenesis and glycogenesis in rat liver.

In an *in vivo* study of human brain tumor glioblastoma cell xenografts in an orthotopic mouse model, Marin-Valencia et al. employed continuous infusion of different ^{13}C tracers coupled with 1D ^{13}C NMR analysis to track glucose and Gln utilization [259]. They found that U-$^{13}C_6$-glucose was metabolized into $^{13}C_2$-2,3-Glu and that $^{13}C_2$-3,4-glucose tracer led to a higher production of $^{13}C_1$-1-Glu/Gln than of $^{13}C_1$-5-Glu/Gln; both are consistent with active PC-mediated anaplerosis *in vivo* in GBM tumor. This is in contrast to the GBM cell findings, where PC activity was found to be suppressed [129]. In addition, U-$^{13}C_5$-Gln was not metabolized in the Krebs cycle *in vivo* in GBM tumors [259], but was found to be the

main anaplerotic substrate for the Krebs cycle *in vitro* in GBM cells [129]. Such sharp contrasts between *in vivo* and *in vitro* tumor cell metabolism strongly argue for the need for *in vivo* tracer-based NMR studies.

To gain better spectral resolution and more rigorous metabolite assignment, various 2D NMR techniques have been applied to metabolite analysis *in vivo* in live animals [260]. In particular, 2D $^{1}H\{^{13}C\}$-ge-HMQC was employed to investigate $^{13}C_1$-1-glucose metabolism in cat brain *in vivo* [261]. Signals from ^{13}C-4-Glu and ^{13}C-4-Gln, along with ^{13}C-3-Glu/Gln and ^{13}C-2-Glu/Gln (detected due to better water suppression), were resolved in the 2D spectrum (cf. Fig. 20). These ^{13}C metabolite isotopomers are important in delineating the pathways involved in Glu/Gln cycling, as described above.

5.2.2.1.4. Human studies: Perhaps one of the most powerful applications of NMR in biomedicine lies in *in vivo* human studies, which can provide invaluable novel metabolic insights that cannot be acquired by any other means. *In vivo* NMR studies of human subjects have been mainly focused on the brain [125,262], since human brain tissues are excellently suited for MRI and localized NMR spectroscopy. Presumably the difficulty of brain tissue procurement and the rapid distortion of its metabolism upon resection also add to this focus.

The first ^{13}C NMR spectra of human brain were acquired by Beckmann et al. [263] using surface coils on volunteers infused with $^{13}C_1$-1-glucose. The ^{13}C incorporation into Glu and Gln at C2, C3, and C4 positions as well as into lactate was observed in real time. Subsequent studies utilizing different ^{13}C tracers including $^{13}C_1$-1 or 2-glucose, $^{13}C_1$-3-lactate, or $^{13}C_1$-2-acetate enabled fluxes through the neuronal Krebs cycle (V_{TCAn}) and the Glu/Gln cycle (V_{cyc}) between neurons and astrocytes to be assessed *in vivo* in human brain (Fig. 21). An approximately 1:1 ratio of V_{TCAn} versus V_{cyc} was evident by compiling data from 11 studies, where these two parameters were deduced under varying brain electrical activity [262]. These results suggest a close link between brain energy metabolism via the Krebs cycle and neurotransmitter production and signaling.

Extensive clinical studies have been performed using ^{13}C enriched substrates including ^{13}C-glucose and acetate to study brain disorders (e.g. Alzheimer's, Canavan's encephalopathy, and epilepsy) as well as normal brain development in human subjects [264]. The slow rate of N-acetylaspartate synthesis from $^{13}C_1$-1-glucose was directly observed for the first time in human brain, and it fell further in patients with Canavan's disease. The same tracer was administered to Alzheimer's patients to uncover failure in Gln–Glu cycling and Glu neurotransmission. The beneficial effect of a ketogenic diet on reducing seizures in epileptic children was found to be related to improved Glu-Gln cycling based on enhanced $^{13}C_1$-1-acetate metabolism into Glu and Gln. The infusion of $^{13}C_1$-2-glucose tracer into healthy subjects enabled measurement of pyruvate carboxylase activity via ^{13}C incorporation into C2 and C3 of glutamine and glutamate [265]. Metabolic modeling of the labeling data indicated that pyruvate carboxylase accounted for 6 ± 4% of the rate of glutamine synthesis. Most of the pyruvate carboxylase flux appears to replace glutamate lost due to glial oxidation, and therefore can be considered to support neurotransmitter trafficking.

Continuous infusion of tracer into human subjects [266,267,264] has been commonly employed in *in vivo* human studies, and requires a more elaborate protocol. An alternative is to administer the tracer orally, which at least in brain studies yields similar results to intravenous administration, but with lower precision [267].

5.2.2.2. Hyperpolarized (HP) applications

5.2.2.2.1. Principles of Dynamic Nuclear Hyperpolarization (DNP): Hyperpolarization-based NMR analysis offers very high sensitivity enhancement that has been demonstrated in recent years for imaging *in vivo* dynamics of metabolic reactions in specific regions of tissues [268–290]. The fundamental principle of hyperpolarization is to transfer magnetization from a very highly polarized reservoir to the observed nucleus. One method, called dynamic nuclear polarization (DNP), uses the very high polarization achievable by unpaired electrons in a magnetic field, which is then pumped using a microwave field to the metabolites bearing one or more ^{13}C or ^{15}N atoms [291]. Under this mechanism, the maximal polarization enhancement is given by (γ_e/γ_N), which is about 660 for protons, 2640 for ^{13}C and 6600 for ^{15}N.

The cross-relaxation process for DNP is usually carried out near 1 K, which also provides a large enhancement of polarization via the Boltzmann distribution, i.e. about 300 fold for 1 K versus 300 K. For biological studies, the frozen polarized sample must be warmed rapidly (e.g. to 300 K) for measurements. Since the fractional polarization for ^{13}C at 300 K at 14.1 T is ca. 1.2E–5, and 0.00359 at 1 K, considerable polarization enhancements (>10,000) can only be achieved immediately after thawing [292], in order to benefit from the contribution of electron-mediated cross polarization and the enhanced polarization due to the Boltzmann distribution. Once at higher temperature, with magnetization no longer being pumped, the system will relax toward its equilibrium polarization; the rate at which this process occurs is determined by the T_1 value. Nuclei with long T_1 values are therefore desirable for prolonging the hyperpolarized state. For example, if the warming and thawing process takes 10 s, then about 30% of the initial polarization will be lost for ^{13}C with a T_1 value of 30 s. Thus, the time period for NMR observations is typically limited to ca. $4T_1$. In addition, as this procedure creates an unstable non-equilibriumstate, once the spin has been excited, the polarization is lost, again limiting the number of NMR transients that can be acquired from the same sample while calling for a small flip angle for the excitation pulse. The magnetization available for each pulse with a flip angle of theta is approximately:

$$M^0\exp(-t/T_1)\sin(\theta) \quad (1)$$

where M^0 is the magnetization just before the first excitation pulse, and θ is the flip angle.

The lifetime of the enhanced polarization must be comparable to the half-life of the reaction that is being measured. For the simple reaction A $\Leftrightarrow$ B, the time-dependence of the production of B is

$$b(t)=a(0)[1-\exp-(k_1+k_{-1})t] \quad (2)$$

where k_1 and k_{-1} are the rate constants of the forward and reverse reaction, respectively. As the magnetization of the source is decaying exponentially, the observed magnetization on B following a bolus input of hyperpolarized A is described by the difference between two exponentials, which goes through a maximum, according to the Bloch–McConnell equations below [92].

$$dM_{\mathrm{B}}/dt=\rho_{\mathrm{B}}(M_{\mathrm{B}}-\langle M_{\mathrm{B}}\rangle)-k_{-1}M_{\mathrm{B}}+k_1M_{\mathrm{A}} \quad (3A)$$

$$dM_{\mathrm{A}}/dt=\rho_{\mathrm{A}}(M_{\mathrm{A}}-\langle M_{\mathrm{A}}\rangle)+k_{-1}M_{\mathrm{B}}-k_1M_{\mathrm{A}} \quad (3B)$$

where ρ_{A}, ρ_{B} are the spin lattice relaxation rate constants and $\langle M_{\mathrm{A}}\rangle$, $\langle M_{\mathrm{B}}\rangle$ are the equilibrium magnetizations of A and B. Fig. 22 shows the magnetization time course calculated for such a two-site exchange reaction with an initial relative polarization of A of 10,000 and an equilibrium constant of unity. The magnetization of A decays biexponentially due to the spin-lattice relaxation and the chemical exchange of A with unpolarized B, whereas that of B initially increases from its (low) equilibrium magnetization as the highly polarized A exchanges with B, followed by a decay as the polarization dissipates via longitudinal relaxation. The T_1 value thus sets the timescale of the observation; reactions that do not occur on this timescale are not observed.

The requirement for a long T_1 value limits the nature of the atoms that can be usefully probed. Generally, carbons such as carbonyl and quaternary carbons, that do not have an attached proton, have sufficiently long T_1 values (20–40 s). It is also possible to use perdeuterated compounds such as perdeuterated glucose (cf. Fig. 23) to slow down the longitudinal relaxation process [287].

As the measurement time window is short, the polarized precursor must be quickly introduced to the sample, for example by direct intravenous injection into an animal or human, or by direct addition to a cell growth medium. The kinetics of the metabolic process being observed then encompass the uptake (transport) rate of the substrate and the rate of its subsequent transformations via enzyme-catalyzed reactions. As the T_1 value is typically in the order 20–30 s [92], the time scale of the reactions that can be monitored is in the order of 2 min. This is comparatively long compared with the reciprocal turnover numbers of enzymes involved in central catabolism (in the range 10–1000 s^{-1}). However, one also has to consider the sequential nature of many metabolic reactions, the concentrations of the enzymes, their fractional saturation, and the sizes of the metabolite pools that are being observed. For example, glycolytic enzymes are usually very abundant, with typical concentrations of 1–10 μM [293], and can approach 100 μM in skeletal muscle [294,295]. These concentrations are often comparable to substrate concentrations and K_m values [296]. In fact, for central metabolism, substrate concentrations are typically substantially lower than their K_m values [296].

Thus for a single human cell with cytoplasmic volume of 1 pL and enzyme concentrations of 1 μM, there is about 1 attomole of enzyme molecules per cell. An enzyme with a turnover number (k_{cat}) of 100 s^{-1}, at 10% occupancy, would produce 10 attomoles of product s^{-1} per

cell. On a high field NMR spectrometer with a probe optimized for ^{13}C detection, a SNR of 100:1 may be achieved in a single acquisition on ca. 1 μmol ^{13}C by conventional analysis, or ca. 100 pmol by DNP with an enhancement of 10,000. To produce 25 pmol in 60 s for hyperpolarized NMR detection would then need a minimum of 4×10^4 cells in the sensing region. In practice, many of the reactions under consideration are sequential, so that the intermediates build up to a much lower extent. Furthermore, a small flip angle must be used for kinetic experiments such that ca. 10% or less of the sample magnetization is sampled with each pulse, while the signal is decaying exponentially. By 1 min, only 13% of the initial signal is left and after 2 min, <2% is left, for T_1 = 30 s. These considerations, along with the limited availability of suitable hyperpolarizable substrates (see below), limit the depth of coverage for metabolic pathways in DNP-based experiments.

5.2.2.2.2. Principle of Para-Hydrogen-Induced Hyperpolarization (PHIP): An alternative to the DNP approach is to use para-hydrogen (the singlet state of H_2 which is present at 25% at thermal equilibrium) to induce hyperpolarization (PHIP). Here polarized para-hydrogen (enriched above its equilibrium value) is rapidly added across a double bond of a substrate (which may be deuterated to reduce T_1 relaxation) next to a ^{13}C carbonyl. This process usually requires a catalyst and the polarization is transferred to the target nucleus via scalar interactions [297–302]. Although the variety of substrates that can be polarized using PHIP is limited, the process is much faster than solid state DNP [303]. Polarization enhancements of >3000 have been achieved in a limited number of metabolic substrates [303–306]. The hyperpolarized substrate is then injected into the recipient organism or cell culture. An example of this is the reduction of ^{13}C-1-diethylfumarate to ^{13}C-1-diethylsuccinate with para-hydrogen, which is rapidly taken up by cells, and converted to ^{13}C-1-succinate by internal esterases [303]. The kinetics of the formation of downstream Krebs cycle metabolites ^{13}C-1-fumarate, -malate, and -OAA (via the surrogate aspartate) can be followed *in vivo*.

When coupled with magnetic resonance imaging, hyperpolarization techniques open an avenue for probing metabolic reactions dynamics *in vivo* in specific regions of tissues that is unparalleled by other techniques. This capability is uniquely suited to whole animal and human metabolic studies.

5.2.2.2.3. Applications. Redox ratio determination: Many of the early studies used ^{13}C-1 or ^{13}C-2 pyruvate as substrate, which have relatively long T_1 values and produce significant polarization enhancement via DNP [276,278,306,307]. The enhanced conversion of pyruvate to lactate is generally considered to be important for tumor development [308–311]. This reaction is catalyzed by one of the lactate dehydrogenase (LDH) isoenzymes and can be analyzed according to the simple two-site exchange model (cf Eq. (3)), where the pseudo first order rate constants are related to the enzyme concentration, the enzyme kinetic parameters, and the overall reaction equilibrium constant (K) as described by:

$$\mathrm{Pyruvate}^- + \mathrm{NADH} + \mathrm{H}^+ \iff \mathrm{lactate}^- + \mathrm{NAD}^+ \quad (4A)$$

$$K=[\text{lactate}-][\text{NAD}^+]/[\text{pyruvate}-][\text{NADH}][\text{H}^+] \quad (4B)$$

The intracellular free NAD^+/NADH ratio has been estimated using hyperpolarized [$^{13}C_6$,$^2H_{12}$]-glucose in two cancer cell lines. This was achieved by measuring the free concentrations of pyruvate and lactate by DNP-^{13}C NMR so that the NAD^+/NADH ratio can be calculated from the independently measured intracellular pH and the assumed equilibrium constant. Christensen et al. reported ratios of 2550 ± 350 in prostate cancer PC3 cells and 738 ± 92 inMCF-7 breast cancer cells grown under normoxic condition, and the intracellular pH was estimated to be 7 to 7.1 from the bicarbonate/CO_2(aqueous) ratio by NMR [287], although this value is typically higher than 7.2 in cancer cells [312,313]. The equilibrium constant was assumed to be 1.11×10^{-11} M, though other estimates deviate from this value [314]. Nonetheless, this ratio is in line with other estimates of the order 1000:1 and is far higher than the ratio of total NAD^+ to NADH (i.e. bound + free species), which is typically <10:1 in mammalian cells [315]. Since the total concentration of dehydrogenases in cells is comparable to the total NAD^+ + NADH content, NAD^+ and NADH are largely in the bound state, and have differential affinity for different dehydrogenases. Thus, changes in the free NAD^+/NADH ratio can have important influence on redox-sensitive metabolic reactions, including such central pathways as glycolysis and the Krebs cycle. Similar remarks apply to the less abundant $NADP^+$ and NADPH redox pair, where NADPH is generally thought to be much higher than $NADP^+$, reflecting their functions in supporting anabolic reactions [316]. However, recent *in vitro* studies have reported ratios closer to unity or lower [317,318]. As NADPH is unstable and highly sensitive to extraction artifacts, the *in vivo* hyperpolarization NMR approach would be valuable in resolving this discrepancy. Again, accurate knowledge of the free to bound ratio of $NADP^+$/NADPH, as well as their absolute concentrations, is crucially important in understanding the regulation of anabolic biochemical networks and oxidative stress.

Kinetic isotope effects: Using perdeuterated substrates such as [U-$^{13}C_6$,$^2H_{12}$]-glucose for probing glycolytic dynamics, there is potentially a primary kinetic isotope effect (KIE) on individual reactions if they involve a C-H bond cleavage which contributes to the overall reaction rate. The primary KIE for C-H versus C-D bond breaking step may be of the order 7 or higher if tunneling is active [319,320]. However, the KIE on net pathway flux may be small as the net flux from glucose to end products such as pyruvate and lactate in glycolysis depends on the kinetic properties of all of the enzymes in the pathway, so that the control coefficient for any given reaction is small [321– 323]. Nevertheless, significant KIEs on parts of metabolic pathways such as the oxidative branch of the pentose phosphate pathway have been observed under steady state conditions [322], which implies that under transient conditions (as with bolus hyperpolarization), such effects may become significant.

Pathway flux analysis: The dynamics of metabolic reactions measured by *in vivo* NMR are influenced by the rates of a number of processes. For example, the conversion of pyruvate to lactate observed by DNP-NMR is governed by the rate of pyruvate uptake via the monocarboxylate transporter, the exchange reaction between pyruvate and lactate, and as many other reactions that utilized pyruvate. A number of recent studies on cells and tissues

of models animal and human subjects indicate that the observed time course conversion of ^{13}C-1-pyruvate or ^{13}C-2-pyruvate to ^{13}C-lactate largely reflects an exchange flux, which at the time immediately after the bolus injection is dominated by the reductive rate (i.e. lactate formation) [92,278,271,304,324–328].

The kinetics of other routes of pyruvate utilization have also been measured, including rapid transamination to alanine catalyzed by the alanine-α-ketoglutarate transaminases (ALT) [162,329], transport into the mitochondria and oxidative decarboxylation to acetyl CoA and CO_2 via pyruvate dehydrogenase, followed by downstream Krebs cycle reactions [160,161,270,330,331], ATP-dependent pyruvate carboxylation to OAA and its subsequent reactions in the Krebs cycle, nucleotide biosynthesis, the aspartate/malate shuttle, and as the entry point to gluconeogenesis in some tissues [68,332].

In recent years a wider variety of hyperpolarized substrates have become available, that can probe different parts of central metabolism [92,272,283,333,281,334], as summarized in Fig. 23. The kinetics of conversion of deuterated ^{13}C glucose by glycolysis into pyruvate and then to lactate or into PPP intermediates, were obtained *in situ* in cancer cells and tumor tissues [277,287]. Meier et al. [335] observed real-time metabolic transformation of hyperpolarized glucose in *E. coli* into DHAP, 3-3PGA, pyruvate, lactate, ethanol, alanine, acetate and acetyl CoA, as well as the decarboxylation products CO_2(aqueous) and HCO_3^-, over a time period of 75 s. Indeed most of the metabolic reactions occurred very rapidly in this system (half life of formation of 10 s or less). Similarly, glucose metabolism was followed in cultured breast cancer cells, in which DHAP, 3PGA and lactate were directly observed, and by saturation transfer other glycolytic intermediates including G6P, F6P, phosphoenolpyruvate (PEP), and pyruvate could be detected [336]. To probe glycolysis and gluconeogenesis in mouse liver, Moreno et al. [337] introduced hyperpolarized ^{13}C-2-DHAP, which was rapidly metabolized to $^{13}C_2$-2,5-glucose, ^{13}C-2-glycerol-3-phosphate (G3P), ^{13}C-2-PEP, ^{13}C-2-pyruvate, ^{13}C-2-Ala, and ^{13}C-2-lactate, showing the central role of DHAP in both glycolysis and gluconeogenesis, as well as the gateway to phospholipid synthesis via the precursor G3P (cf. Fig. 23). However, ^{13}C carbonyl resonance assignments of metabolites based only on chemical shift and biochemical intuition could be problematic. Recently it was shown that a particular signal was assigned to 6-phosphogluconate (6PG) in tumors, but 3PGA in yeast and potentially in other systems [338]. The biochemical interpretation of these assignments is distinct, as 3PGA relates to glycolytic flux while 6PG reflects flux through the oxidative branch of the pentose phosphate pathway.

Besides glucose-derived pyruvate as a carbon source, the Krebs cycle has multiple other carbon inputs, such as beta-oxidation and anaplerotic glutaminolysis (Fig. 23). Glutaminase activity was measured by the conversion of hyperpolarized $^{13}C_5$-Gln into Glu in HepG2 liver cancer cells [339] and in prostate cancer cell lines [286]. Transformation of hyperpolarized ^{13}C-1-glutamate into α-ketoglutarate was also observed in HepG2 cells via the activity of ALT [279]. This glutaminase pathway is thought to be a major contributor to survival and proliferation in reprogrammed tumor metabolism [340,341]. Further reactions down the Krebs cycle have been probed using the hyperpolarized diethyl ester of ^{13}C-1-deuterosuccinate (readily taken up by cells), which was then converted into succinate, malate, fumarate, and aspartate (cf. Fig. 23).

Using hyperpolarized $^{13}C_1$-α-ketoisocaproate as a tracer substrate, the branched chain amino acid Leu metabolism via branched chain amino acid transferase (BCAT) was probed in murine lymphoma (EL4) versus rat mammary adenocarcinoma (R3230AC) tumors. BCAT is a putative marker of metastasis and a target of the proto-oncogene c-*MYC*. Its activity was monitored by the conversion of $^{13}C_1$-α-ketoisocaproate to Leu. EL4 but not R3230A tumors show a more than 7-fold higher hyperpolarized ^{13}C-leucine signal relative to the surrounding healthy tissue. The distinct molecular signatures of branched chain amino acid metabolism in EL4 and R3230AC tumors correlate well with *ex vivo* assays of BCAT activity [342].

It has been proposed that precursors could be multiplexed, such as ^{13}C-1-pyruvate, ^{13}C-sodium bicarbonate, $^{13}C_2$-1,4-fumarate, and ^{13}C-urea to measure multiple enzyme activities *in vivo* [274]. A recent MRI study demonstrates the feasibility of co-hyperpolarizing three ^{13}C labeled agents (^{13}C-urea, ^{13}C-1-hydroxymethylcyclopropane (HMCP), and ^{13}C-2-*t*-butanol) for obtaining rapid dynamic images of their distribution in mouse tissues using multiband frequency encoding coupled with the steadystate free precession (SSFP) method [343]. The dynamic *in vivo* ^{13}C MRI data enabled tissue perfusion and permeability to be quantified. As shown in Fig. 24, *t*-butanol crossed the blood-brain barrier at a remarkable speed, unlike urea and HMCP. Prostate tumor tissues exhibited a higher permeability for urea and HMCP than normal brain and liver tissues. This capability of HP MRI opens up the possibility of *in vivo* measurement of drug delivery efficiency to target tissues.

Cardiac metabolism using hyperpolarized substrates has also been an active area of study, including the use of hyperpolarized $^{13}C_1$-2-pyruvate to interrogate the role of acetyl carnitine as a buffer for acetyl CoA supply in ex vivo rat heart [344]. $^{13}C_1$-2- and/or $^{13}C_1$-1-pyruvate were employed to uncover a switch from predominant fatty acid oxidation to reliance on glucose oxidation in spontaneously hypertensive rat heart, while hyperthyroidism-induced hypertrophic rat heart had reduced glucose oxidation, which was mediated by pyruvate dehydrogenase kinase activity. This capability of $^{13}C_1$-1-pyruvate to discriminate modes of cardiac dysregulations in different causes of cardiac hypertrophy is unparalleled [345].

6. Integration of metabolic network information with knowledge gained from other ‘omics technologies

It is clear that the variety of NMR techniques coupled with the stable isotope tracer approach described above affords powerful means for exploring metabolic network dynamics in organisms and their perturbations in response to stressors. In particular, the ability of NMR to track metabolic changes noninvasively or *in situ* provides unmatched means for determining the dynamics and compartmentation of metabolic pathways directly in living organisms, including human subjects. Such knowledge has been sparse, but is required for our understanding of metabolism at the systems level. It is also important to realize that NMR alone cannot resolve the vastly complex and intersecting relationships of metabolic networks, and that mass spectrometry represents another powerful molecular structure-based platform that can both complement and confirm NMR approaches in deciphering metabolic

network puzzles. This aspect has been discussed elsewhere and will not be elaborated here [11,88,346].

It should be further emphasized that the combination of stable isotope tracers with NMR and MS analytical power is capable of resolving metabolic reprogramming at specific enzyme steps such as the pyruvate carboxylase reaction, even directly in human subjects (cf. Fig. 18) [97,107]. The NMR- and MS-acquired stable isotope labeling patterns (positional isotopomers and mass isotopologues) of metabolites are also excellent constraint parameters formetabolic networkmodeling to globally deconvolute individual enzyme kinetics [180,347–358]. As illustrated in Fig. 17A, such information on perturbations of metabolic network dynamics is invaluable for directing functional analysis of other ‘omics data, including genomics, epigenomics, transcriptomics, and proteomics. For example, we learned from a SIRM study that selenite blocks glycolysis and the Krebs cycle in lung cancer A549 cells. Inquiring into the transcriptomic data acquired in parallel, we discovered that these perturbations could result from downregulation of multiple enzyme genes in glycolysis and the Krebs cycle (Fig. 17) [108]. Likewise, the buildup of lipid catabolites (phosphorylcholine, glycerolphosphorylcholine, and inositols) points to enhanced lipid degradation (Fig. 17B). Again, transcriptomic data on phospholipases and lyosphospholipases substantiate the SIRM observation that lipid catabolism is enhanced via upregulation of lipases.

We also discovered from the transcriptomic data down regulation of the key enzyme, acetyl CoA carboxylase (ACC), in the fatty acid biosynthesis, and up regulation of its negative regulator AMPK (AMP-dependent kinase). These gene expression changes, together with heightened AMP/ATP ratio (known to activate AMPK), suggest reduced fatty acid biosynthesis in selenite-treated A549 cells. Subsequent 2D $^{1}H\{^{13}C\}$-HSQC analysis of ^{13}C labeling patterns of A549 lipids showed reduced synthesis of fatty acyl chains, but not glycerol backbone synthesis in response to selenite treatment (Fig. 17B). These results in combination with the transcriptomic evidence show that the selenite attenuation of lipid biosynthesis is mediated via the AMPK-ACC axis, but not via glycerol-3-phosphate synthesis or incorporation into lipids. Protein expression analysis using Western blot confirmed inhibition of ACC activity via ACC phosphorylation by AMPK (Fig. 17C). However, the activation of AMPK appeared to be more complex than enhanced gene expression of AMPK. We found that AMPK phosphorylation was attenuated by selenite, which points towards AMPK activation via suppressing its inhibitor kinase LKB1 activity [359]. Thus, metabolomics-edited transcriptomic analysis (META) not only generates testable hypotheses on metabolic dysregulations at the transcript level, but together with targeted protein analysis also uncovers signaling cascade(s) that modulate the observed metabolic reprogramming.

Although performed manually, the above case study exemplifies the synergistic value of integrating SIRM with other ‘omics approaches in achieving systems biochemical understanding of biological perturbations. The study also illustrates that optimal gain is attained by bidirectional and cross-correlational integration of ‘omics data. Future bioinformatics development on such integration will present an unprecedented opportunity

for advancing systems biochemistry in organisms of interest, whether related to pathogenesis, environmental stresses or organismal interactions.

7. Conclusions and future directions

NMR has a number of unparalleled advantages for metabolic studies, most notably the rigor and versatility in structure elucidation, and in analysis of positional isotopomer distribution, afforded by multinuclear and multidimensional experiments, as well as the capacity for *in vivo* spatially selective analysis of tissues in living organisms. There are also limitations on NMR in metabolic studies, including (1) its relatively low sensitivity [360] (ca. 1 nmol without hyperpolarization or in the 10 pmol range with hyperpolarization for kinetic studies), compared with LC-MS, where femtomole detection is now routine; and (2) limited resolution in terms of the number of metabolites relative to high-resolution MS. Although fmol detection is routine in LC-MS, the amount of material needed to achieve this detection limit is much larger, as only a small fraction of the LC eluate can be introduced into the mass spectrometer. Although MS-based profiling is now more popular in metabolomic studies, NMR has been and will continue to be a key player in stable isotope-resolved metabolomic studies. It synergizes with MS in such applications by providing complementary and indispensible isotopomer distribution information, as illustrated in this review. With resurgent interest in probing metabolism *in vivo*, particularly in human subjects, NMR's ability to track metabolic dynamics *in situ* in living cells and tissues is unmatched by any other technique. For these reasons, we expect to see future expansion of NMR applications in metabolic research. Further development in NMR techniques to improve detection limits and resolution is therefore highly desirable to facilitate this expansion. Below, we list a few areas of development that are under way.

There are several approaches to improving sensitivity. The most expensive option is to develop ultrahigh magnetic field strength, of the order 23–28 T [361,362], which may benefit metabolic NMR more than macromolecular NMR. However the performance of cryogenic probes and field stability at such high magnetic field strength is presently problematic, and the sensitivity enhancement may not approach the expected theoretical field dependence (see above). Cryogenic probes can provide a substantial sensitivity boost, typically 4-fold over a comparable RT probe for non-lossy samples. This is significantly compromised in lossy (ionic) samples, a problem which is exacerbated at higher magnetic field strength. Using smaller diameter (e.g. 1–1.7 mm) probes will reduce such losses, while improving intrinsic performance, particularly for mass-limited samples [76,363]. Shaped tubes have also been developed to reduce the influence of the E-field in salty samples [364].

To greatly expand 1D NMR resolution, and to gain much more structural insights, further development in multidimensional NMR is indispensible, particularly in terms of the speed of data acquisition. There have been multiple developments that improve this aspect, including non-uniform sampling [154,365] and projection–reconstruction [366,367]. There are also hardware approaches, including multiple receivers enabling 2 or more 2D experiments to be acquired simultaneously [368,369], as well as one-shot 2/3D methods which acquire different "increments" at different slices of the sample [370–376]. However, the latter put greater demands on sensitivity [377].

The number of increments needed for nD NMR can also be reduced using selective excitation methods, or pre-choosing which metabolites present in a mixture are to be sampled, using the Hadamard approach [366] for targeted analyses. The latter approach will be limited for metabolic profiling and/or SIRM studies, where the goal is to obtain as much coverage as possible, including isotopomer distributions.

Slow relaxation or long T_1 is a significant limitation on the speed of NMR acquisition. Very fast pulsing results in compromised sensitivity and highly distorted intensities, requiring large corrections for quantitative analysis. The SOFAST HMQC experiment that works well for ^{15}N-enriched proteins [378] is inappropriate for metabolite analysis, for lack of fast relaxing proton reservoirs and due to the need for sampling the entire spectral region. Fast HMQC using Hartmann-Hahn polarization sharing [379] has been described, but may be of less value for ^{13}C isotopomer analysis. A third alternative is to reduce the T_1 of protons by paramagnetic relaxation enhancement, allowing shorter recycle times [380]. A combination of these solutions is most likely to improve the throughput of 2D NMR methods to make them more attractive for routine NMR analysis, thereby attaining greater reliability for metabolite assignments and isotopomer distribution analysis as well as resolving capacity.

Furthermore, there is a resurging interest in *in vivo* NMR applications, as magnetic resonance imaging (MRI) and image-guided spectroscopy (MRS) have greatly improved in terms of ease of use, sensitivity, and circumvention of motion-mediated artifacts. Together with further developments in hyperpolarization technologies, particularly in terms of the choice of reagents [381] and repetitive polarization, MRS will find many more powerful applications not only in basic and preclinical research but also in the clinical arena [92,298,382,383]. The metabolic insights to be gained from NMR analyses will be a key to our quest for achieving systems biochemical understanding in living organisms.

Acknowledgments

This work was supported in part by NIH grants: 1R01CA118434-01A2, 1U24DK097215-01A1, P01 CA163223-01A1 and NIH 5R01ES022191-04. NIH had no role in the preparation of the article.

We thank Drs. P. Dobrowolski and P. Lin for careful reading of the manuscript.

Glossary of abbreviations

ACC	acetyl CoA carboxylase
AMPK	AMP-dependent kinase
CA	cancer(ous)
CS	chemical selective
DHAP	dihydroxyacetene phosphate
DNP	Dynamic Nuclear Hyperpolarization
DSS	2,2-dimethyl-4-silapentane-4-sulfonic acid
F6P	fructose-6-phosphate

FBP	fructose-1,6-bisphosphate
GAB	γ-aminobutyrate
GAIMS	*G*enetic *A*lgorithm for *I*sotopologues in *M*etabolic *S*ystems
GAP	glyceraldehyde-3-phosphate
GBM	glioblastoma multiforme
G3P	glycerol-3-phosphate
G6P	glucose-6-phosphate
GFT	G-matrix Fourier transform
GSH	reduced glutathione
GSSG	oxidized glutathione
GPC	glycerophosphocholine
HMBC	heteronuclear multiple bond coherence
HRMAS	High Resolution Magic Angle Spinning
HSQC	heteronuclear single quantum coherence
INADEQUATE	Incredible Natural Abundance DoublE QUAntum Transfer Experiment
INEPT	insensitive nuclei enhanced by polarization transfer
IROA	Isotope Ratio Outlier Analysis
KIE	kinetic isotope effect
Lac	lactate
LDHA	lactate dehydrogenase isozyme A
META	Metabolomics-Edited Transcriptomics Analysis
MS	mass spectrometry
MTBE	methyl-tert-butyl ether
NC	non-cancer(ous)
NSCLC	non-small cell lung cancer
PDH	pyruvate dehydrogenase
PEP	phosphoenolpyruvate
3PGA	3-phosphoglycerate
PHIP	Para-hydrogen-Induced Hyperpolarization
PR	projection reconstruction
OAA	oxalacetatic acid
QDA	*Q*uaternary ammonium *D*odecyl dimethyl *A*minooxy

PC	pyruvate carboxylase
PCA	perchloric acid
PEPC	phosphoenolpyruvate carboxylase
SCID	Severe Combined Immunodeficiency
SIRM	stable isotope-resolved metabolomics
SNR	signal-to-noise ratio
TCA	trichloroacetic acid
TME	tumor microenvironment
TSP	3-(trimethylsilyl)propanoic acid
TOCSY	total correlation spectroscopy
UDPG	uridine diphosphate glucose
UDP-GlcNAc	uridine diphosphate N-acetyl glucosamine
UXP	uridine nucleotide (UM, UDP or UTP)
VAM	vesicular-arbuscular mycorrhizal

References

1. Purcell E, Torrey H, Pound R. Resonance absorption by nuclear magnetic moments in a solid. Phys Rev. 1946; 69:37–38.
2. Bloch F. Nuclear induction. Phys Rev. 1946; 70:460–474.
3. Fan TWM, Higashi RM, Lane AN, Jardetzky O. Combined use of proton NMR and gas chromatography–mass spectra for metabolite monitoring and in vivo proton NMR assignments. Biochim Biophys Acta. 1986; 882:154– 167. [PubMed: 3011112]
4. Evanochko WT, Sakai TT, Ng TC, Krishna NR, Kim HD, Zeidler RB, Ghanta VK, Brockman RW, Schiffer LM, et al. NMR study of in-vivo Rif-1 tumors analysis of perchloric-acid extracts and identification of proton phosphorus-31 and carbon-13 resonances. Biochim Biophys Acta. 1984; 805:104–116. [PubMed: 6477969]
5. Bales JR, Higham DP, Howe I, Nicholson JK, Sadler PJ. Use of high-resolution proton nuclear magnetic resonance spectroscopy for rapid multi-component analysis of urine. Clin Chem. 1984; 30:426–432. [PubMed: 6321058]
6. Nicholson JK, Buckingham MJ, Sadler PJ. High-resolution H-1-NMR studies of vertebrate blood and plasma. Biochem J. 1983; 211:605–615. [PubMed: 6411064]
7. Chen C, Gonzalez FJ, Idle JR. LC–MS-based metabolomics in drug metabolism. Drug Metab Rev. 2007; 39:581–597. [PubMed: 17786640]
8. Metz TO, Zhang Q, Page JS, Shen Y, Callister SJ, Jacobs JM, Smith RD. The future of liquid chromatography–mass spectrometry (LC–MS) in metabolic profiling and metabolomic studies for biomarker discovery. Biomark Med. 2007; 1:159–185. [PubMed: 19177179]
9. Theodoridis GA, Gika HG, Want EJ, Wilson ID. Liquid chromatography-mass spectrometry based global metabolite profiling: a review. Anal Chim Acta. 2012; 711:7–16. [PubMed: 22152789]
10. Sumner LW, Bedair M. Current and emerging mass-spectrometry technologies for metabolomics. TRAC – Trends Anal Chem. 2008; 27:238– 250.
11. Fan TW, Lorkiewicz PK, Sellers K, Moseley HN, Higashi RM, Lane AN. Stable isotope-resolved metabolomics and applications for drug development. Pharmacol Ther. 2012; 133:366–391. [PubMed: 22212615]

12. Sanders, JKM.; Hunter, BK. A Guide for Chemists. Oxford University Press; Oxford, UK: 1987. Modern NMR Spectroscopy.
13. Wuthrich, K. NMR of Proteins and Nucleic Acids. Wiley; New York: 1986.
14. Dewar BJ, Keshari K, Jeffries R, Dzeja P, Graves LM, Macdonald JM. Metabolic assessment of a novel chronic myelogenous leukemic cell line and an imatinib resistant subline by H-1 NMR spectroscopy. Metabolomics. 2010; 6:439–450. [PubMed: 20676217]
15. Posma JM, Garcia-Perez I, De Iorio M, Lindon JC, Elliott P, Holmes E, Ebbels TMD, Nicholson JK. Subset optimization by reference matching (STORM): an optimized statistical approach for recovery of metabolic biomarker structural information from H-1 NMR spectra of biofluids. Anal Chem. 2012; 84:10694–10701. [PubMed: 23151027]
16. Der-Torossian H, Asher SA, Winnike JH, Wysong A, Yin XY, Willis MS, O'Connell TM, Couch ME. Cancer cachexia's metabolic signature in a murine model confirms a distinct entity. Metabolomics. 2013; 9:730–739.
17. Robinette SL, Lindon JC, Nicholson JK. Statistical spectroscopic tools for biomarker discovery and systems medicine. Anal Chem. 2013; 85:5297– 5303. [PubMed: 23614579]
18. Chen C, Deng LL, Wei SW, Gowda GAN, Gu HW, Chiorean EG, Abu Zaid M, Harrison ML, Pekny JF, Loehrer PJ, Zhang DB, Zhang M, Raftery D. Exploring metabolic profile differences between colorectal polyp patients and controls using seemingly unrelated regression. J Proteome Res. 2015; 14:2492–2499. [PubMed: 25919433]
19. Emwas AH, Luchinat C, Turano P, Tenori L, Roy R, Salek RM, Ryan D, Merzaban JS, Kaddurah-Daouk R, Zeri AC, Gowda GAN, Raftery D, Wang YL, Brennan L, Wishart DS. Standardizing the experimental conditions for using urine in NMR-based metabolomic studies with a particular focus on diagnostic studies: a review. Metabolomics. 2015; 11:872–894. [PubMed: 26109927]
20. Kaddurah-Daouk R, Weinshilboum R. Metabolomic signatures for drug response phenotypes: pharmacometabolomics enables precision medicine. Clin Pharmacol Ther. 2015; 98:71–75. N. Pharmacometabolomics Res. [PubMed: 25871646]
21. Fan TW-M, Lorkiewicz P, Sellers K, Moseley HNB, Higashi RM, Lane AN. Stable isotope-resolved metabolomics and applications to drug development. Pharmacol Ther. 2012; 133:366–391. [PubMed: 22212615]
22. Fan TW-M, Lane AN. Structure-based profiling of metabolites and isotopomers by NMR. Progr NMR Spectrosc. 2008; 52:69–117.
23. Fan TW-M. Metabolite profiling by one- and two-dimensional NMR analysis of complex mixtures. Prog Nucl Magn Reson Spectrosc. 1996; 28:161–219.
24. Bingol K, Li D-W, Bruschweiler-Li L, Cabrera OA, Megraw T, Zhang F, Brueschweiler R. Unified and isomer-specific NMR metabolomics database for the accurate analysis of C-13–H-1 HSQC spectra. ACS Chem Biol. 2015; 10:452–459. [PubMed: 25333826]
25. Bingol K, Brueschweiler R. NMR/MS translator for the enhanced simultaneous analysis of metabolomics mixtures by NMR spectroscopy and mass spectrometry: application to human urine. J Proteome Res. 2015; 14:2642–2648. [PubMed: 25881480]
26. Fan, TW-M.; Lane, AN. Assignment strategies for NMR resonances in metabolomics research. In: Lutz, N.; Sweedler, JV.; Weevers, RA., editors. Methodologies for Metabolomics: Experimental Strategies and Techniques. Cambridge University Press; Cambridge: 2013.
27. Weljie AM, Newton J, Mercier P, Carlson E, Slupsky CM. Targeted profiling: quantitative analysis of H-1 NMR metabolomics data. Anal Chem. 2006; 78:4430–4442. [PubMed: 16808451]
28. Lane, AN. NMR applications in metabolomics. In: Fan, TW-M.; Lane, AN.; Higashi, RM., editors. Handbook of Metabolomics. Humana; 2012.
29. Fan, TW-M.; Lane, AN. Assignment strategies for NMR resonances in metabolomics research. In: Lutz, N.; Sweedler, JV.; Weevers, RA., editors. Methodologies for Metabolomics: Experimental Strategies and Techniques. Cambridge University Press; Cambridge: 2012.
30. Horak RM, Steyn PS, Vleggaar R. Carbon–carbon coupling-constants derived from biosynthetic-studies. Magn Reson Chem. 1985; 23:995–1039.
31. Lane AN, Arumugam S, Lorkiewicz PK, Higashi RM, Laulhe S, Nantz MH, Moseley HNB, Fan TWM. Chemoselective detection and discrimination of carbonyl-containing compounds in

metabolite mixtures by H-1-detected N-15 nuclear magnetic resonance. Magn Reson Chem. 2015; 53:337–343. [PubMed: 25616249]

32. Gradwell MJ, Fan TWM, Lane AN. Analysis of phosphorylated metabolites in crayfish extracts by two-dimensional H-1–P-31 NMR heteronuclear total correlation spectroscopy (HeteroTOCSY). Anal Biochem. 1998; 263:139–149. [PubMed: 9799525]
33. Tayyari F, Gowda G, Gu H, Raftery D. ^{15}N-cholamine – a smart isotope tag for combining NMR- and MS-based metabolite profiling. Anal Chem. 2013; 85:8715–8721. [PubMed: 23930664]
34. Ye T, Mo HP, Shanaiah N, Gowda GAN, Zhang SC, Raftery D. Chemoselective ^{15}N tag for sensitive and high-resolution nuclear magnetic resonance profiling of the carboxyl-containing metabolome. Anal Chem. 2009; 81:4882–4888. [PubMed: 19518144]
35. Gori SS, Lorkiewicz PK, Ehringer DS, Belshoff AC, Higashi RM, Fan TW-M, Nantz MH. Profiling thiol metabolites and quantification of cellular glutathione using FT-ICR-MS spectrometry. Anal Bioanal Chem. 2014; 406:4371–4379. [PubMed: 24858467]
36. Bousamra M 2nd, Schumer E, Li M, Knipp R, Nantz MH, van Berkel VFX. Quantitative analysis of exhaled carbonyl compounds distinguishes benign from malignant pulmonary disease. J Thorac Cardiovasc Surg. 2014; 148:1074–1080. [PubMed: 25129599]
37. Mattingly SJ, Xu T, Nantz MH, Higashi RM, Fan TWM. A carbonyl capture approach for profiling oxidized metabolites in cell extracts. Metabolomics. 2012; 8:989–996. [PubMed: 23175637]
38. Shaykhutdinov RA, MacInnis GD, Dowlatabadi R, Weljie AM, Vogel HJ. Quantitative analysis of metabolite concentrations in human urine samples using C-13{H-1} NMR spectroscopy. Metabolomics. 2009; 5:307–317.
39. Clendinen CS, Lee-McMullen B, Williams CM, Stupp GS, Vandenborne K, Hahn DA, Walter GA, Edison AS. C-13 NMR metabolomics: applications at natural abundance. Anal Chem. 2014; 86:9242–9250. [PubMed: 25140385]
40. Bingol K, Brueschweiler R. Multidimensional approaches to NMR-based metabolomics. Anal Chem. 2014; 86:47–57. [PubMed: 24195689]
41. Bingol K, Bruschweiler-Li L, Li D-W, Brueschweiler R. Customized metabolomics database for the analysis of NMR H-1–H-1 TOCSY and C-13– H-1 HSQC–TOCSY spectra of complex mixtures. Anal Chem. 2014; 86:5494– 5501. [PubMed: 24773139]
42. Clendinen CS, Pasquel C, Ajredini R, Edison AS. C-13 NMR metabolomics: INADEQUATE network analysis. Anal Chem. 2015; 87:5698–5706. [PubMed: 25932900]
43. Hegeman AD, Schulte CF, Cui Q, Lewis IA, Huttlin EL, Eghbalnia H, Harms AC, Ulrich EL, Markley JL, Sussman MR. Stable isotope assisted assignment of elemental compositions for metabolomics. Anal Chem. 2007; 79:6912–6921. [PubMed: 17708672]
44. de Jong FA, Beecher C. Addressing the current bottlenecks of metabolomics: isotopic ratio outlier analysis (TM), an isotopic-labeling technique for accurate biochemical profiling. Bioanalysis. 2012; 4:2303–2314. [PubMed: 23046270]
45. Stupp GS, Clendinen CS, Ajredini R, Szewc MA, Garret T, Menger RF, Yost RA, Beecher C, Edison AS. Isotopic ratio outlier analysis global metabolomics of *Caenorhabditis elegans*. Anal Chem. 2013; 85:11858–11865. [PubMed: 24274725]
46. Barfield M. DFT/FPT studies of the structural dependencies of long-range H-1, H-1 coupling over four bonds (4)J(H,H′) in propanic and allylic systems. Magn Reson Chem. 2003; 41:344–358.
47. Barfield M, Dingley AJ, Feigon J, Grzesiek S. A DFT study of the interresidue dependencies of scalar J-coupling and magnetic shielding in the hydrogen-bonding regions of a DNA tripler. J Am Chem Soc. 2001; 123:4014–4022. [PubMed: 11457152]
48. Rusakov YY, Krivdin LB. Four-component relativistic DFT calculations of Se-77 NMR chemical shifts: a gateway to a reliable computational scheme for the medium-sized organoselenium molecules. J Comput Chem. 2015; 36:1756–1762. [PubMed: 26132843]
49. Dona AC, Jimenez B, Schaefer H, Humpfer E, Spraul M, Lewis MR, Pearce JTM, Holmes E, Lindon JC, Nicholson JK. Precision high-throughput proton NMR spectroscopy of human urine, serum, and plasma for large-scale metabolic phenotyping. Anal Chem. 2014; 86:9887–9894. [PubMed: 25180432]

50. Bally T, Rablen PR. Quantum-chemical simulation of H-1 NMR spectra 2. Comparison of DFT-based procedures for computing proton–proton coupling constants in organic molecules. J Org Chem. 2011; 76:4818–4830. [PubMed: 21574622]
51. Choi C, Ganji SK, DeBerardinis RJ, Hatanpaa KJ, Rakheja D, Kovacs Z, Yang XL, Mashimo T, Raisanen JM, Marin-Valencia I, Pascual JM, Madden CJ, Mickey BE, Malloy CR, Bachoo RM, Maher EA. 2-Hydroxyglutarate detection by magnetic resonance spectroscopy in subjects with IDH-mutated gliomas. Nat Med. 2012; 18:624–629. [PubMed: 22281806]
52. Dang L, White DW, Gross S, Bennett BD, Bittinger MA, Driggers EM, Fantin VR, Jang HG, Jin S, Keenan MC, Marks KM, Prins RM, Ward PS, Yen KE, Liau LM, Rabinowitz JD, Cantley LC, Thompson CB, Heiden MGV, Su SM. Cancer-associated IDH1 mutations produce 2-hydroxyglutarate. Nature. 2009; 462:U739–U752.
53. Achouri Y, NoeL G, Vertommen D, Rider MH, Veiga-Da-Cunha M, van Schaftingen E. Identification of a dehydrogenase acting on D-2-hydroxyglutarate. Biochem J. 2004; 381:35–42. [PubMed: 15070399]
54. Kranendijk M, Struys EA, Salomons GS, Van der Knaap MS, Jakobs C. Progress in understanding 2-hydroxyglutaric acidurias. J Inherit Metab Dis. 2012; 35:571–587. [PubMed: 22391998]
55. Rzem R, Vincent MF, Van Schaftingen E, Veiga-da-Cunha M. L-2-Hydroxyglutaric aciduria, a defect of metabolite repair. J Inherit Metab Dis. 2007; 30:681–689. [PubMed: 17603759]
56. Struys EA, Salomons GS, Achouri Y, Van Schaftingen E, Grosso S, Craigen WJ, Verhoeven NM, Jakobs C. Mutations in the D-2-hydroxyglutarate dehydrogenase gene cause D-2-hydroxyglutaric aciduria. Am J Hum Genet. 2005; 76:358–360. [PubMed: 15609246]
57. Lane AN, Fan TW, Higashi RM. Isotopomer-based metabolomic analysis by NMR and mass spectrometry. Biophys Tools Biol. 2008; 84:541–588.
58. Fasano M, Curry S, Terreno E, Galliano M, Fanali G, Narciso P, Notari S, Ascenzi P. The extraordinary ligand binding properties of human serum albumin. IUMBM Life. 2005; 57:787–796. [PubMed: 16393781]
59. Henry, JB.; McPherson, RA.; Pincus, MR. Henry's Clinical Diagnosis and Management by Laboratory Methods. 22. Elsevier/Saunders; Philadelphia: 2011.
60. Jupin M, Michiels PJ, Girard FC, Spraul M, Wijmenga SS. NMR identification of endogenous metabolites interacting with fatted and non-fatted human serum albumin in blood plasma: fatty acids influence the HSA-metabolite interaction. J Magn Reson. 2013; 228:81–94. [PubMed: 23357430]
61. Jupin M, Michiels PJ, Girard FC, Spraul M, Wijmenga SS. NMR metabolomics profiling of blood plasma mimics shows that medium- and long-chain fatty acids differently release metabolites from human serum albumin. J Magn Reson. 2014; 239:34–43. [PubMed: 24374750]
62. Akoka S, Barantin L, Trierweiler M. Concentration measurement by proton NMR using the ERETIC method. Anal Chem. 1999; 71:2554–2557. [PubMed: 21662801]
63. Gowda GAN, Raftery D. Quantitating metabolites in protein precipitated serum using NMR spectroscopy. Anal Chem. 2014; 86:5433–5440. [PubMed: 24796490]
64. Gowda GAN, Gowda YN, Raftery D. Expanding the limits of human blood metabolite quantitation using NMR spectroscopy. Anal Chem. 2015; 87:706–715. [PubMed: 25485990]
65. Fan, TW-M. Sample preparation for metabolomics investigation. In: Fan, TW-M.; Lane, AN.; Higashi, RM., editors. The Handbook of Metabolomics: Pathway and Flux Analysis, Methods in Pharmacology and Toxicology. Springer Science; New York: 2012. p. 7-27.http://dx.doi.org/10.1007/978-1-61779-618-0_11
66. Lindon, JC.; Nicholson, JK.; Everett, JR. Annual Reports on NMR Spectroscopy. Vol. 38. Academic Press Inc; San Diego: 1999. NMR spectroscopy of biofluids; p. 1-88.
67. Nicholson JK, Foxall PJD, Spraul M, Farrant RD, Lindon JC. 750-MHz H-1 and H-1–C-13 NMR-spectroscopy of human blood-plasma. Anal Chem. 1995; 67:793–811. [PubMed: 7762816]
68. Sellers K, Fox MP, Bousamra M, Slone S, Higashi RM, Miller DM, Wang Y, Yan J, Yuneva MO, Deshpande R, Lane AN, Fan TW-M. Pyruvate carboxylase is critical for non-small-cell lung cancer proliferation. J Clin Invest. 2015; 125:687–698. [PubMed: 25607840]

69. Lewis IA, Schommer SC, Hodis B, Robb KA, Tonelli M, Westler WM, Suissman MR, Markley JL. Method for determining molar concentrations of metabolites in complex solutions from two-dimensional H-1–C-13 NMR spectra. Anal Chem. 2007; 79:9385–9390. [PubMed: 17985927]
70. Lewis, IA.; Shortreed, MR.; Hegeman, AD.; Markley, JL. Novel NMR and MS approaches to metabolomics. In: Fan, TW-M.; Lane, AN.; Higashi, RM., editors. The Handbook of Metabolomics. Humana; New York: 2012. p. 199-230.
71. Hu K, Ellinger JJ, Chylla RA, Markley JL. Measurement of absolute concentrations of individual compounds in metabolite mixtures by gradient-selective time-zero H-1–C-13 HSQC with two concentration references and fast maximum likelihood reconstruction analysis. Anal Chem. 2011; 83:9352–9360. [PubMed: 22029275]
72. Lane AN, Fan TW. Quantification and identification of isotopomer distributions of metabolites in crude cell extracts using ^{1}H TOCSY. Metabolomics. 2007; 3:79–86.
73. Fan TW, Lane AN. Structure-based profiling of metabolites and isotopomers by NMR. Progr NMR Spectrosc. 2008; 52:69–117.
74. Le A, Lane AN, Hamaker M, Bose S, Barbi J, Tsukamoto T, Rojas CJ, Slusher BS, Zhang H, Zimmerman LJ, Liebler DC, Slebos RJC, Lorkiewicz PK, Higashi RM, Fan TW-M, Dang CV. Myc induction of hypoxic glutamine metabolism and a glucose-independent TCA cycle in human B lymphocytes. Cell Metab. 2012; 15:110–121. [PubMed: 22225880]
75. Hoult DI, Richards RE. The signal-to-noise ratio of the nuclear magnetic resonance experiment. J Magn Reson. 1969; 24:71–85.
76. Ramaswamy V, Hooker JW, Withers RS, Nast RE, Brey WW, Edison AS. Development of a C-13-optimized 1.5-mm high temperature superconducting NMR probe. J Magn Reson. 2013; 235:58–65. [PubMed: 23969086]
77. Brey WW, Edison AE, Nast RE, Rocca JR, Saha S, Withers RS. Design, construction, and validation of a 1-mm triple-resonance high-temperature-superconducting probe for NMR. J Magn Res. 2006; 179:290–293.
78. Henry EB. Osmolarity of human serum and of chemical solutions of biologic importance. Clin Chem. 1961; 7:156–164.
79. Lane, AN. The stability of intramolecular DNA quadruplexes compared with other macromolecules. Biochimie. 2011. http://dx.doi.org/10.1016/j.biochi.2011.08.004
80. Lane AN, Arumugam S. Improving NMR sensitivity in room temperature and cooled probes with dipolar ions. J Magn Reson. 2005; 173:339–343. [PubMed: 15780927]
81. Fan TWM, Higashi RM, Frenkiel TA, Lane AN. Anaerobic nitrate and ammonium metabolism in flood-tolerant rice coleoptiles. J Exp Bot. 1997; 48:1655–1666.
82. Ippel J, Wijmenga S, de Jong B, Heus H, Hilbers C, Vroom E, van de Marel C, van Boom J. Heteronuclear scalar couplings in the bases and sugar rings of nucleic acids: their determination and application in assignment and conformational analysis. Magn Reson Chem. 1996; 34:S156–S176.
83. Lane AN, Arumugam S, Lorkiewicz PK, Higashi RM, Laulhe S, Nantz MH, Moseley HNB, Fan TW-M. Chemoselective detection of carbonyl compounds in metabolite mixtures by NMR. Magn Res Chem. 2015
84. Fan TW-M, Lane AN. NMR-based stable isotope resolved metabolomics in systems biochemistry. J Biomol NMR. 2011; 49:267–280. [PubMed: 21350847]
85. Malloy, CR.; Maher, E.; Marin-Valenica, I.; Mickey, B.; DeBerardinis, RJ.; Sherry, AD. Carbon-13 nuclear magnetic resonance for analysis of metabolic pathways. In: Lutz, N.; Sweedler, JV.; Weevers, RA., editors. Methodologies for Metabolomics: Experimental Strategies and Techniques. Cambridge University Press; Cambridge: 2013. p. 415-445.
86. Williamson RT, Buevich AV, Martin GE. Using LR-HSQMBC to observe long-range H-1–N-15 correlations. Tetrahedron Lett. 2014; 55:3365–3366.
87. Martin GE, Blinov KA, Williamson RT. HMBC-1,n-ADEQUATE spectra calculated from HMBC and 1,n-ADEQUATE spectra. Magn Reson Chem. 2013; 51:299–307. [PubMed: 23483673]
88. Mueller D, Heinzle E. Stable isotope-assisted metabolomics to detect metabolic flux changes in mammalian cell cultures. Curr Opin Biotechnol. 2013; 24:54–59. [PubMed: 23142545]

89. Wiechert W, Noh K. Isotopically non-stationary metabolic flux analysis: complex yet highly informative. Curr Opin Biotechnol. 2013; 24:979–986. [PubMed: 23623747]

90. Moseley HNB, Lane AN, Belshoff AC, Higashi RM, Fan TW-M. Non-steady state modeling of UDP-GlcNAc biosynthesis is enabled by stable isotope resolved metabolomics (SIRM). BMC Biol. 2011; 9:37. [PubMed: 21627825]

91. Yang, TH. Metabolic flux analysis. In: Fan, TW.; Lane, AN.; Higashi, RM., editors. The Handbook of Metabolomics. Humana; Totoya: 2012. p. 231-277.

92. Brindle KM. Imaging metabolism with hyperpolarized C-13-labeled cell substrates. J Am Chem Soc. 2015; 137:6418–6427. [PubMed: 25950268]

93. Niedenfuhr S, Wiechert W, Noh K. How to measure metabolic fluxes: a taxonomic guide for (13)C fluxomics. Curr Opin Biotechnol. 2015; 34:82– 90. [PubMed: 25531408]

94. Buescher JM, Antoniewicz MR, Boros LG, Burgess SC, Brunengraber H, Clish CB, DeBerardinis RJ, Feron O, Frezza C, Ghesquiere B, Gottlieb E, Hiller K, Jones RG, Kamphorst JJ, Kibbey RG, Kimmelman AC, Locasale JW, Lunt SY, Maddocks OD, Malloy C, Metallo CM, Meuillet EJ, Munger J, Noh K, Rabinowitz JD, Ralser M, Sauer U, Stephanopoulos G, St-Pierre J, Tennant DA, Wittmann C, Vander Heiden MG, Vazquez A, Vousden K, Young JD, Zamboni N, Fendt S-M. A roadmap for interpreting (13)C metabolite labeling patterns from cells. Curr Opin Biotechnol. 2015; 34:189–201. [PubMed: 25731751]

95. Fendt S-M, Bell EL, Keibler MA, Olenchock BA, Mayers JR, Wasylenko TM, Vokes NI, Guarente L, Vander Heiden MG, Stephanopoulos G. Reductive glutamine metabolism is a function of the alpha-ketoglutarate to citrate ratio in cells. Nat Commun. 2013; 4

96. Fan TWM, Lane AN, Higashi RM. In vivo and in vitro metabolomic analysis of anaerobic rice coleoptiles revealed unexpected pathways. Russ J Plant Physiol. 2003; 50:787–793.

97. Fan TW, Lane AN, Higashi RM, Farag MA, Gao H, Bousamra M, Miller DM. Altered regulation of metabolic pathways in human lung cancer discerned by (13)C stable isotope-resolved metabolomics (SIRM). Mol Cancer. 2009; 8:41. [PubMed: 19558692]

98. Le A, Lane AN, Hamaker M, Bose S, Gouw A, Barbi J, Tsukamoto T, Rojas CJ, Slusher BS, Zhang H, Zimmerman LJ, Liebler DC, Slebos RJ, Lorkiewicz PK, Higashi RM, Fan TW, Dang CV. Glucose-independent glutamine metabolism via TCA cycling for proliferation and survival in B cells. Cell Metab. 2012; 15:110–121. [PubMed: 22225880]

99. Liu W, Le A, Hancock C, Lane AN, Dang CV, Fan TW, Phang JM. Reprogramming of proline and glutamine metabolism contributes to the proliferative and metabolic responses regulated by oncogenic transcription factor c-MYC. Proc Natl Acad Sci USA. 2012; 109:8983–8988. [PubMed: 22615405]

100. Yang Y, Lane AN, Ricketts CJ, Sourbier C, Wei MH, Shuch B, Pike L, Wu M, Rouault TA, Boros LG, Fan TW, Linehan WM. Metabolic reprogramming for producing energy and reducing power in fumarate hydratase null cells from hereditary leiomyomatosis renal cell carcinoma. PLoS ONE. 2013; 8:e72179. [PubMed: 23967283]

101. Xie H, Hanai JI, Ren JG, Kats L, Burgess K, Bhargava P, Signoretti S, Billiard J, Duffy KJ, Grant A, Wang X, Lorkiewicz PK, Schatzman S, Bousamra M 2nd, Lane AN, Higashi RM, Fan TW, Pandolfi PP, Sukhatme VP, Seth P. Targeting lactate dehydrogenase-A inhibits tumorigenesis and tumor progression in mouse models of lung cancer and impacts tumor-initiating cells. Cell Metab. 2014; 19:1–15. [PubMed: 24411934]

102. Dong C, Yuan T, Wu Y, Wang Y, Fan TW, Miriyala S, Lin Y, Yao J, Shi J, Kang T, Lorkiewicz P, St Clair D, Hung MC, Evers BM, Zhou BP. Loss of FBP1 by snail-mediated repression provides metabolic advantages in basal-like breast cancer. Cancer Cell. 2013; 23:316–331. [PubMed: 23453623]

103. Ren JG, Seth P, Clish CB, Lorkiewicz PK, Higashi RM, Lane AN, Fan TW, Sukhatme VP. Knockdown of malic enzyme 2 suppresses lung tumor growth, induces differentiation and impacts PI3K/AKT signaling. Sci Rep. 2014; 4:5414. [PubMed: 24957098]

104. Guin S, Pollard C, Ru Y, Ritterson Lew C, Duex JE, Dancik G, Owens C, Spencer A, Knight S, Holemon H, Gupta S, Hansel D, Hellerstein M, Lorkiewicz P, Lane AN, Fan TW, Theodorescu D. Role in tumor growth of a glycogen debranching enzyme lost in glycogen storage disease. J Natl Cancer Inst. 2014; 106

105. Fan TW, Lane AN, Higashi RM, Yan J. Stable isotope resolved metabolomics of lung cancer in a SCID mouse model. Metabolomics. 2011; 7:257–269. [PubMed: 21666826]
106. Fan TW, Yuan P, Lane AN, Higashi RM, Wang Y, Hamidi AB, Zhou R, Guitart X, Chen G, Manji HK, Kaddurah-Daouk R. Stable isotope-resolved metabolomic analysis of lithium effects on glial-neuronal metabolism and interactions. Metabolomics. 2010; 6:165–179. [PubMed: 20631920]
107. Sellers K, Fox MP, Bousamra M II, Slone SP, Higashi RM, Miller DM, Wang Y, Yan J, Yuneva MO, Deshpande R, Lane AN, Fan TWM. Pyruvate carboxylase is critical for non-small-cell lung cancer proliferation. J Clin Invest. 2015; 125:687–698. [PubMed: 25607840]
108. Fan T, Bandura L, Higashi R, Lane A. Metabolomics-edited transcriptomics analysis of Se anticancer action in human lung cancer cells. Metabolomics. 2005; 1:325–339.
109. Chang K, Roberts JKM. Quantitation of rates of transport, metabolic fluxes, and cytoplasmic levels of inorganic carbon in maize root tips during potassium ion uptake. Plant Physiol (Rockville). 1992; 99:291–297. [PubMed: 16668864]
110. Ugurbil K, Brown TR, Den Hollander JA, Glynn P, Shulman RG. High-resolution ^{13}C nuclear magnetic resonance studies of glucose metabolism in *Escherichia coli*. Proc Natl Acad Sci. 1978; 75:3742–3746. [PubMed: 358201]
111. Lu D, Mulder H, Zhao P, Burgess SC, Jensen MV, Kamzolova S, Newgard CB, Sherry AD. ^{13}C NMR isotopomer analysis reveals a connection between pyruvate cycling and glucose-stimulated insulin secretion (GSIS). Proc Natl Acad Sci USA. 2002; 99:2708–2713. [PubMed: 11880625]
112. Lundberg P, Ekblad A, Nilsson M. ^{13}C NMR spectroscopy studies of forest soil microbial activity: glucose uptake and fatty acid biosynthesis. Soil Biol Biochem. 2001; 33:621–632.
113. Szyperski T. ^{13}C NMR, MS and metabolic flux balancing in biotechnology research. Quart Rev Biophys. 1998; 31:41–106.
114. Portais J-C, Schuster R, Merle M, Canioni P. Metabolic flux determination in C6 glioma cells using carbon-13 distribution upon (1-^{13}C)glucose incubation. Eur J Biochem. 1993; 217:457–468. [PubMed: 7901007]
115. Liu KJM, Kleps R, Henderson T, Nyhus L. C-13 NMR-study of hepatic pyruvate-carboxylase activity in tumor rats. Biochem Biophys Res Commun. 1991; 179:366–371. [PubMed: 1883366]
116. Sonnewald U, Kondziella D. Neuronal glial interaction in different neurological diseases studied by ex vivo ^{13}C NMR spectroscopy. NMR Biomed. 2003; 16:424–429. [PubMed: 14679504]
117. Yang C, Richardson A, Osterman A, Smith J. Profiling of central metabolism in human cancer cells by two-dimensional NMR, GC–MS analysis, and isotopomer modeling. Metabolomics. 2008
118. Delgado TC, Castro MM, Geraldes CF, Jones JG. Quantitation of erythrocyte pentose pathway flux with [2-^{13}C]glucose and ^{1}H NMR analysis of the lactate methyl signal. Magn Reson Med. 2004; 51:1283–1286. [PubMed: 15170851]
119. Mancuso A, Beardsley NJ, Wehrli S, Pickup S, Matschinsky FM, Glickson JD. Real-time detection of ^{13}C NMR labeling kinetics in perfused EMT6 mouse mammary tumor cells and betaHC9 mouse insulinomas. Biotechnol Bioeng. 2004; 87:835–848. [PubMed: 15334410]
120. Oh-hama T, Seto H, Miyachi S. ^{13}C-NMR evidence of bacteriochlorophyll a formation by the C5 pathway in *Chromatium*. Arch Biochem Biophys. 1986; 246:192–198. [PubMed: 3963821]
121. Jones JG, Solomon MA, Cole SM, Sherry AD, Malloy CR. An integrated (2) H and (13)C NMR study of gluconeogenesis and TCA cycle flux in humans. Am J Physiol Endocrinol Metab. 2001; 281:E848–E856. [PubMed: 11551863]
122. Gruetter R, Magnusson I, Rothman DL, Avison MJ, Shulman RG, Shulman GI. Validation of ^{13}C NMR measurements of liver glycogen in vivo. Magn Reson Med. 1994; 31:583–588. [PubMed: 8057810]
123. Artemov D, Bhujwalla ZM, Pilatus U, Glickson JD. Two-compartment model for determination of glycolytic rates of solid tumors by in vivo ^{13}C NMR spectroscopy. NMR Biomed. 1998; 11:395–404. [PubMed: 10221582]
124. Bhujwalla ZM, Shungu DC, Chatham JC, Wehrle JP, Glickson JD. Glucose metabolism in RIF-1 tumors after reduction in blood flow: an in vivo ^{13}C and ^{31}P NMR study. Magn Reson Med. 1994; 32:303–309. [PubMed: 7984062]

125. Gruetter R, Adriany G, Choi IY, Henry PG, Lei H, Oz G. Localized in vivo ^{13}C NMR spectroscopy of the brain. NMR Biomed. 2003; 16:313–338. [PubMed: 14679498]
126. Choi IY, Gruetter R. In vivo ^{13}C NMR assessment of brain glycogen concentration and turnover in the awake rat. Neurochem Int. 2003; 43:317–322. [PubMed: 12742075]
127. Price TB, Rothman DL, Avison MJ, Buonamico P, Shulman RG. ^{13}C NMR measurements of muscle glycogen during low-intensity exercise. J Appl Physiol. 1991; 70:1836–1844. [PubMed: 2055862]
128. Mancuso A, Sharfstein ST, Tucker SN, Clark DS, Blanch HW. Examination of primary metabolic pathways in a murine hybridoma with carbon-13 nuclear magnetic resonance spectroscopy. Biotechnol Bioeng. 1994; 44:563–585. [PubMed: 18618793]
129. DeBerardinis RJ, Mancuso A, Daikhin E, Nissim I, Yudkoff M, Wehrli S, Thompson CB. Beyond aerobic glycolysis: transformed cells can engage in glutamine metabolism that exceeds the requirement for protein and nucleotide synthesis. Proc Natl Acad Sci USA. 2007; 104:19345–19350. [PubMed: 18032601]
130. de Graaf RA, Rothman DL, Behar KL. State of the art direct ^{13}C and indirect ^{1}H–[^{13}C] NMR spectroscopy in vivo. A practical guide. NMR Biomed. 2011; 24:958–972. [PubMed: 21919099]
131. Rothman DL, De Feyter HM, de Graaf RA, Mason GF, Behar KL. ^{13}C MRS studies of neuroenergetics and neurotransmitter cycling in humans. NMR Biomed. 2011; 24:943–957. [PubMed: 21882281]
132. Cunnane S, Likhodii S, Moine G. In vivo ^{13}C nuclear magnetic resonance: applications and current limitations for noninvasive assessment of fatty acid status. Lipids. 1996; 31:S127–S130. [PubMed: 8729106]
133. Lapidot A, Gopher A. Cerebral metabolic compartmentation. Estimation of glucose flux via pyruvate carboxylase/pyruvate dehydrogenase by ^{13}C NMR isotopomer analysis of D-[U-^{13}C]glucose metabolites. J Biol Chem. 1994; 269:27198–27208. [PubMed: 7961629]
134. Artemov D, Bhujwalla ZM, Glickson JD. In vivo selective measurement of (1-^{13}C)-glucose metabolism in tumors by heteronuclear cross polarization. Magn Reson Med. 1995; 33:151–155. [PubMed: 7707903]
135. Kaplan O, Firon M, Vivi A, Navon G, Tsarfaty I. HGF/SF activates glycolysis and oxidative phosphorylation in DA3 murine mammary cancer cells. Neoplasia. 2000; 2:365–377. [PubMed: 11005571]
136. Carvalho RA, Rodrigues TB, Zhao PY, Jeffrey FMH, Malloy CR, Sherry AD. A C-13 isotopomer kinetic analysis of cardiac metabolism: influence of altered cytosolic redox and [Ca^{2+}](o). Am J Physiol – Heart Circul Physiol. 2004; 287:H889–H895.
137. Dobbins RL, Malloy CR. Measuring in-vivo metabolism using nuclear magnetic resonance. Curr Opin Clin Nutr Metab Care. 2003; 6:501–509. [PubMed: 12913667]
138. Jin ES, Jones JG, Burgess SC, Merritt ME, Sherry AD, Malloy CR. Comparison of [3,4-C-13(2)]glucose to [6,6-H-2(2)]glucose as a tracer for glucose turnover by nuclear magnetic resonance. Magn Reson Med. 2005; 53:1479–1483. [PubMed: 15906303]
139. Sherry AD, Jeffrey FMH, Malloy CR. Analytical solutions for C-13 isotopomer analysis of complex metabolic conditions: substrate oxidation, multiple pyruvate cycles, and gluconeogenesis. Metab Eng. 2004; 6:12–24. [PubMed: 14734252]
140. Jin ES, Jones JG, Merritt M, Burgess SC, Malloy CR, Sherry AD. Glucose production, gluconeogenesis, and hepatic tricarboxylic acid cycle fluxes measured by nuclear magnetic resonance analysis of a single glucose derivative. Anal Biochem. 2004; 327:149–155. [PubMed: 15051530]
141. Lane AN, Fan TW, Xie Z, Moseley HN, Higashi RM. Isotopomer analysis of lipid biosynthesis by high resolution mass spectrometry and NMR. Anal Chim Acta. 2009; 651:201–208. [PubMed: 19782812]
142. Lane AN, Arumugam S, Lorkiewicz PK, Higashi RM, Laulhe S, Nantz MH, Moseley HNB, Fan TWM. Chemoselective detection and discrimination of carbonyl-containing compounds in metabolite mixtures by ^{1}H-detected ^{15}N nuclear magnetic resonance. Magn Reson Chem. 2015; 53:337–343. [PubMed: 25616249]

143. Clore GM, Gronenborn AM. NMR structure determination of proteins and protein complexes larger than 20 kDa. Curr Opin Chem Biol. 1998; 2:564– 570. [PubMed: 9818180]

144. Bax A. Multidimensional nuclear-magnetic-resonance methods for protein studies. Curr Opin Struct Biol. 1994; 4:738–744.

145. Ikura M, Bax A. Isotope-filtered 2d NMR of a protein peptide complex – study of a skeletal-muscle myosin light chain kinase fragment bound to calmodulin. J Am Chem Soc. 1992; 114:2433–2440.

146. Otting G, Wuthrich K. Heteronuclear filters in 2-dimensional H-1, H-1 NMR-spectroscopy – combined use with isotope labeling for studies of macromolecular conformation and intermolecular interactions. Q Rev Biophys. 1990; 23:39–96. [PubMed: 2160666]

147. McIntosh LP, Dahlquist FW. Biosynthetic incorporation of N-15 and C-13 for assignment and interpretation of nuclear-magnetic-resonance spectra of proteins. Q Rev Biophys. 1990; 23:1–38. [PubMed: 2188278]

148. Fesik SW, Zuiderweg ERP. Heteronuclear 3-dimensional NMR-spectroscopy of isotopically labeled biological macromolecules. Q Rev Biophys. 1990; 23:97–131. [PubMed: 2188281]

149. Senn H, Otting G, Wuthrich K. Protein-structure and interactions by combined use of sequential NMR assignments and isotope labeling. J Am Chem Soc. 1987; 109:1090–1092.

150. Gardner KH, Kay LE. The use of H-2, C-13, N-15 multidimensional NMR to study the structure and dynamics of proteins. Annu Rev Biophys Biomol Struct. 1998; 27:357–406. [PubMed: 9646872]

151. Qin J, Clore GM, Gronenborn AM. Ionization equilibria for side-chain carboxyl groups in oxidized and reduced human thioredoxin and in the complex with its target peptide from the transcription factor NF kappa B. Biochemistry. 1996; 35:7–13. [PubMed: 8555200]

152. Jeng MF, Dyson HJ. Direct measurement of the aspartic acid 26 pK(a) for reduced *Escherichia coli* thioredoxin by C-13 NMR. Biochemistry. 1996; 35:1–6. [PubMed: 8555161]

153. Levitt MH, Ernst RR. Improvement of pulse performance in N.M.R. coherence transfer experiments. Mol Phys. 1983; 50:1109–1124.

154. Hoch JC, Maciejewski MW, Mobli M, Schuyler AD, Stern AS. Nonuniform sampling and maximum entropy reconstruction in multidimensional NMR. Acc Chem Res. 2014; 47:708–717. [PubMed: 24400700]

155. Freeman R, Kupče Ē. Distant echoes of the accordion: reduced dimensionality, GFT-NMR, and projection–reconstruction of multidimensional spectra. Conc Magn Reson A. 2004; 23A:63–75.

156. Szyperski T, Atreya HS. Principles and applications of GFT projection NMR spectroscopy. Magn Reson Chem. 2006; 44:S51–S60. [PubMed: 16826541]

157. Carvalho RA, Jeffrey FMH, Sherry AD, Malloy CR. C-13 isotopomer analysis of glutamate by heteronuclear multiple quantum coherence total correlation spectroscopy (HMQC-TOCSY). FEBS Lett. 1998; 440:382–386. [PubMed: 9872407]

158. Lenox, RH.; Kant, GJ.; Meyerhoff, JL. Rapid enzyme inactivation. In: Lajtha, A., editor. Handbook of Neurochemistry. Plenum Press; New York: 1982. p. 77-102.

159. Wollenberger A, Ristau O, Schoffa G. Eine einfache Technik der extrem schnellen Abkuhlung groserer Gewebestucke. Pflugers Arch. 1960; 270:399–412.

160. Lazzarino G, Nuutinen M, Tavazzi B, Di Pierro D, Giardina B. A method for preparing freeze-clamped tissue samples for metabolite analyses. Anal Biochem. 1989; 181:239–241. [PubMed: 2817387]

161. Teng Q, Huang W, Collette T, Ekman D, Tan C. A direct cell quenching method for cell-culture based metabolomics. Metabolomics. 2009; 5:199– 208.

162. de Koning W, van Dam K. A method for the determination of changes of glycolytic metabolites in yeast on a subsecond time scale using extraction at neutral pH. Anal Biochem. 1992; 204:118–123. [PubMed: 1514678]

163. Winder CL, Dunn WB, Schuler S, Broadhurst D, Jarvis R, Stephens GM, Goodacre R. Global metabolic profiling of *Escherichia coli* cultures: an evaluation of methods for quenching and extraction of intracellular metabolites. Anal Chem. 2008; 80:2939–2948. [PubMed: 18331064]

164. Sellick CA, Hansen R, Maqsood AR, Dunn WB, Stephens GM, Goodacre R, Dickson AJ. Effective quenching processes for physiologically valid metabolite profiling of suspension cultured mammalian cells. Anal Chem. 2009; 81:174–183. [PubMed: 19061395]
165. Villas-Boas SG, Bruheim P. Cold glycerol-saline: the promising quenching solution for accurate intracellular metabolite analysis of microbial cells. Anal Biochem. 2007; 370:87–97. [PubMed: 17643383]
166. Buchholz A, Hurlebaus J, Wandrey C, Takors R. Metabolomics: quantification of intracellular metabolite dynamics. Biomol Eng. 2002; 19:5–15. [PubMed: 12103361]
167. Bolten CJ, Kiefer P, Letisse F, Portais JC, Wittmann C. Sampling for metabolome analysis of microorganisms. Anal Chem. 2007; 79:3843–3849. [PubMed: 17411014]
168. Link H, Anselment B, Weuster-Botz D. Leakage of adenylates during cold methanol/glycerol quenching of *Escherichia coli*. Metabolomics. 2008; 4:240– 247.
169. Kruger NJ, Troncoso-Ponce MA, Ratcliffe RG. ^{1}H NMR metabolite fingerprinting and metabolomic analysis of perchloric acid extracts from plant tissues. Nat Protoc. 2008; 3:1001–1012. [PubMed: 18536647]
170. Moreno A, Arus C. Quantitative and qualitative characterization of H-1 NMR spectra of colon tumors, normal mucosa and their perchloric acid extracts: decreased levels of myo-inositol in tumours can be detected in intact biopsies. NMR Biomed. 1996; 9:33–45. [PubMed: 8842031]
171. Flogel U, Willker W, Engelmann J, Niendorf T, Leibfritz D. Adaptation of cellular metabolism to anisosmotic conditions in a glial cell line, as assessed by C-13-NMR spectroscopy. Dev Neurosci. 1996; 18:449–459. [PubMed: 8940618]
172. Martinez-Bisbal MC, Marti-Bonmati L, Piquer J, Revert A, Ferrer P, Llacer JL, Piotto M, Assemat O, Celda B. H-1 and C-13 HR-MAS spectroscopy of intact biopsy samples ex vivo and in vivo H-1 MRS study of human high grade gliomas. NMR Biomed. 2004; 17:191–205. [PubMed: 15229932]
173. Reszko AE, Kasumov T, Comte B, Pierce BA, David F, Bederman IR, Deutsch J, Des Rosiers C, Brunengraber H. Assay of the concentration and ^{13}C-isotopic enrichment of malonyl-coenzyme A by gas chromatography–mass spectrometry. Anal Biochem. 2001; 298:69–75. [PubMed: 11673897]
174. Berners-Price SJ, Sant ME, Christopherson RI, Kuchel PW. ^{1}H and ^{31}P NMR and HPLC studies of mouse L1210 Leukemia cell extracts: the effect of Au(I) and Cu(I) diphosphine complexes on the cell metabolism. Magn Reson Med. 1991; 18:142–158. [PubMed: 2062226]
175. Faijes M, Mars A, Smid E. Comparison of quenching and extraction methodologies for metabolome analysis of *Lactobacillus plantarum*. Microb Cell Fact. 2007; 6:27. [PubMed: 17708760]
176. Higashi RM, Fan TWM, Macdonald JM. Monitoring of metabolic responses of intact haliotis (abalones) under salinity stress by P-31 surface probe localized NMR. J Exp Zool. 1989; 249:350–356. [PubMed: 2708953]
177. Fan TW, Kucia M, Jankowski K, Higashi RM, Ratajczak J, Ratajczak MZ, Lane AN. Rhabdomyosarcoma cells show an energy producing anabolic metabolic phenotype compared with primary myocytes. Mol Cancer. 2008; 7:79. [PubMed: 18939998]
178. Fan TW-M, Tan JL, McKinney MM, Lane AN. Stable isotope resolved metabolomics analysis of ribonucleotide and RNA metabolism in human lung cancer cells. Metabolomics. 2012; 8:517–527. [PubMed: 26146495]
179. Lorkiewicz P, Higashi RM, Lane AN, Fan TW. High information throughput analysis of nucleotides and their isotopically enriched isotopologues by direct-infusion FTICR-MS. Metab: Off J Metab Soc. 2012; 8:930–939.
180. Moseley HN, Lane AN, Belshoff AC, Higashi RM, Fan TW. A novel deconvolution method for modeling UDP-N-acetyl-D-glucosamine biosynthetic pathways based on (13)C mass isotopologue profiles under non-steady-state conditions. BMC Biol. 2011; 9:37. [PubMed: 21627825]
181. Sloth JJ, Larsen EH, Julshamn K. Determination of organoarsenic species in marine samples using gradient elution cation exchange HPLC-ICP-MS. J Anal At Spectrom. 2003; 18:452–459.

182. Villas-Boas SG, Hojer-Pedersen J, Akesson M, Smedsgaard J, Nielsen J. Global metabolite analysis of yeast: evaluation of sample preparation methods. Yeast. 2005; 22:1155–1169. [PubMed: 16240456]

183. Yang L, Kasumov T, Yu L, Jobbins KA, David F, Previs SF, Kelleher JK, Brunengraber H. Metabolomic assays of the concentration and mass isotopomer distribution of gluconeogenic and citric acid cycle intermediates. Metabolomics. 2006; 2:1573–3882.

184. Want EJ, O'Maille G, Smith CA, Brandon TR, Uritboonthai W, Qin C, Trauger SA, Siuzdak G. Solvent-dependent metabolite distribution, clustering, and protein extraction for serum profiling with mass spectrometry. Anal Chem. 2006; 78:743–752. [PubMed: 16448047]

185. Wittmann C, Kromer JO, Kiefer P, Binz T, Heinzle E. Impact of the cold shock phenomenon on quantification of intracellular metabolites in bacteria. Anal Biochem. 2004; 327:135–139. [PubMed: 15033521]

186. Winder CL, Dunn WB, Schuler S, Broadhurst D, Jarvis R, Stephens GM, Goodacre R. Global metabolic profiling of *Escherichia coli* cultures: an evaluation of methods for quenching and extraction of intracellular metabolites. Anal Chem. 2008; 80:2939–2948. [PubMed: 18331064]

187. De Vos RC, Moco S, Lommen A, Keurentjes JJ, Bino RJ, Hall RD. Untargeted large-scale plant metabolomics using liquid chromatography coupled to mass spectrometry. Nat Protoc. 2007; 2:778–791. [PubMed: 17446877]

188. Rabinowitz JD, Kimball E. Acidic acetonitrile for cellular metabolome extraction from *Escherichia coli*. Anal Chem. 2007; 79:6167–6173. [PubMed: 17630720]

189. Kimball E, Rabinowitz JD. Identifying decomposition products in extracts of cellular metabolites. Anal Biochem. 2006; 358:273–280. [PubMed: 16962982]

190. Ritter JB, Genzel Y, Reichl U. Simultaneous extraction of several metabolites of energy metabolism and related substances in mammalian cells: optimization using experimental design. Anal Biochem. 2008; 373:349–369. [PubMed: 18036549]

191. Wittmann C, Kromer JO, Kiefer P, Binz T, Heinzle E. Impact of the cold shock phenomenon on quantification of intracellular metabolites in bacteria. Anal Biochem. 2004; 327:135–139. [PubMed: 15033521]

192. Paglia G, Magnusdottir M, Thorlacius S, Sigurjonsson OE, Guethmundsson S, Palsson BO, Thiele I. Intracellular metabolite profiling of platelets: evaluation of extraction processes and chromatographic strategies. J Chromatogr B: Anal Technol Biomed Life Sci. 2012; 898:111–120.

193. Yang Y, Cruickshank C, Armstrong M, Mahaffey S, Reisdorph R, Reisdorph N. New sample preparation approach for mass spectrometry-based profiling of plasma results in improved coverage of metabolome. J Chromatogr A. 2013; 1300:217–226. [PubMed: 23672979]

194. Matyash V, Liebisch G, Kurzchalia TV, Shevchenko A, Schwudke D. Lipid extraction by methyl-tert-butyl ether for high-throughput lipidomics. J Lipid Res. 2008; 49:1137–1146. [PubMed: 18281723]

195. Abbott SK, Jenner AM, Mitchell TW, Brown SH, Halliday GM, Garner B. An improved high-throughput lipid extraction method for the analysis of human brain lipids. Lipids. 2013; 48:307–318. [PubMed: 23355308]

196. Reis A, Rudnitskaya A, Blackburn GJ, Fauzi NM, Pitt AR, Spickett CM. A comparison of five lipid extraction solvent systems for lipidomic studies of human LDL. J Lipid Res. 2013; 54:1812–1824. [PubMed: 23670529]

197. Folch J, Lees M, Sloane Stanley GH. A simple method for the isolation and purification of total lipides from animal tissues. J Biol Chem. 1957; 226:497–509. [PubMed: 13428781]

198. Ye T, Mo H, Shanaiah N, Gowda GA, Zhang S, Raftery D. Chemoselective ^{15}N tag for sensitive and high-resolution nuclear magnetic resonance profiling of the carboxyl-containing metabolome. Anal Chem. 2009; 81:4882–4888. [PubMed: 19518144]

199. Tayyari F, Gowda GA, Gu H, Raftery D. ^{15}N-cholamine – a smart isotope tag for combining NMR- and MS-based metabolite profiling. Anal Chem. 2013; 85:8715–8721. [PubMed: 23930664]

200. Gowda GA, Tayyari F, Ye T, Suryani Y, Wei S, Shanaiah N, Raftery D. Quantitative analysis of blood plasma metabolites using isotope enhanced NMR methods. Anal Chem. 2010

201. Gori SS, Lorkiewicz P, Ehringer DS, Belshoff AC, Higashi RM, Fan TW, Nantz MH. Profiling thiol metabolites and quantification of cellular glutathione using FT-ICR-MS spectrometry. Anal Bioanal Chem. 2014; 406:4371–4379. [PubMed: 24858467]

202. Moestue S, Sitter B, Bathen T, Tessem M, Gribbestad I. HR MAS MR spectroscopy in metabolic characterization of cancer. Curr Top Med Chem. 2011; 11:2–26. [PubMed: 20809888]

203. Griffin JL, Blenkiron C, Valonen PK, Caldas C, Kauppinen RA. High-resolution magic angle spinning H-1 NMR spectroscopy and reverse transcription-PCR analysis of apoptosis in a rat glioma. Anal Chem. 2006; 78:1546–1552. [PubMed: 16503606]

204. Imperiale A, Moussallieh F-M, Roche P, Battini S, Cicek AE, Sebag F, Brunaud L, Barlier A, Elbayed K, Loundou A, Bachellier P, Goichot B, Stratakis CA, Pacak K, Namer I-J, Taieb d. Metabolome profiling by HRMAS NMR spectroscopy of pheochromocytomas and paragangliomas detects SDH deficiency: clinical and pathophysiological implications. Neoplasia. 2015; 17:55–65. [PubMed: 25622899]

205. Solinas A, Chessa M, Culeddu N, Porcu MC, Virgilio G, Arcadu F, Deplano A, Cossu S, Scanu D, Migaleddu V. High resolution-magic angle spinning (HR-MAS) NMR-based metabolomic fingerprinting of early and recurrent hepatocellular carcinoma. Metabolomics. 2014; 10:616–626.

206. Benahmed MA, Elbayed K, Daubeuf F, Santelmo N, Frossard N, Namer IJ. NMR HRMAS spectroscopy of lung biopsy samples: comparison study between human, pig, rat, and mouse metabolomics. Magn Reson Med. 2014; 71:35–43. [PubMed: 23412987]

207. Somashekar BS, Amin AG, Rithner CD, Troudt J, Basaraba R, Izzo A, Crick DC, Chatterjee D. Metabolic profiling of lung granuloma in mycobacterium tuberculosis infected guinea pigs: ex vivo H-1 magic angle spinning NMR studies. J Proteome Res. 2011; 10:4186–4195. [PubMed: 21732701]

208. Simon G, Kervarec N, Cerantola S. HRMAS NMR analysis of algae and identification of molecules of interest via conventional 1D and 2D NMR: sample preparation and optimization of experimental conditions. Methods Mol Biol (Clifton, NJ). 2015; 1308:191–205.

209. Palomino-Schaetzlein M, Micaela Molina-Navarro M, Tormos-Perez M, Rodriguez-Navarro S, Pineda-Lucena A. Optimised protocols for the metabolic profiling of *S. cerevisiae* by H-1-NMR and HRMAS spectroscopy. Anal Bioanal Chem. 2013; 405:8431–8441. [PubMed: 23942588]

210. Valentini M, Ritota M, Cafiero C, Cozzolino S, Leita L, Sequi P. The HRMAS-NMR tool in foodstuff characterisation. Magn Reson Chem. 2011; 49:S121– S125. [PubMed: 22290702]

211. Rocha CM, Barros AS, Gil AM, Goodfellow BJ, Humpfer E, Spraul M, Carreira IM, Melo JB, Bernardo J, Gomes A, Sousa V, Carvalho L, Duarte IF. Metabolic profiling of human lung cancer tissue by H-1 high resolution magic angle spinning (HRMAS) NMR spectroscopy. J Proteome Res. 2010; 9:319–332. [PubMed: 19908917]

212. Blaise BJ, Giacomotto J, Triba MN, Toulhoat P, Piotto M, Emsley L, Segalat L, Dumas M-E, Elena B. Metabolic profiling strategy of *Caenorhabditis elegans* by whole-organism nuclear magnetic resonance. J Proteome Res. 2009; 8:2542–2550. [PubMed: 19267476]

213. Coen M, Holmes E, Lindon JC, Nicholson JK. NMR-based metabolic profiling and metabonomic approaches to problems in molecular toxicology. Chem Res Toxicol. 2008; 21:9–27. [PubMed: 18171018]

214. Maher AD, Lindon JC, Nicholson JK. H-1 NMR-based metabonomics for investigating diabetes. Fut Med Chem. 2009; 1:737–747.

215. Smolinska A, Blanchet L, Buydens LMC, Wijmenga SS. NMR and pattern recognition methods in metabolomics: from data acquisition to biomarker discovery: a review. Anal Chim Acta. 2012; 750:82–97. [PubMed: 23062430]

216. Emwas AHM, Salek RM, Griffin JL, Merzaban J. NMR-based metabolomics in human disease diagnosis: applications, limitations, and recommendations. Metabolomics. 2013; 9:1048–1072.

217. Rolin, D.; Deborde, C.; Maucourt, M.; Cabasson, C.; Fauvelle, F.; Jacob, D.; Canlet, C.; Moing, A. High-resolution H-1-NMR spectroscopy and beyond to explore plant metabolome. In: Rolin, D., editor. Metabolomics Coming of Age with Its Technological Diversity. 2013. p. 1-66.

218. Brennan L. NMR-based metabolomics: from sample preparation to applications in nutrition research. Prog Nucl Magn Reson Spectrosc. 2014; 83:42–49. [PubMed: 25456316]

219. Simmler C, Napolitano JG, McAlpine JB, Chen SN, Pauli GF. Universal quantitative NMR analysis of complex natural samples. Curr Opin Biotechnol. 2014; 25:51–59. [PubMed: 24484881]
220. Larive CK, Barding GA, Dinges MM. NMR spectroscopy for metabolomics and metabolic profiling. Anal Chem. 2015; 87:133–146. [PubMed: 25375201]
221. Sobolev AP, Mannina L, Proietti N, Carradori S, Daglia M, Giusti AM, Antiochia R, Capitani D. Untargeted NMR-based methodology in the study of fruit metabolites. Molecules. 2015; 20:4088–4108. [PubMed: 25749679]
222. Tavares LC, Jarak I, Nogueira FN, Oliveira PJ, Carvalho RA. Metabolic evaluations of cancer metabolism by NMR-based stable isotope tracer methodologies. Eur J Clin Invest. 2015; 45:37–43. [PubMed: 25524585]
223. Sellers K, Fox MP, Bousamra M II, Slone SP, Higashi RM, Miller DM, Wang Y, Yan J, Yuneva MO, Deshpande R, Lane AN, Fan TWM. Pyruvate carboxylase is critical for non-small-cell lung cancer proliferation. J Clin Invest. 2015; 125:687–698. [PubMed: 25607840]
224. Fan TW. Considerations of sample preparation for metabolomics investigation. Handb Metab. 2012; 17
225. Lane AN, Fan TW-M. Regulation of mammalian nucleotide metabolism and biosynthesis. Nucleic Acids Res. 2015; 43:2466–2485. [PubMed: 25628363]
226. Weinman EO, Strisower EH, Chaikoff IL. Conversion of fatty acids to carbohydrate; application of isotopes to this problem and role of the Krebs cycle as a synthetic pathway. Physiol Rev. 1957; 37:252–272. [PubMed: 13441426]
227. Strisower EH, Kohler GD, Chaikoff IL. Incorporation of acetate carbon into glucose by liver slices from normal and alloxan-diabetic rats. J Biol Chem. 1952; 198:115–126. [PubMed: 12999723]
228. Rittenberg D, Schoenheimer R. Deuterium as an indicator in study of intermediatory metabolism. VIII. Hydrogenation of fatty acids in the animals organism. J Biol Chem. 1937; 117:485–490.
229. Tjandra N, Omichinski JG, Gronenborn AM, Clore GM, Bax A. Use of dipolar H-1–N-15 and H-1–C-13 couplings in the structure determination of magnetically oriented macromolecules in solution. Nat Struct Biol. 1997; 4:732–738. [PubMed: 9303001]
230. Clore, GM.; Potts, J. Recent Developments in Biomolecular NMR. RSC Publishing; 2012.
231. Barbato G, Ikura M, Kay LE, Pastor RW, Bax A. Backbone dynamics of calmodulin studied by N-15 relaxation using inverse detected 2-dimensional NMR-spectroscopy – the central helix is flexible. Biochemistry. 1992; 31:5269–5278. [PubMed: 1606151]
232. Kupče Ē, Freeman R. Fast multidimensional NMR: radial sampling of evolution space. J Magn Reson. 2005; 173:317–321. [PubMed: 15780924]
233. Pervushin K, Ono A, Fernandez C, Szyperski T, Kainosho M, Wuthrich K. NMR scaler couplings across Watson-Crick base pair hydrogen bonds in DNA observed by transverse relaxation optimized spectroscopy. Proc Natl Acad Sci USA. 1998; 95:14147–14151. [PubMed: 9826668]
234. Bonarius HPJ, Ozemre A, Timmerarends B, Skrabal P, Tramper J, Schmid G, Heinzle E. Metabolic-flux analysis of continuously cultured hybridoma cells using (CO2)-C-13 mass spectrometry in combination with C-13-lactate nuclear magnetic resonance spectroscopy and metabolite balancing. Biotechnol Bioeng. 2001; 74:528–538. [PubMed: 11494221]
235. Cline GW, Lepine RL, Papas KK, Kibbey RG, Shulman GI. ^{13}C NMR isotopomer analysis of anaplerotic pathways in INS-1 cells. J Biol Chem. 2004; 279:44370–44375. [PubMed: 15304488]
236. Zwingmann C, Leibfritz D. Regulation of glial metabolism studied by C-13-NMR. NMR Biomed. 2003; 16:370–399. [PubMed: 14679501]
237. Wahl SA, Dauner M, Wiechert W. New tools for mass isotopomer data evaluation in C-13 flux analysis: mass isotope correction, data consistency checking, and precursor relationships. Biotechnol Bioeng. 2004; 85:259–268. [PubMed: 14748080]
238. Carvalho RA, Zhao P, Wiegers CB, Jeffrey FM, Malloy CR, Sherry AD. TCA cycle kinetics in the rat heart by analysis of (13)C isotopomers using indirect (1)H. Am J Physiol Heart Circ Physiol. 2001; 281:H1413–H1421. [PubMed: 11514314]

239. Chowdhury GM, Banasr M, de Graaf RA, Rothman DL, Behar KL, Sanacora G. Chronic riluzole treatment increases glucose metabolism in rat prefrontal cortex and hippocampus. J Cereb Blood Flow Metab. 2008; 28:1892–1897. [PubMed: 18628780]

240. Yuneva MO, Fan TW, Allen TD, Higashi RM, Ferraris DV, Tsukamoto T, Mates JM, Alonso FJ, Wang C, Seo Y, Chen X, Bishop JM. The metabolic profile of tumors depends on both the responsible genetic lesion and tissue type. Cell Metab. 2012; 15:157–170. [PubMed: 22326218]

241. Warburg O. Is the respiration of cancer cells normal? Biochem Zeitschr. 1924; 51

242. Maher EA, Marin-Valencia I, Bachoo RM, Mashimo T, Raisanen J, Hatanpaa KJ, Jindal A, Jeffrey FM, Choi C, Madden C, Mathews D, Pascual JM, Mickey BE, Malloy CR, DeBerardinis RJ. Metabolism of [U-^{13}C]glucose in human brain tumors in vivo. NMR Biomed. 2012; 25:1234–1244. [PubMed: 22419606]

243. Brindle KM. NMR methods for measuring enzyme kinetics in vivo. Prog Nucl Magn Reson Spectrosc. 1988; 20:257–293.

244. Selenko P, Wagner G. Looking into live cells with in-cell NMR spectroscopy. J Struct Biol. 2007; 158:244–253. [PubMed: 17502240]

245. Grivet J-P, Delort A-M. NMR for microbiology: in vivo and in situ applications. Prog Nucl Magn Reson Spectrosc. 2009; 54:1–53.

246. Weuster-Botz D, de Graaf AA. Reaction engineering methods to study intracellular metabolite concentrations. Adv Biochem Eng Biotechnol. 1996; 54:75–108. [PubMed: 8623615]

247. Ugurbil K, Brown TR, den Hollander JA, Glynn P, Shulman RG. High-resolution ^{13}C nuclear magnetic resonance studies of glucose metabolism in *Escherichia coli*. Proc Natl Acad Sci USA. 1978; 75:3742–3746. [PubMed: 358201]

248. den Hollander JA, Brown TR, Ugurbil K, Shulman RG. ^{13}C nuclear magnetic resonance studies of anaerobic glycolysis in suspensions of yeast cells. Proc Natl Acad Sci USA. 1979; 76:6096–6100. [PubMed: 42910]

249. Hartbrich A, Schmitz G, Weuster-Botz D, de Graaf AA, Wandrey C. Development and application of a membrane cyclone reactor for in vivo NMR spectroscopy with high microbial cell densities. Biotechnol Bioeng. 1996; 51:624–635. [PubMed: 18629829]

250. Tholozan JL, Touzel JP, Samain E, Grivet JP, Prensier G, Albagnac G. *Clostridium neopropionicum* sp. nov., a strict anaerobic bacterium fermenting ethanol to propionate through acrylate pathway. Arch Microbiol. 1992; 157:249–257. [PubMed: 1510558]

251. Majors PD, McLean JS, Pinchuk GE, Fredrickson JK, Gorby YA, Minard KR, Wind RA. NMR methods for in situ biofilm metabolism studies. J Microbiol Methods. 2005; 62:337–344. [PubMed: 15936835]

252. Singer S, Okunieff P, Gostin C, Thilly WG, Chen LB, Neuringer LJ. ^{13}C- and ^{31}P-NMR studies of human colon cancer in-vitro and in-vivo. Surg Oncol. 1993; 2:7–18. [PubMed: 8252195]

253. Shachar-Hill Y, Pfeffer PE, Douds D, Osman SF, Doner LW, Ratcliffe RG. Partitioning of intermediary carbon metabolism in vesicular-arbuscular mycorrhizal leek. Plant Physiol (Rockville). 1995; 108:7–15. [PubMed: 12228450]

254. Fan TWM, Lane AN, Higashi RM. An electrophoretic profiling method for thiol-rich phytochelatins and metallothioneins. Phytochem Anal. 2004; 15:175–183. [PubMed: 15202602]

255. Burgess SC, Babcock EE, Jeffrey FM, Sherry AD, Malloy CR. NMR indirect detection of glutamate to measure citric acid cycle flux in the isolated perfused mouse heart. FEBS Lett. 2001; 505:163–167. [PubMed: 11557062]

256. Hardin CD, Kushmerick MJ. Simultaneous and separable flux of pathways for glucose and glycogen utilization studied by ^{13}C-NMR. J Mol Cell Cardiol. 1994; 26:1197–1210. [PubMed: 7815462]

257. Anousis N, Carvalho RA, Zhao P, Malloy CR, Sherry AD. Compartmentation of glycolysis and glycogenolysis in the perfused rat heart. NMR Biomed. 2004; 17:51–59. [PubMed: 15052552]

258. Morikawa S, Inubushi T, Takahashi K, Shigemori S, Ishii H. Relationship between gluconeogenesis and phosphoenergetics in rat liver assessed by in vivo ^{13}C and ^{31}P NMR spectroscopy. NMR Biomed. 1997; 10:18–24. [PubMed: 9251111]

259. Marin-Valencia I, Cho SK, Rakheja D, Hatanpaa KJ, Kapur P, Mashimo T, Jindal A, Vemireddy V, Good LB, Raisanen J, Sun X, Mickey B, Choi C, Takahashi M, Togao O, Pascual JM,

Deberardinis RJ, Maher EA, Malloy CR, Bachoo RM. Glucose metabolism via the pentose phosphate pathway, glycolysis and Krebs cycle in an orthotopic mouse model of human brain tumors. NMR Biomed. 2012; 25:1177–1186. [PubMed: 22383401]

260. Meric P, Autret G, Doan BT, Gillet B, Sebrie C, Beloeil JC. In vivo 2D magnetic resonance spectroscopy of small animals. MAGMA. 2004; 17:317– 338. [PubMed: 15625585]
261. van Zijl PC, Chesnick AS, DesPres D, Moonen CT, Ruiz-Cabello J, van Gelderen P. In vivo proton spectroscopy and spectroscopic imaging of [1-^{13}C]-glucose and its metabolic products. Magn Reson Med. 1993; 30:544–551. [PubMed: 8259054]
262. Rothman DL, De Feyter HM, de Graaf RA, Mason GF, Behar KL. ^{13}C MRS studies of neuroenergetics and neurotransmitter cycling in humans. NMR Biomed. 2011; 24:943–957. [PubMed: 21882281]
263. Beckmann N, Turkalj I, Seelig J, Keller U. ^{13}C NMR for the assessment of human brain glucose metabolism in vivo. Biochemistry. 1991; 30:6362– 6366. [PubMed: 2054342]
264. Ross B, Lin A, Harris K, Bhattacharya P, Schweinsburg B. Clinical experience with ^{13}C MRS in vivo. NMR Biomed. 2003; 16:358–369. [PubMed: 14679500]
265. Mason GF, Petersen KF, de Graaf RA, Shulman GI, Rothman DL. Measurements of the anaplerotic rate in the human cerebral cortex using C-13 magnetic resonance spectroscopy and [1-C-13] and [2-C-13] glucose. J Neurochem. 2007; 100:73–86. [PubMed: 17076763]
266. Maher EA, Marin-Valencia I, Bachoo RM, Mashimo T, Raisanen J, Hatanpaa KJ, Jindal A, Jeffrey FM, Choi CH, Madden C, Mathews D, Pascual JM, Mickey BE, Malloy CR, DeBerardinis RJ. Metabolism of U-^{13}C glucose in human brain tumors in vivo. NMR Biomed. 2012; 25:1234–1244. [PubMed: 22419606]
267. Mason GF, Petersen KF, de Graaf RA, Kanamatsu T, Otsuki T, Rothman DL. A comparison of C-13 NMR measurements of the rates of glutamine synthesis and the tricarboxylic acid cycle during oral and intravenous administration of 1-C-13 glucose (vol 10, pg 181, 2003). Brain Res Protoc. 2003; 11:143.
268. Golman K, in't Zandt R, Thaning M. Real-time metabolic imaging. Proc Natl Acad Sci USA. 2006; 103:11270–11275. [PubMed: 16837573]
269. Golman K, in't Zandt R, Lerche M, Pehrson R, Ardenkjaer-Larsen JH. Metabolic imaging by hyperpolarized C-13 magnetic resonance imaging for in vivo tumor diagnosis. Cancer Res. 2006; 66:10855–10860. [PubMed: 17108122]
270. Golman K, Petersson JS, Magnusson P, Johansson E, Akeson P, Chai CM, Hansson G, Mansson S. Cardiac metabolism measured noninvasively by hyperpolarized C-13 MRI. Magn Reson Med. 2008; 59:1005–1013. [PubMed: 18429038]
271. Keshari KR, Sriram R, Koelsch BL, Van Criekinge M, Wilson DM, Kurhanewicz J, Wang ZJ. Hyperpolarized C-13-pyruvate magnetic resonance reveals rapid lactate export in metastatic renal cell carcinomas. Cancer Res. 2013; 73:529–538. [PubMed: 23204238]
272. Kurhanewicz J, Vigneron DB, Brindle K, Chekmenev EY, Comment A, Cunningham CH, DeBerardinis RJ, Green GG, Leach MO, Rajan SS, Rizi RR, Ross BD, Warren WS, Malloy CR. Analysis of cancer metabolism by imaging hyperpolarized nuclei: prospects for translation to clinical research. Neoplasia. 2011; 13:81–97. [PubMed: 21403835]
273. Hu S, Balakrishnan A, Bok RA, Anderton B, Larson PE, Nelson SJ, Kurhanewicz J, Vigneron DB, Goga A. (13)C–pyruvate imaging reveals alterations in glycolysis that precede c-Myc-induced tumor formation and regression. Cell Metab. 2011; 14:131–142. [PubMed: 21723511]
274. Wilson DM, Keshari KR, Larson PEZ, Chen AP, Hu S, Van Criekinge M, Bok R, Nelson SJ, Macdonald JM, Vigneron DB, Kurhanewicz J. Multi-compound polarization by DNP allows simultaneous assessment of multiple enzymatic activities in vivo. J Magn Reson. 2010; 205:141–147. [PubMed: 20478721]
275. Clatworthy MR, Kettunen MI, Hu DE, Mathews RJ, Witney TH, Kennedy BWC, Bohndiek SE, Gallagher FA, Jarvis LB, Smith KGC, Brindle KM. Magnetic resonance imaging with hyperpolarized 1,4-C-13(2) fumarate allows detection of early renal acute tubular necrosis. Proc Natl Acad Sci USA. 2012; 109:13374–13379. [PubMed: 22837393]

276. Witney TH, Kettunen MI, Brindle KM. Kinetic modeling of hyperpolarized C-13 label exchange between pyruvate and lactate in tumor cells. J Biol Chem. 2011; 286:24572–24580. [PubMed: 21596745]

277. Rodrigues TB, Serrao EM, Kennedy BWC, Hu DE, Kettunen MI, Brindle KM. Magnetic resonance imaging of tumor glycolysis using hyperpolarized C-13-labeled glucose. Nat Med. 2014; 20:93. [PubMed: 24317119]

278. Kennedy BWC, Kettunen MI, Hu DE, Brindle KM. Probing lactate dehydrogenase activity in tumors by measuring hydrogen/deuterium exchange in hyperpolarized L-1-C-13, U-H-2 lactate. J Am Chem Soc. 2012; 134:4969–4977. [PubMed: 22316419]

279. Gallagher FA, Kettunen MI, Day SE, Hu DE, Karlsson M, Gisselsson A, Lerche MH, Brindle KM. Detection of tumor glutamate metabolism in vivo using C-13 magnetic resonance spectroscopy and hyperpolarized 1-C-13 glutamate. Magn Reson Med. 2011; 66:18–23. [PubMed: 21695718]

280. Gallagher FA, Kettunen MI, Brindle KM. Imaging pH with hyperpolarized C-13. NMR Biomed. 2011; 24:1006–1015. [PubMed: 21812047]

281. Bohndiek SE, Kettunen MI, Hu DE, Kennedy BWC, Boren J, Gallagher FA, Brindle KM. Hyperpolarized 1-C-13-ascorbic and dehydroascorbic acid: vitamin C as a probe for imaging redox status in vivo. J Am Chem Soc. 2011; 133:11795–11801. [PubMed: 21692446]

282. Gallagher FA, Kettunen MI, Hu DE, Jensen PR, in't Zandt R, Karlsson M, Gisselsson A, Nelson SK, Witney TH, Bohndiek SE, Hansson G, Peitersen T, Lerche MH, Brindle KM. Production of hyperpolarized 1,4-C-13(2) malate from 1,4-C-13(2) fumarate is a marker of cell necrosis and treatment response in tumors. Proc Natl Acad Sci USA. 2009; 106:19801–19806. [PubMed: 19903889]

283. Gallagher FA, Kettunen MI, Day SE, Hu DE, Ardenkjaer-Larsen JH, in't Zandt R, Jensen PR, Karlsson M, Golman K, Lerche MH, Brindle KM. Magnetic resonance imaging of pH in vivo using hyperpolarized (13)C- labelled bicarbonate. Nature. 2008; 453:U940–U973.

284. Lerche MH, Jensen PR, Karlsson M, Meier S. NMR insights into the inner workings of living cells. Anal Chem. 2015; 87:119–132. [PubMed: 25084065]

285. Jensen PR, Serra SC, Miragoli L, Karlsson M, Cabella C, Poggi L, Venturi L, Tedoldi F, Lerche MH. Hyperpolarized 1,3-C-13(2) ethyl acetoacetate is a novel diagnostic metabolic marker of liver cancer. Int J Cancer. 2015; 136:E117–E126. [PubMed: 25156718]

286. Canape C, Catanzaro G, Terreno E, Karlsson M, Lerche MH, Jensen PR. Probing treatment response of glutaminolytic prostate cancer cells to natural drugs with hyperpolarized 5-C-13 glutamine. Magn Reson Med. 2015; 73:2296–2305. [PubMed: 25045880]

287. Christensen CE, Karlsson M, Winther JR, Jensen PR, Lerche MH. Non-invasive in-cell determination of free cytosolic NAD(+)/NADH ratios using hyperpolarized glucose show large variations in metabolic phenotypes. J Biol Chem. 2014; 289:2344–2352. [PubMed: 24302737]

288. Jensen PR, Peitersen T, Karlsson M, in't Zandt R, Gisselsson A, Hansson G, Meier S, Lerche MH. Tissue-specific short chain fatty acid metabolism and slow metabolic recovery after ischemia from hyperpolarized NMR in vivo. J Biol Chem. 2009; 284:36077–36082. [PubMed: 19861411]

289. Brindle KM. New approaches for imaging tumour responses to treatment. Nat Rev Cancer. 2008; 8:94–107. [PubMed: 18202697]

290. Comment A, Merritt ME. Hyperpolarized magnetic resonance as a sensitive detector of metabolic function. Biochemistry. 2014; 53:7333–7357. [PubMed: 25369537]

291. Abragam A, Goldman M. Principles of dynamic nuclear polarisation. Rep Prog Phys. 1978; 41:395–467.

292. Ardenkjaer-Larsen JH, Fridlund B, Gram A, Hansson G, Hansson L, Lerche MH, Servin R, Thaning M, Golman K. Increase in signal-to-noise ratio of >10,000 times in liquid-state NMR. Proc Natl Acad Sci USA. 2003; 100:10158–10163. [PubMed: 12930897]

293. Albe KR, Butler MH, Wright BE. Cellular concentrations of enzymes and their substrates. J Theor Biol. 1990; 143:163–195. [PubMed: 2200929]

294. Maughan DW, Henkin JA, Vigoreaux JO. Concentrations of glycolytic enzymes and other cytosolic proteins in the diffusible fraction of a vertebrate muscle proteome. Mol Cell Proteomics. 2005; 4:1541–1549. [PubMed: 15982968]
295. Madhukar NS, Warmoes MO, Locasale JW. Organization of enzyme concentration across the metabolic network in cancer cells. PLoS ONE. 2015; 10:e0117131. [PubMed: 25621879]
296. Fersht, A. Structure and Mechanism in Protein Science. W.H. Freeman & Co; New York: 1999.
297. Bhattacharya P, Chekmenev EY, Reynolds WF, Wagner S, Zacharias N, Chan HR, Bunger R, Ross BD. Parahydrogen-induced polarization (PHIP) hyperpolarized MR receptor imaging in vivo: a pilot study of C-13 imaging of atheroma in mice. NMR Biomed. 2011; 24:1023–1028. [PubMed: 21538638]
298. Cai C, Coffey AM, Shchepin RV, Chekmenev EY, Waddell KW. Efficient transformation of parahydrogen spin order into heteronuclear magnetization. J Phys Chem B. 2013; 117:1219–1224. [PubMed: 23214962]
299. Chekmenev EY, Hovener J, Norton VA, Harris K, Batchelder LS, Bhattacharya P, Ross BD, Weitekamp DP. PASADENA hyperpolarization of succinic acid for MRI and NMR spectroscopy. J Am Chem Soc. 2008; 130:4212. [PubMed: 18335934]
300. Hovener JB, Chekmenev EY, Harris KC, Perman WH, Robertson LW, Ross BD, Bhattacharya P. PASADENA hyperpolarization of C-13 biomolecules: equipment design and installation. Magn Reson Mater Phys Biol Med. 2009; 22:111–121.
301. Natterer J, Bargon J. Parahydrogen induced polarization. Prog Nucl Magn Reson Spectrosc. 1997; 31:293–315.
302. Goldman M, Johannesson H, Axelsson O, Karlsson M. Design and implementation of C-13 hyperpolarization from para-hydrogen, for new MRI contrast agents. CR Chim. 2006; 9:357–363.
303. Zacharias NM, Chan HR, Sailasuta N, Ross BD, Bhattacharya P. Real-time molecular imaging of tricarboxylic acid cycle metabolism in vivo by hyperpolarized 1-^{13}C diethyl succinate. J Am Chem Soc. 2012; 134:934– 943. [PubMed: 22146049]
304. Reineri F, Boi T, Aime S. ParaHydrogen induced polarization of C-13 carboxylate resonance in acetate and pyruvate. Nat Commun. 2015; 6
305. Reineri F, Bouguet-Bonnet S, Canet D. Creation and evolution of net proton hyperpolarization arising from para-hydrogenation. J Magn Reson. 2011; 210:107–112. [PubMed: 21402486]
306. Shchepin RV, Coffey AM, Waddell KW, Chekmenev EY. PASADENA hyperpolarized C-13 phospholactate. J Am Chem Soc. 2012; 134:3957– 3960. [PubMed: 22352377]
307. Day SE, Kettunen MI, Gallagher FA, Hu DE, Lerche M, Wolber J, Golman K, Ardenkjaer-Larsen JH, Brindle KM. Detecting tumor response to treatment using hyperpolarized C-13 magnetic resonance imaging and spectroscopy. Nat Med. 2007; 13:1382–1387. [PubMed: 17965722]
308. Warburg O. Versuche an uberlebendem Carcinomgewebe (Methoden). Biochem Zeitschr. 1923; 142:317–333.
309. Warburg O. On the origin of cancer cells. Science. 1956; 123:309–314. [PubMed: 13298683]
310. Garber K. Energy boost: the Warburg effect returns in a new theory of cancer. J Natl Cancer Inst. 2004; 96:1805–1806. [PubMed: 15601632]
311. Xie H, Hanai J, Ren J-G, Kats L, Burgess K, Bhargava P, Signoretti S, Billiard J, Duffy KJ, Grant A, Wang X, Lorkiewicz PK, Schatzman S, Bousamra M II, Lane AN, Higashi RM, Fan TW-M, Pandolfi PPP, Sukhatme VP, Seth P. Targeting lactate dehydrogenase-A (LDH-A) inhibits tumorigenesis and tumor progression in mouse models of lung cancer and impacts tumor initiating cells. Cell Metab. 2014; 19:795–809. [PubMed: 24726384]
312. Webb BA, Chimenti M, Jacobson MP, Barber DL. Dysregulated pH: a perfect storm for cancer progression. Nat Rev Cancer. 2011; 11:671–677. [PubMed: 21833026]
313. Shirmanova MV, Druzhkova IN, Lukina MM, Matlashov ME, Belousov VV, Snopova LB, Prodanetz NN, Dudenkova VV, Lukyanov SA, Zagaynova EV. Intracellular pH imaging in cancer cells in vitro and tumors in vivo using the new genetically encoded sensor SypHer2. Biochim Biophys Acta – Gen Subj. 2015; 1850:1905–1911.
314. Hakala MT, Glaid AJ, Schwert GW. Lactic dehydrogenase. II. Variation of kinetics and equilibrium constants with temperature. J Biol Chem. 1956; 221:191–210. [PubMed: 13345810]

315. Lin S, Guarente L. Nicotinamide adenine dinucleotide, a metabolic regulator of transcription, longevity and disease. Curr Opin Cell Biol. 2003; 15:241– 246. [PubMed: 12648681]

316. Veech RL, Eggleston LV, Krebs HA. The redox state of free nicotinamide-adenine dinucleotide phosphate in the cytoplasm of rat liver. Biochem J. 1969; 115(4):609–619. [PubMed: 4391039]

317. Jeon S-M, Chandel NS, Hay N. AMPK regulates NADPH homeostasis to promote tumour cell survival during energy stress. Nature. 2012; 485:661. [PubMed: 22660331]

318. Fan J, Ye JB, Kamphorst JJ, Shlomi T, Thompson CB, Rabinowitz JD. Quantitative flux analysis reveals folate-dependent NADPH production. Nature. 2014; 510:298. [PubMed: 24805240]

319. Dzierlenga MW, Antoniou D, Schwartz SD. Another look at the mechanisms of hydride transfer enzymes with quantum and classical transition path sampling. J Phys Chem Lett. 2015; 6:117–1181.

320. Berti PJ, Tanaka KSE. Transition state analysis using multiple kinetic isotope effects: mechanisms of enzymatic and non-enzymatic glycoside hydrolysis and transfer. Adv Phys Org Chem. 2002; 37:239–314.

321. Poulo, JM.; Elston, T.; Lane, AN.; Macdonald, JM.; Cascante, M. Introduction to metabolic control analysis (MCA). In: Fan, TW-M.; Higashi, RM.; Lane, AN., editors. Handbook of Metabolomics. Humana Press; 2012.

322. Rose IA. The use of kinetic isotope effects in the study of metabolic control. J Biol Chem. 1961; 236:603–609. [PubMed: 13743275]

323. Meier S, Jensen PR, Duus JO. Real-time detection of central carbon metabolism in living *Escherichia coli* and its response to perturbations. FEBS Lett. 2012; 585:3133–3138. [PubMed: 21907715]

324. Hu S, Yoshihara HAI, Bok R, Zhou J, Zhu MH, Kurhanewicz J, Vigneron DB. Use of hyperpolarized 1-C-13 pyruvate and 2-C-13 pyruvate to probe the effects of the anticancer agent dichloroacetate on mitochondrial metabolism in vivo in the normal rat. Magn Reson Imaging. 2012; 30:1367– 1372. [PubMed: 22819176]

325. Harzstark AL, Weinberg VK, Grycz K, Hurd RE, Ardenkjaer-Larsen JH, Murray J, Chen A, Ferrone M, Park I, Reed G, Munster PN, Small EJ, Carvajal LE, VanCriekinge ME, Larson PE, Chang J, Bok RA, Nelson SJ, Vigneron DB, Kurhanewicz JV. A first-in-human phase I imaging study using hyperpolarized (1)C-13 pyruvate (h-Py) in patients (pts) with localized prostate cancer (I-PCa). J Clin Oncol. 2012; 30

326. Chen AP, Hurd RE, Schroeder MA, Lau AZ, Gu YP, Lam WW, Barry J, Tropp J, Cunningham CH. Simultaneous investigation of cardiac pyruvate dehydrogenase flux, Krebs cycle metabolism and pH, using hyperpolarized 1,2-C-13(2) pyruvate in vivo. NMR Biomed. 2012; 25:305–311. [PubMed: 21774012]

327. Seth P, Grant A, Tang J, Vinogradov E, Wang X, Lenkinski R, Sukhatme VP. On-target inhibition of tumor fermentative glycolysis as visualized by hyperpolarized pyruvate. Neoplasia. 2011; 13:60–71. [PubMed: 21245941]

328. Hu S, Balakrishnan A, Bok RA, Anderton B, Larson PEZ, Nelson SJ, Kurhanewicz J, Vigneron DB, Goga A. (13)C–pyruvate imaging reveals alterations in glycolysis that precede c-Myc-induced tumor formation and regression. Cell Metab. 2011; 14:131–142. [PubMed: 21723511]

329. Bastiaansen JAM, Yoshihara HAI, Takado Y, Gruetter R, Comment A. Hyperpolarized C-13 lactate as a substrate for in vivo metabolic studies in skeletal muscle. Metabolomics. 2014; 10:986–994.

330. Schroeder MA, Atherton HJ, Ball DR, Cole MA, Heather LC, Griffin JL, Clarke K, Radda GK, Tyler DJ. Real-time assessment of Krebs cycle metabolism using hyperpolarized C-13 magnetic resonance spectroscopy. Faseb J. 2009; 23:2529–2538. [PubMed: 19329759]

331. Schroeder MA, Atherton HJ, Heather LC, Griffin JL, Clarke K, Radda GK, Tyler DJ. Determining the in vivo regulation of cardiac pyruvate dehydrogenase based on label flux from hyperpolarised 1-C-13 pyruvate. NMR Biomed. 2011; 24:980–987. [PubMed: 21387444]

332. Jitrapakdee S, St Maurice M, Rayment I, Cleland WW, Wallace JC, Attwood PV. Structure, mechanism and regulation of pyruvate carboxylase. Biochem J. 2008; 413:369–387. [PubMed: 18613815]

333. Dzien P, Kettunen MI, Marco-Rius I, Serrao EM, Rodrigues TB, Larkin TJ, Timm KN, Brindle KM. C-13 magnetic resonance spectroscopic imaging of hyperpolarized 1-C-13, U-H-2(5) ethanol oxidation can be used to assess aldehyde dehydrogenase activity in vivo. Magn Reson Med. 2015; 73:1733– 1740. [PubMed: 24800934]
334. Keshari KR, Wilson DM. Chemistry and biochemistry of ^{13}C hyperpolarized magnetic resonance using dynamic nuclear polarization. Chem Soc Rev. 2014; 43:1627–1659. [PubMed: 24363044]
335. Meier S, Jensen PR, Karlsson M, Lerche MH. Hyperpolarized NMR probes for biological assays. Sensors. 2014; 14:1576–1597. [PubMed: 24441771]
336. Harris T, Degani H, Frydman L. Hyperpolarized C-13 NMR studies of glucose metabolism in living breast cancer cell cultures. NMR Biomed. 2013; 26:1831–1843. [PubMed: 24115045]
337. Moreno KX, Satapati S, DeBerardinis RJ, Burgess SC, Malloy CR, Merritt ME. Real-time detection of hepatic gluconeogenic and glycogenolytic states using hyperpolarized 2-C-13 dihydroxyacetone. J Biol Chem. 2014; 289:35859–35867. [PubMed: 25352600]
338. Timm KN, Hartl J, Keller MA, Hu D-E, Kettunen MI, Rodrigues TB, Ralser M, Brindle KM. Hyperpolarized [U-^{2}H, U-^{13}C]glucose reports on glycolytic and pentose phosphate pathway activity in EL4 tumors and glycolytic activity in yeast cells. Magn Reson Med. 2014
339. Gallagher FA, Kettunen MI, Day SE, Lerche M, Brindle KM. C-13 MR spectroscopy measurements of glutaminase activity in human hepatocellular carcinoma cells using hyperpolarized C-13-labeled glutamine. Magn Reson Med. 2008; 60:253–257. [PubMed: 18666104]
340. Ochoa-Ruiz E, Diaz-Ruiz R. Anaplerosis in cancer: another step beyond the warburg effect. Am J Mol Biol. 2012; 2:291–303.
341. Mazurek S, Eigenbrodt E. The tumor metabolome. Anticancer Res. 2003; 23:1149–1154. [PubMed: 12820363]
342. Karlsson M, Jensen PR, in 't Zandt R, Gisselsson A, Hansson G, Duus JO, Meier S, Lerche MH. Imaging of branched chain amino acid metabolism in tumors with hyperpolarized ^{13}C ketoisocaproate. Int J Cancer. 2010; 127:729–736. [PubMed: 19960440]
343. von Morze C, Bok RA, Reed GD, Ardenkjaer-Larsen JH, Kurhanewicz J, Vigneron DB. Simultaneous multiagent hyperpolarized (13)C perfusion imaging. Magn Reson Med. 2014; 72:1599–1609. [PubMed: 24382698]
344. Schroeder MA, Atherton HJ, Dodd MS, Lee P, Cochlin LE, Radda GK, Clarke K, Tyler DJ. The cycling of acetyl-coenzyme A through acetylcarnitine buffers cardiac substrate supply: a hyperpolarized ^{13}C magnetic resonance study. Circ Cardiovasc Imaging. 2012; 5:201–209. [PubMed: 22238215]
345. Rider OJ, Tyler DJ. Clinical implications of cardiac hyperpolarized magnetic resonance imaging. J Cardiovasc Magn Reson. 2013; 15:93. [PubMed: 24103786]
346. Lane AN, Fan TW, Higashi RM. Isotopomer-based metabolomic analysis by NMR and mass spectrometry. Methods Cell Biol. 2008; 84:541–588. [PubMed: 17964943]
347. Schmidt K, Carlsen M, Nielsen J, Villadsen J. Modeling isotopomer distributions in biochemical networks using isotopomer mapping matrices. Biotechnol Bioeng. 1997; 55:831–840. [PubMed: 18636594]
348. Wittmann C, Heinzle E. Modeling and experimental design for metabolic flux analysis of lysine-producing Corynebacteria by mass spectrometry. Metab Eng. 2001; 3:173–191. [PubMed: 11289793]
349. Zupke C, Stephanopoulos G. Modeling of isotope distributions and intracellular fluxes in metabolic networks using atom mapping matrices. Biotechnol Prog. 1994; 10:489–498.
350. Yuan J, Bennett BD, Rabinowitz JD. Kinetic flux profiling for quantitation of cellular metabolic fluxes. Nat Protoc. 2008; 3:1328–1340. [PubMed: 18714301]
351. Selivanov V, Vizan P, Mollinedo F, Fan T, Lee P, Cascante M. Edelfosine-induced metabolic changes in cancer cells that precede the overproduction of reactive oxygen species and apoptosis. BMC Syst Biol. 2010; 4:135. [PubMed: 20925932]
352. Mason GF, Rothman DL. Basic principles of metabolic modeling of NMR (13)C isotopic turnover to determine rates of brain metabolism in vivo. Metab Eng. 2004; 6:75–84. [PubMed: 14734257]

353. Noack S, Noh K, Moch M, Oldiges M, Wiechert W. Stationary versus non-stationary (13)C-MFA: a comparison using a consistent dataset. J Biotechnol. 2011; 154:179–190. [PubMed: 20638432]
354. Zamboni N. ^{13}C metabolic flux analysis in complex systems. Curr Opin Biotechnol. 2011; 22:103–108. [PubMed: 20833526]
355. Jamshidi N, Edwards JS, Fahland T, Church GM, Palsson BO. Dynamic simulation of the human red blood cell metabolic network. Bioinformatics. 2001; 17:286–287. [PubMed: 11294796]
356. Niedenfuhr S, Wiechert W, Noh K. How to measure metabolic fluxes: a taxonomic guide for ^{13}C fluxomics. Curr Opin Biotechnol. 2015; 34:82–90. [PubMed: 25531408]
357. Schryer DW, Peterson P, Paalme T, Vendelin M. Bidirectionality and compartmentation of metabolic fluxes are revealed in the dynamics of isotopomer networks. Int J Mol Sci. 2009; 10:1697–1718. [PubMed: 19468334]
358. Maher AD, Kuchel PW, Ortega F, de Atauri P, Centelles J, Cascante M. Mathematical modelling of the urea cycle – a numerical investigation into substrate channelling. Eur J Biochem. 2003; 270:3953–3961. [PubMed: 14511377]
359. Luo Z, Saha AK, Xiang X, Ruderman NB. AMPK, the metabolic syndrome and cancer. Trends Pharmacol Sci. 2005; 26:69–76. [PubMed: 15681023]
360. Ardenkjaer-Larsen JH, Boebinger GS, Comment A, Duckett S, Edison AS, Engelke F, Griesinger C, Griffin RG, Hilty C, Maeda H, Parigi G, Prisner T, Ravera E, van Bentum J, Vega S, Webb A, Luchinat C, Schwalbe H, Frydman L. Facing and overcoming sensitivity challenges in biomolecular NMR spectroscopy. Angew Chem – Int Ed. 2015; 54:9162–9185.
361. Bhattacharya A. Chemistry: breaking the billion-hertz barrier. Nature. 2010; 463:605–606. [PubMed: 20130626]
362. Bascunan J, Hahn S, Park DK, Iwasa Y. A 1.3-GHz LTS/HTS NMR magnet– a progress report. IEEE Trans Appl Supercond. 2011; 21:2092–2095. [PubMed: 22081752]
363. Brey WW, Edison AS, Nast RE, Rocca JR, Saha S, Withers RS. Design, construction, and validation of a 1-mm triple-resonance high-temperature-superconducting probe for NMR. J Magn Reson. 2006; 179:290–293. [PubMed: 16423543]
364. Takeda M, Hallenga K, Shigezane M, Waelchli M, Loehr F, Markley JL, Kainosho M. Construction and performance of an NMR tube with a sample cavity formed within magnetic susceptibility-matched glass. J Magn Reson. 2011; 209:167–173. [PubMed: 21316281]
365. Mobli M, Maciejewski MW, Gryk MR, Hoch JC. Automatic maximum entropy spectral reconstruction in NMR. J Biomol NMR. 2007; 39:133–139. [PubMed: 17701276]
366. Kupče Ē, Freeman R. Fast multi-dimensional Hadamard spectroscopy. J Magn Reson. 2003; 163:56–63. [PubMed: 12852907]
367. Freeman R, Kupče Ē. New ways to record multidimensional NMR spectra. Curr Anal Chem. 2006; 2:101–105.
368. Kupče Ē. NMR with multiple receivers. Top Curr Chem. 2013; 335:71–96. [PubMed: 21837554]
369. Pudakalakatti SM, Dubey A, Jaipuria G, Shubhashree U, Adiga SK, Moskau D, Atreya HS. A fast NMR method for resonance assignments: application to metabolomics. J Biomol NMR. 2014; 58:165–173. [PubMed: 24488481]
370. Shapira B, Shetty K, Brey WW, Gan Z, Frydman L. Single-scan 2D NMR spectroscopy on a 25 T bitter magnet. Chem Phys Lett. 2007; 442:478–482. [PubMed: 18037970]
371. Giraudeau P, Frydman L. Ultrafast 2D NMR: an emerging tool in analytical spectroscopy. Annu Rev Anal Chem. 2014; 7:129–161.
372. Giraudeau P, Baguet E. Improvement of the inverse-gated-decoupling sequence for a faster quantitative analysis of various samples by C-13 NMR spectroscopy. J Magn Reson. 2006; 180:110–117. [PubMed: 16488168]
373. Rouger L, Charrier B, Pathan M, Akoka S, Giraudeau P. Processing strategies to obtain clean interleaved ultrafast 2D NMR spectra. J Magn Reson. 2014; 238:87–93. [PubMed: 24322368]
374. Le Guennec A, Giraudeau P, Caldarelli S. Evaluation of fast 2D NMR for metabolomics. Anal Chem. 2014; 86:5946–5954. [PubMed: 24856256]

375. Foroozandeh M, Giraudeau P, Jeannerat D. A toolbox of HSQC experiments for small molecules at high C-13-enrichment. Artifact-free, fully C-13-homodecoupled and J(CC)-encoding pulse sequences. Magn Reson Chem. 2013; 51:808–814. [PubMed: 24123384]

376. Boisseau R, Charrier B, Massou S, Portais J-C, Akoka S, Giraudeau P. Fast spatially encoded 3D NMR strategies for C-13-based metabolic flux analysis. Anal Chem. 2013; 85:9751–9757. [PubMed: 24006900]

377. Akoka, S.; Giraudeau, P. Fast hybrid multi-dimensional NMR methods based on ultrafast 2D NMR. Magn Reson Chem. 2015. http://dx.doi.org/10.1002/mrc.4237

378. Schanda P, Kupče Ē, Brutscher B. SOFAST-HMQC experiments for recording two-dimensional heteronuclear correlation spectra of proteins within a few seconds. J Biomol NMR. 2005; 33:199–211. [PubMed: 16341750]

379. Kupče Ē, Freeman R. Fast multidimensional NMR by polarization sharing. Magn Reson Chem. 2007; 45:2–4. [PubMed: 17125135]

380. Theillet FX, Binolfi A, Liokatis S, Verzini S, Selenko P. Paramagnetic relaxation enhancement to improve sensitivity of fast NMR methods: application to intrinsically disordered proteins. J Biomol NMR. 2011; 51:487–495. [PubMed: 22008951]

381. Michaelis VK, Smith AA, Corzilius B, Haze O, Swager TM, Griffin RG. High-field ^{13}C dynamic nuclear polarization with a radical mixture. J Am Chem Soc. 2013; 135:2935–2938. [PubMed: 23373472]

382. Reed GD, Larson PEZ, von Morze C, Bok R, Lustig M, Kerr AB, Pauly JM, Kurhanewicz J, Vigneron DB. A method for simultaneous echo planar imaging of hyperpolarized C-13 pyruvate and C-13 lactate. J Magn Reson. 2012; 217:41–47. [PubMed: 22405760]

383. Nelson SJ, Kurhanewicz J, Vigneron DB, Larson PEZ, Harzstark AL, Ferrone M, van Criekinge M, Chang JW, Bok R, Park I, Reed G, Carvajal L, Small EJ, Munster P, Weinberg VK, Ardenkjaer-Larsen JH, Chen AP, Hurd RE, Odegardstuen L-I, Robb FJ, Tropp J, Murray JA. Metabolic imaging of patients with prostate cancer using hyperpolarized 1-C-13 pyruvate. Sci Transl Med. 2013; 5

384. Fan, TW. Considerations of sample preparation for metabolomics investigation. In: Fan, TW.; Lane, AN.; Hiagshi, RM., editors. Handbook of Metabolomics. Humana; Totoya: 2012.

385. Wollenberger A, Ristau O, Schoffa G. A simple technique for extremely rapid freezing of large pieces of tissue. Pfiugers Arch Ges Physiol. 1960; 270:399– 412.

386. Fan TWM, Higashi RM, Lane AN. Integrating metabolomics and transcriptomics for probing Se anticancer mechanisms. Drug Metab Rev. 2006; 38:707–732. [PubMed: 17145697]

Highlights

- Here we review recent developments in NMR applications to metabolic studies using stable isotope tracers.
- Recent developments in sample handling, structure determination and quantification are described.
- The unique strengths of NMR in isotopomer analysis and *in vivo* investigations are highlighted.
- New hardware and techniques are illustrated with a wide range of applications in biological research.
- We also place NMR investigations of metabolic networks in the context of integration with other ‘omics technologies.

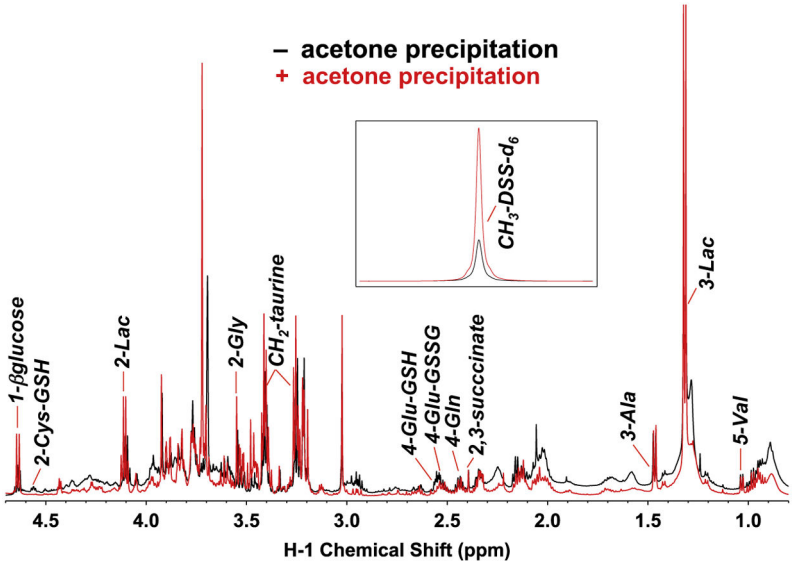

Fig. 1.

Influence of extraction procedure on NMR spectral quality of tissue extracts. Patient-derived tumor tissues were implanted into Nod/SCID Gamma mice and let grow to ca. 1 cm in diameter before harvest and pulverization in liquid N_2 for metabolite extraction using our CH_3CN:H_2O:$CHCl_3$ (2:1.5:1 v/v) solvent partitioning method [384]. The resulting polar extract was dissolved in 50% D_2O for 1D ^1H NMR measurement at 14.1 T (black line), followed by 80% acetone treatment to remove residual proteins and analysis again by ^1H NMR (red line). The two ^1H spectra were normalized by the peak area of the H3 resonance of lactate (3-Lac). The spectral region from 0.8 to 4.7 ppm is shown, along with the CH_3 resonance of the DSS-d_6 standard in the inset. The latter was much lower in intensity and broader in linewidth without acetone than with acetone precipitation of proteins, which indicates the influence of DSS binding to residual proteins on resonance quality. In contrast, the signal intensities of most metabolites were enhanced by acetone precipitation (e.g. H1-βglucose, H2-Gly), which is again consistent with signal attenuation by protein binding. In contrast, the reduced glutathione (GSH) resonances (i.e. H2-Cys and H4-Glu resonances of GSH) were absent from the spectrum after acetone treatment, which could be attributed to insolubility of GSH in 80% acetone. Re-extraction of the protein pellet with 60% acetonitrile restored the GSH signals.

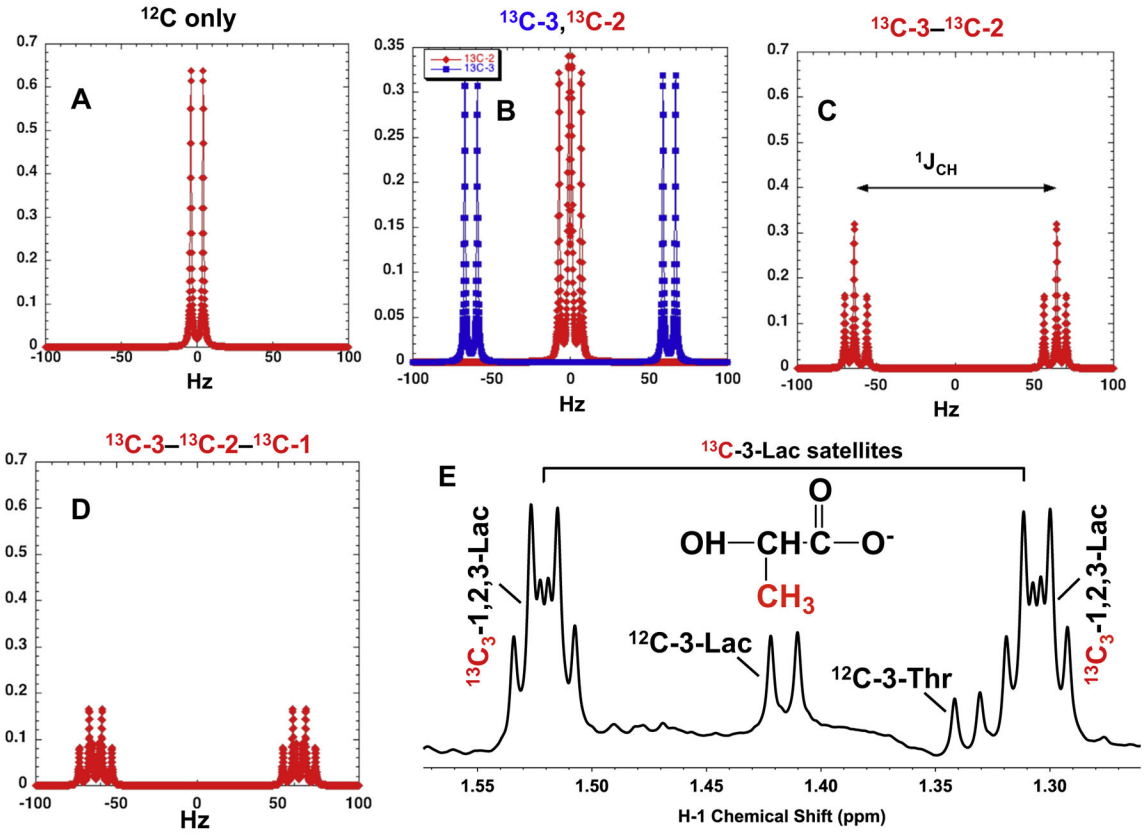

Fig. 2.

^{13}C-lactate satellite patterns in ^{1}H NMR. Panels (A–D) display the simulated splitting patterns of the ^{1}H-3 resonance of lactate with these methyl protons coupled to ^{12}C-3 (A), to ^{13}C-3 or ^{13}C-2 (B), to $^{13}C_2$-2,3 (C), and $^{13}C_3$-1,2,3 (D). An example ^{1}H spectrum of cell culture medium after 24 h of lung adenocarcinoma A549 cell growth in U-$^{13}C_6$-glucose is shown in (E), where the complex splitting pattern of ^{13}C satellites of H-3 present in U-$^{13}C_3$-lactate is evident.

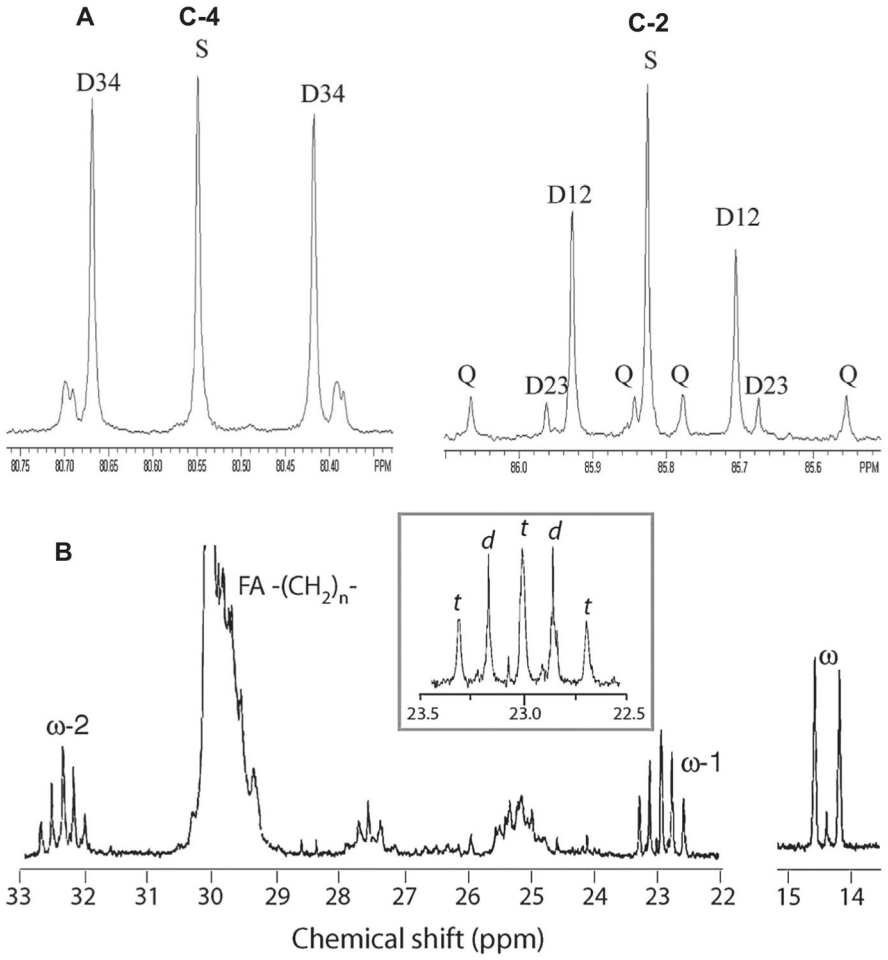

Fig. 3.

^{13}C coupling patterns of ^{13}C-enriched metabolites in ^{13}C NMR. (A) ^{13}C NMR spectrum of monoacetone glucose derived from plasma glucose of rat with infusion of $^{13}C_2$-3,4-glucose and IP injection of [U-^{13}C]proprionate and $^{2}H_2O$; S: singlet; D34, D12 or D23: doublet from C-3 and C-4, C-1 and C-2 or C-2 and C-3 coupling, respectively; Q: doublet of doublet from C-2 coupling to both C-1 and C-3 [140]. Reprinted from Anal Biochem, 327, E.S. Jin, J.G. Jones, M. Merritt, S.C. Burgess, C.R. Malloy, A.D. Sherry. Glucose production, gluconeogenesis, and hepatic tricarboxylic acid cycle fluxes measured by nuclear magnetic resonance analysis of a single glucose derivative, pp. 149–155, (2004), with permission from Elsevier. (B) ^{13}C NMR spectrum of lipids extracted from glioblastoma cultured in [U-$^{13}C_6$]glucose. The inset shows the expansion of the 23 ppm region. ω, ω-1, and ω-2: terminal CH_3, penultimate CH_2, and CH_2 neighbor to ω-1 CH_2; d: doublet; t: triplet; FA-(CH_2)n-: internal CH_2 of fatty acyl chains. Excerpted with permission from R.J. DeBerardinis, A. Mancuso, E. Daikhin, I. Nissim, M. Yudkoff, S. Wehrli, C.B. Thompson, Beyond aerobic glycolysis: transformed cells can engage in glutamine metabolism that exceeds the requirement for protein and nucleotide synthesis, Proc Natl Acad Sci USA, 104 (2007) 19345–19350 [129]. Copyright (2007) National Academy of Sciences, U.S.A.

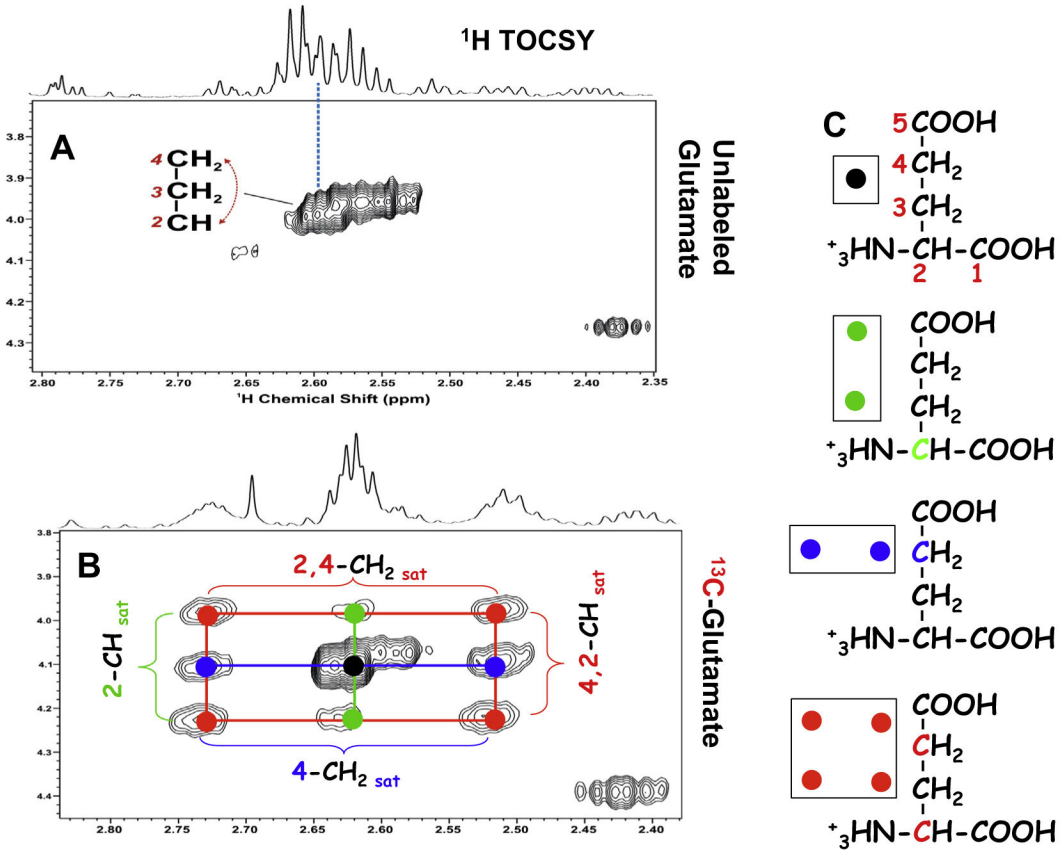

Fig. 4.

2D ^{1}H TOCSY detects four different isotopomers of glutamate. A549 cells were grown in unenriched or $^{13}C_6$-glucose for 24 h before extraction for polar metabolites. 2D ^{1}H TOCSY analysis of unenriched extracts identifies covalent connectivity of Glu-2H to Glu-4H as a cross-peak (A). The corresponding analysis of the ^{13}C enriched extract detects 3 pairs of satellite (sat) cross-peaks that are equidistant from the central cross-peak (●) of Glu-2H to Glu-4H (B). ●, ●, ●: satellite cross-peaks of Glu-4H, Glu-2H, and Glu-2,4H, respectively. The four positional isotopomers of Glu that give rise to these cross-peak patterns are shown in (C).

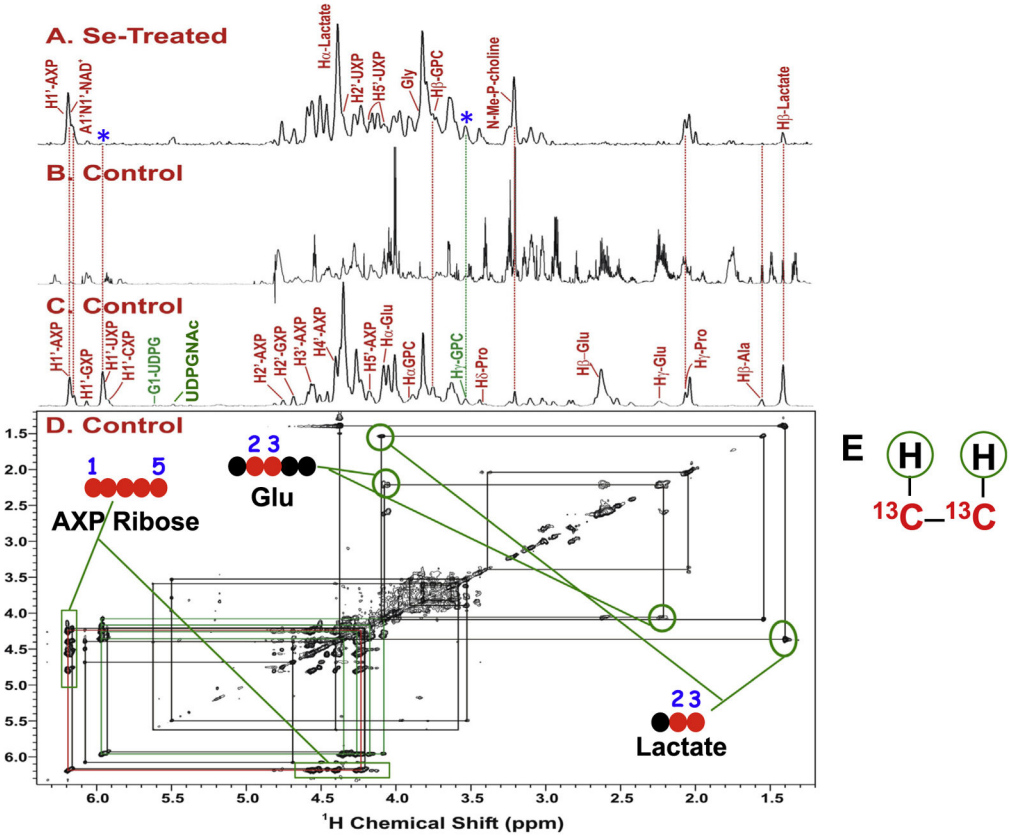

Fig. 5.

2-D ^{1}H–^{13}C HCCH–TOCSY analysis detects positional isotopomers with consecutive ^{13}C labels. Lung adenocarcinoma A549 cells were grown in $^{13}C_6$-glucose under control or selenite (Se) treatment. HCCH–TOCSY analysis was performed on the polar cell extracts to enable selective detection of protons attached to consecutively bonded ^{13}C atoms, as illustrated in (E). The 2D spectrum in (D) reveals Glu and lactate isotopomers consecutively ^{13}C labeled at C-2 and C-3 positions, as well as adenine nucleotide (AXP) isotopomer consecutively ^{13}C labeled at C-1 to C-5 of the ribose unit. Also shown are the 1D high-resolution ^{1}H NMR spectrum of the control cell extract (B) as well as the 2D projection spectra of the control (C) and selenite-treated (A) cell extracts. The ^{13}C editing also enhances the detection of minor ^{13}C labeled components such as glycerophosphocholine (GPC) and unresolved ^{13}C labeled components such as uracil nucleotides (UXP) (denoted by *) (cf. B and C). Such a capability is unique in revealing the decreased synthesis of $^{13}C_5$-1,2,3,4,5-ribose containing UXP and increased production of $^{13}C_3$-1,2,3-glycerol containing GPC by the selenite treatment (cf. A and C) (adapted from [108]).

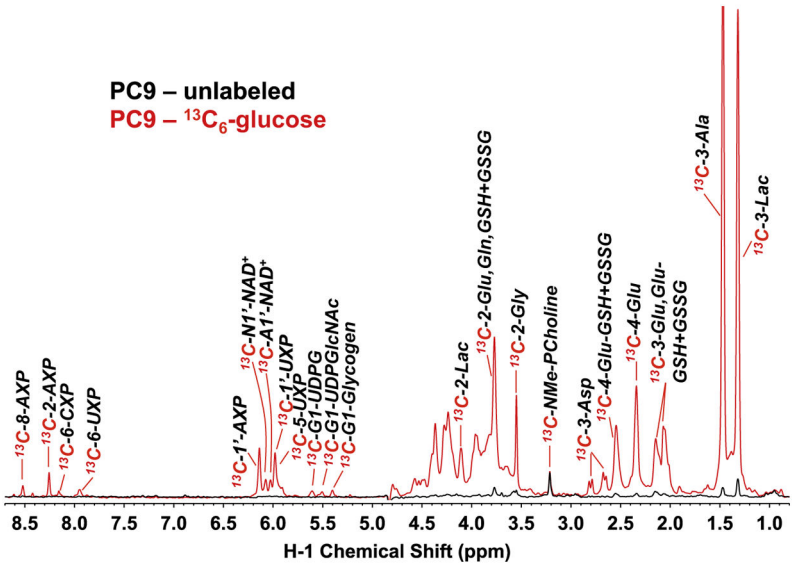

Fig. 6.

1D ^{1}H{^{13}C}-HSQC analysis provides an overview of ^{13}C positional isotopomers of metabolites in a ^{13}C labeled PC9 cell extract. Lung adenocarcinoma PC9 cells were grown in $^{13}C_6$-glucose or unlabeled glucose for 24 h before extraction. The two polar extracts were subjected to 1D ^{1}H{^{13}C}-HSQC analysis for ^{13}C positional isotopomers of various metabolites. Lac: lactate; GSH, GSSH: reduced and oxidized glutathiones; PCholine: phosphocholine; Me: methyl; UXP, CXP, AXP: uracil, cytosine, and adenine nucleotides, respectively; UDPGlcNAc: UDP-N-acetylglucosamine; UDPG: UDP-glucose.

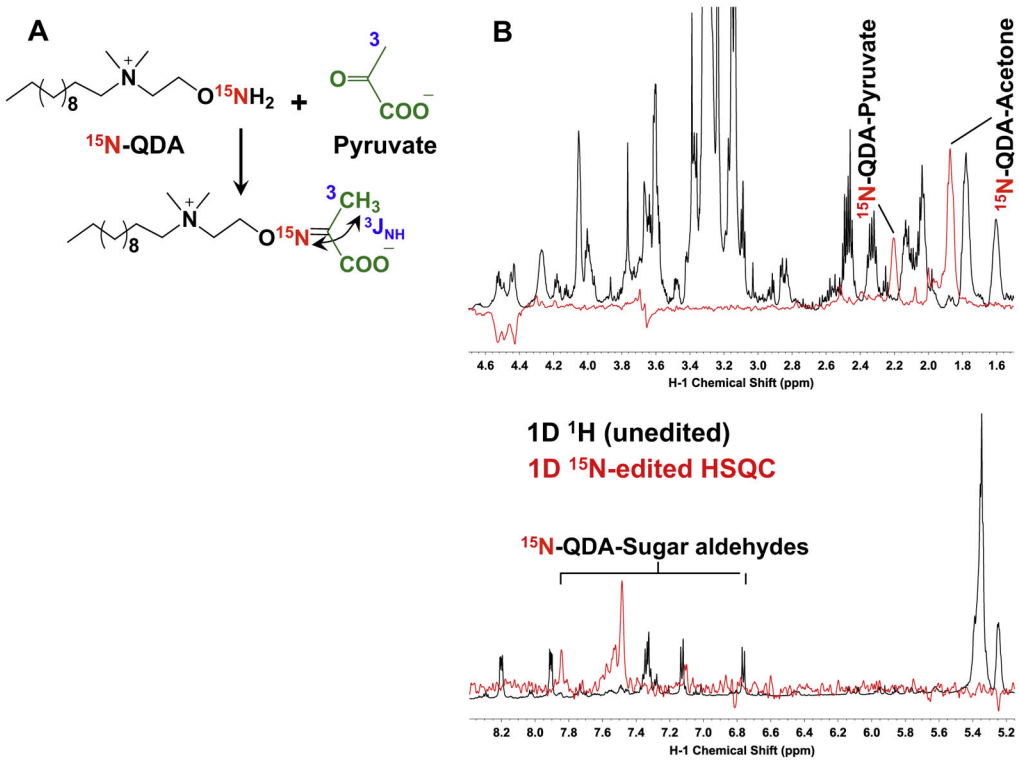

Fig. 7.

1D $^{1}H\{^{15}N\}$-HSQC analysis provides sensitive detection of ^{15}N-enriched metabolite derivatives. A549 cell extract was derivatized with an ^{15}N-enriched aminooxy probe ^{15}N-QDA (N-(2-^{15}N-aminooxyethyl)-N,N-dimethyl-1-dodecylammonium), which form oxime adducts with carbonyl-containing metabolites such as acetone, pyruvate, and sugar aldehydes (A). The 2 or 3-bond coupling between ^{15}N of the probe and ^{1}H of the metabolites enables detection of ^{15}N via its covalently linked ^{1}H by $^{1}H\{^{15}N\}$-HSQC analysis (B).

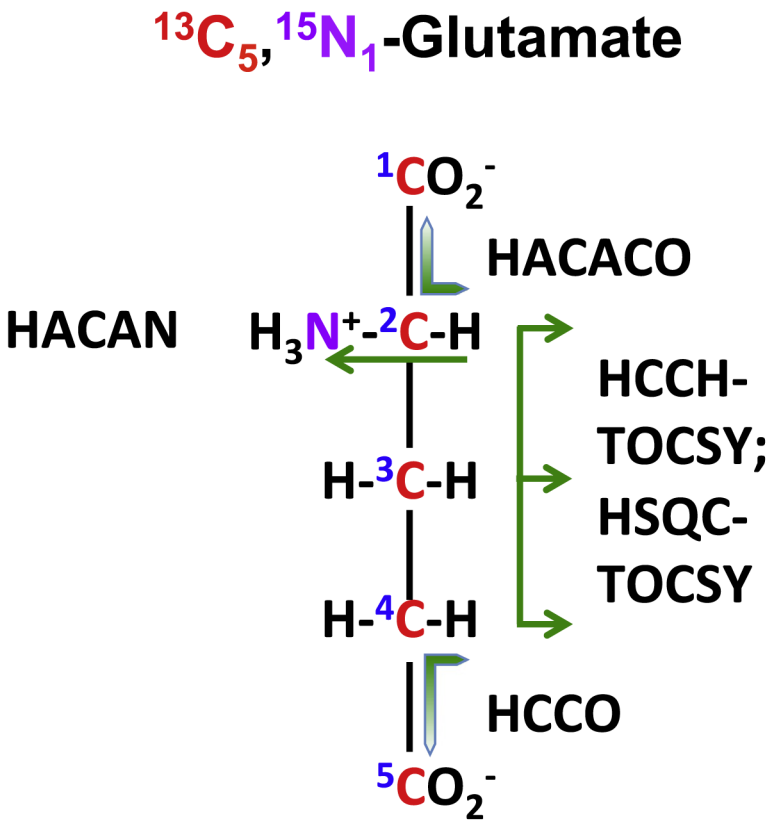

Fig. 8.

Spin topology pathways for $^{13}C_5$,$^{15}N_1$-glutamate in 2 or 3D NMR experiments. Various 3D NMR experiments that can be performed as the 2D version for ^{13}C and ^{15}N labeled Glu are depicted. Arrows denote magnetization transfer pathways in $^{13}C_5$,$^{15}N_1$-Glu via homonuclear and heteronuclear scalar couplings. C: ^{13}C; N: ^{15}N.

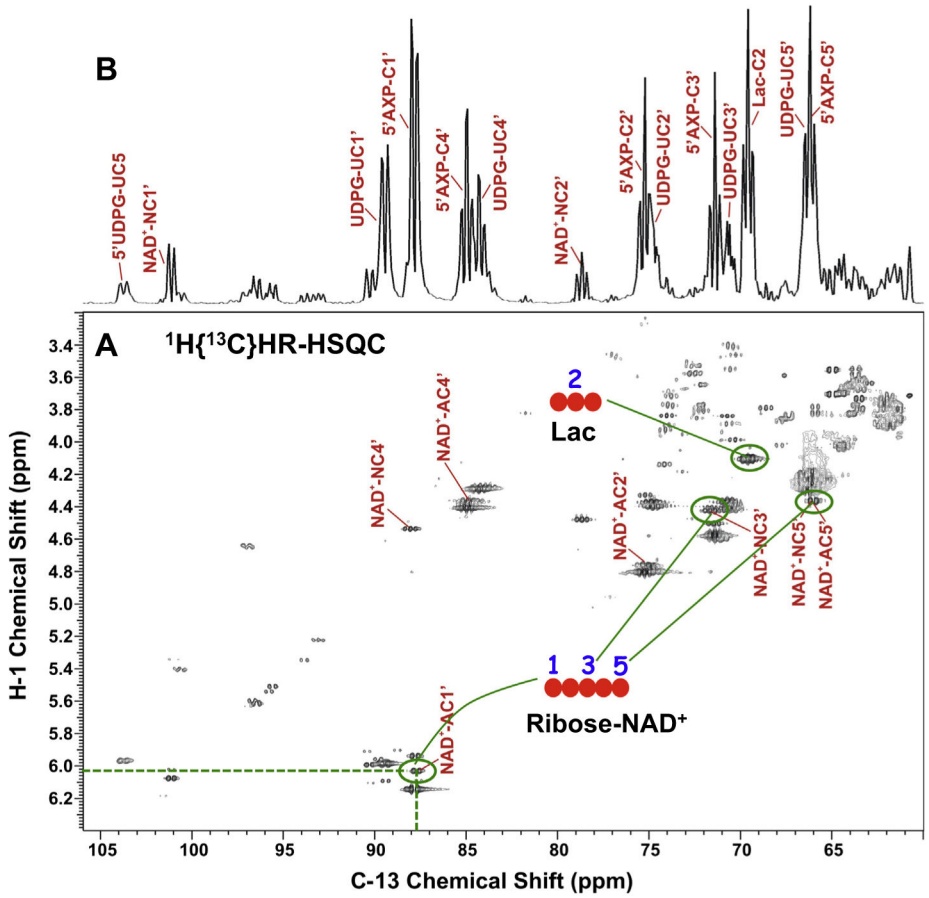

Fig. 9.

2D $^{1}H\{^{13}C\}$HR-HSQC analysis provides rigorous identification of ^{13}C positional isotopomers of metabolites via ^{13}C–^{13}C coupling patterns. A polar extract of A549 cells grown in $^{13}C_6$-glucose was analyzed by high-resolution (hr) $^{1}H\{^{13}C\}$-HSQC at 18.8 T. The 2D HSQC contour plot (A) is shown along with the 1D projection spectrum in the ^{13}C dimension (B), where the ^{13}C–^{13}C coupling patterns are better visualized. The doublet of C-1′, triplet of C-2′, and doublet of C-5′ of ribose attached to the adenine ring (A) of NAD^+ indicate the presence of $^{13}C_5$-1,2,3,4,5-ribose-containing NAD^+ isotopomer, while the triplet of C-2-lactate (Lac) identifies the presence of $^{13}C_3$-1,2,3-lactate.

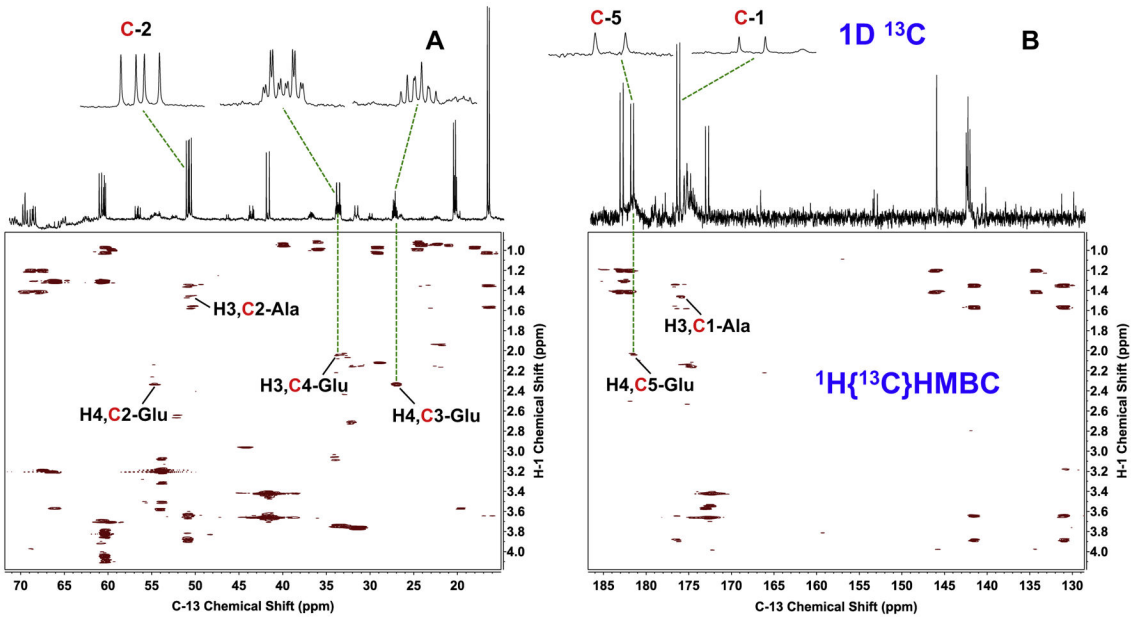

Fig. 10.

$^{1}H\{^{13}C\}$HMBC detects multiple bond $^{1}H–^{13}C$ connectivity including that between carbons with no directly attached proton(s) or carbons bonded to heteroatoms in the covalent network of given metabolites. The 2D HMBC contour plots of aliphatic (A) and carbonyl/double bonded carbon regions (B) are shown along with the corresponding 1D high-resolution ^{13}C NMR spectral regions of a polar extract obtained from lung adenocarcinoma PC9 cells grown in $^{13}C_6$-glucose for 24 h. The cross-peak for C-5 (C=O) to H-4 of Glu is evident, along with those for C-4 to H-3, as well as C-2 and C-3 to H-4. Also evident are the cross-peaks for C-1 (C=O) to H-3 and C-2 to H-3 of Ala. The expanded 1D ^{13}C spectra for C-2, C-3, C-4, and C-5 of Glu as well as C-1 and C-2 of Ala illustrate more clearly the $^{13}C–^{13}C$ coupling patterns. C: ^{13}C.

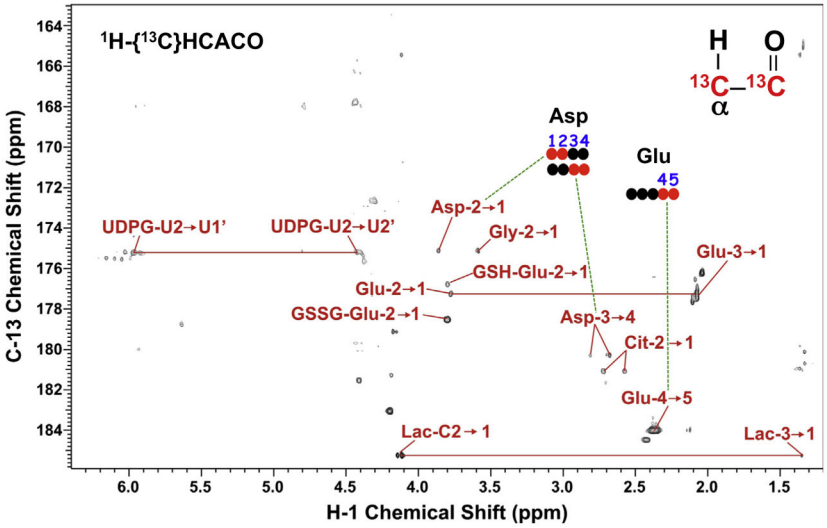

Fig. 11.

2D $^{1}H\{^{13}C\}$HCACO analysis provides rigorous identification of ^{13}C positional isotopomers of carbonyl-containing metabolites in the polar extract of A549 cells. This 2D experiment detects covalent connectivity as cross-peaks from ^{13}C-carbonyl carbon to aliphatic protons of metabolites via ^{13}C–^{13}C coupling, as illustrated in the example structure diagram (top right). The cross-peaks of ^{13}C-1 to H-3 and ^{13}C-1 to H-2 of lactate (Lac) denote the presence of $^{13}C_3$-1,2,3-lactate, those of ^{13}C-1 to H-2 and ^{13}C-4 to H-3 of Asp indicate the presence of $^{13}C_2$-1,2- and $^{13}C_2$-3,4-Asp, respectively, and those of ^{13}C-1 to H-2, ^{13}C-1 to H-3, and ^{13}C-5 to H-4 of Glu are consistent with the presence of $^{13}C_2$-1,2-, $^{13}C_3$-1,2,3-, and $^{13}C_2$-4,5-Glu, respectively.

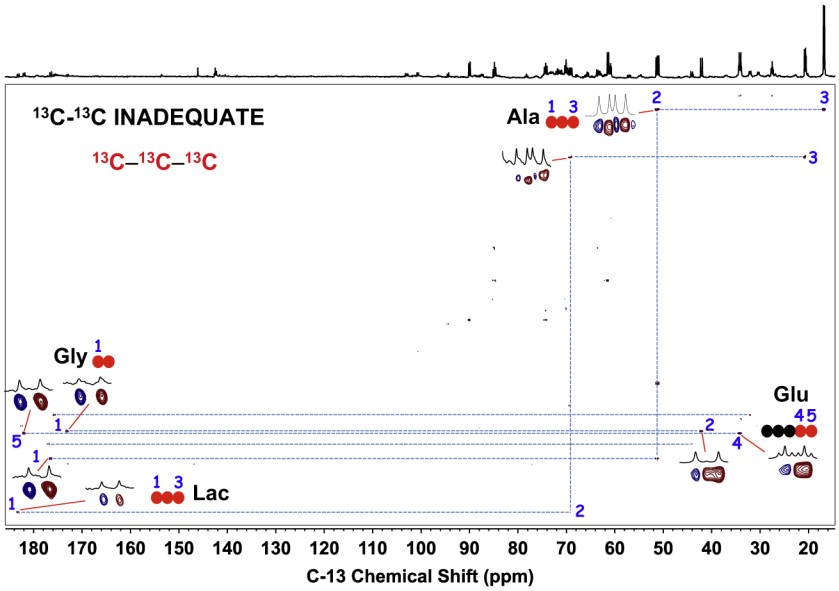

Fig. 12.

2D ^{13}C–^{13}C INADEQUATE analysis provides rigorous identification of ^{13}C positional isotopomers of ^{13}C-enriched metabolites in the polar extract of PC9 cells grown in $^{13}C_6$-glucose. This 2D experiment detects carbon covalent connectivity as cross-peaks via ^{13}C–^{13}C coupling, as illustrated in the example structure diagram (top left). The cross-peaks of ^{13}C-1 to ^{13}C-2 to ^{13}C-3 of Ala and lactate (Lac), ^{13}C-1 to ^{13}C-2 of Gly, and ^{13}C-4 to ^{13}C-5 of Glu as well as their splitting patterns unambiguously indicate the presence of $^{13}C_3$-1,2,3-Ala and -lactate, $^{13}C_2$-4,5-Glu, and $^{13}C_2$-1,2-Gly, respectively. Shown above the 2D contour plots are the corresponding 1D high-resolution ^{13}C NMR spectral regions.

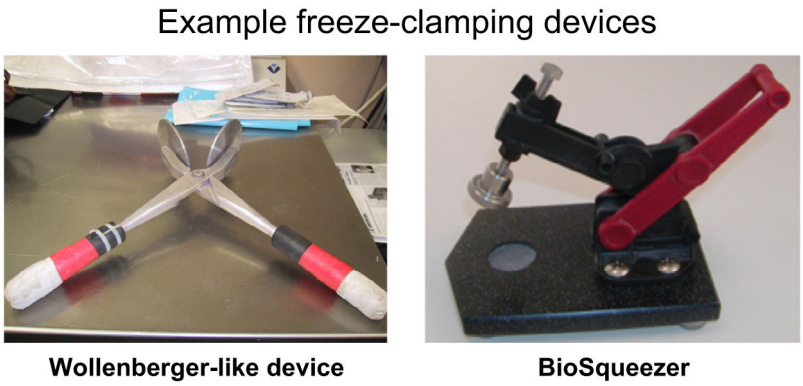

Fig. 13.

Example freeze-clamping devices. A Wollenberger-like device [385] is routinely used in our laboratory for rapid freezing of human and animal tissues to quench metabolism. A commercially available freeze-clamping device for small tissue freezing (BioSqueezer) is also shown (http://www.biosciencetechnology.com/product-releases/2010/12/snap-freeze-tissue-clamp).

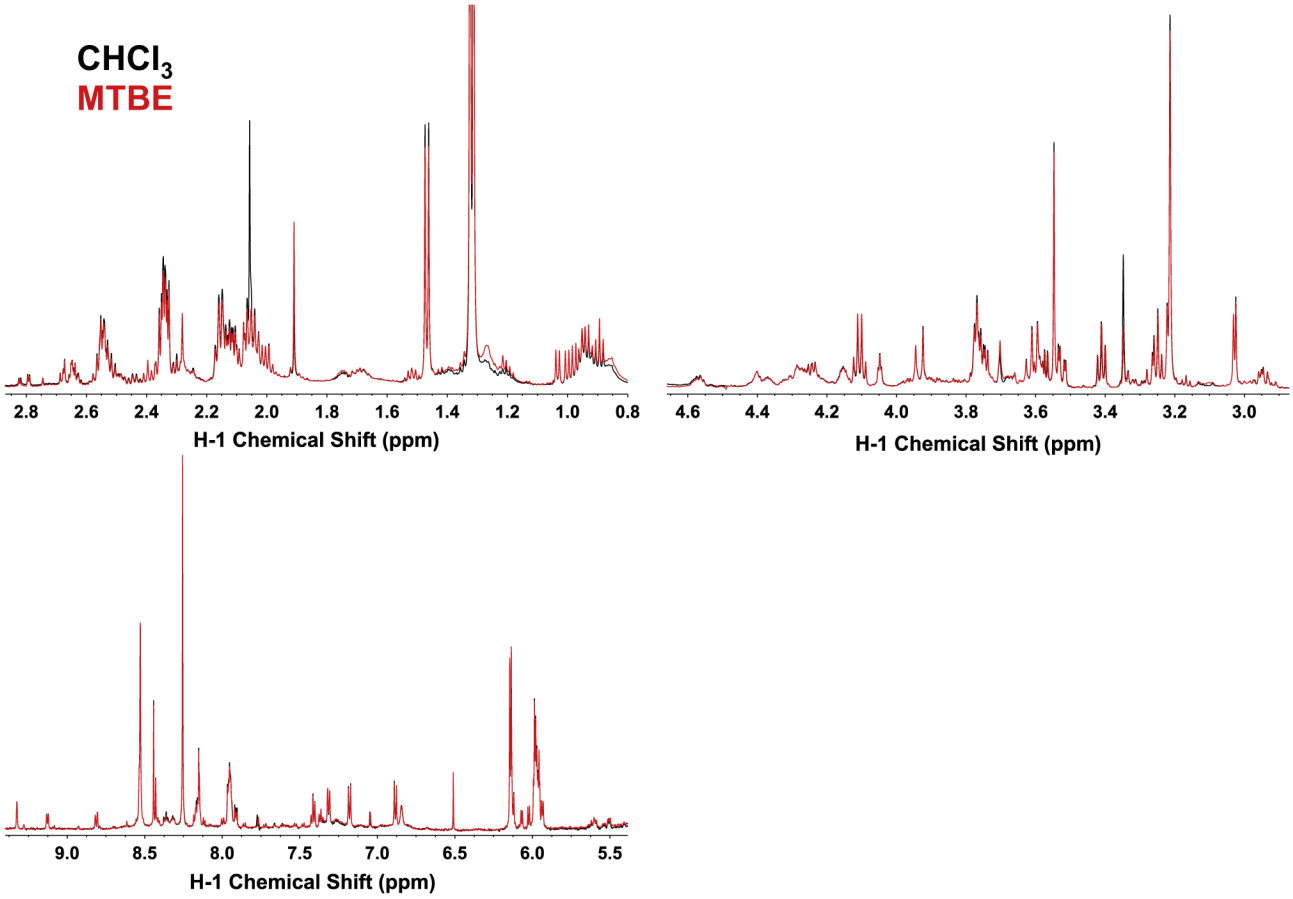

Fig. 14.

MTBE-based extraction gives comparable ^{1}H NMR profile of polar metabolites as $CHCl_3$-based extraction. An NSCLC patient-derived lung cancer cell line (PDLC216) was quenched in cold CH_3CN before extraction of polar and non-polar metabolites by the addition of H_2O and $CHCl_3$ or MTBE. The solvent composition for the $CHCl_3$ extraction method was CH_3CN:H_2O:$CHCl_3$ (2:1.5:1) for the 1st extraction and $CHCl_3$:methanol:butylated hydroxytoluene (2:1:1 mM) for the 2nd extraction. The solvent composition for the MTBE extraction method was CH_3CN:H_2O:$MTBE_3$ (2:1:3) for the 1st extraction and MTBE:methanol:H_2O (10:3:2.5) for the 2nd extraction.

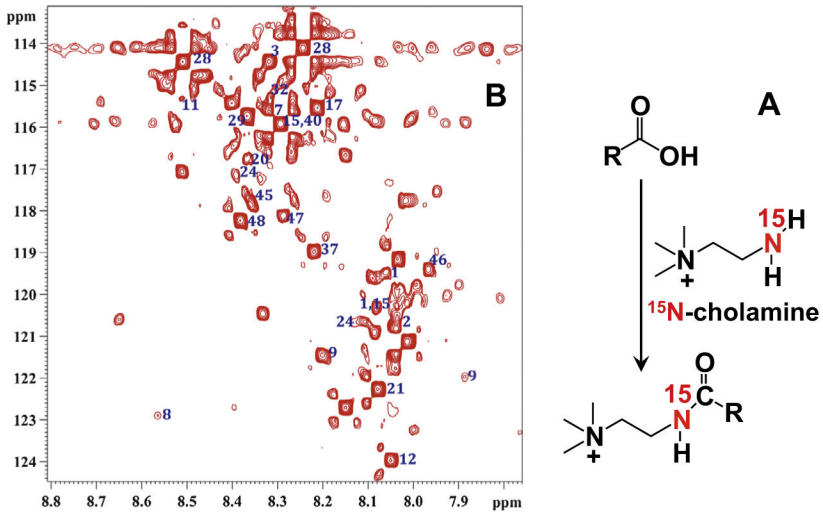

Fig. 15.

^{15}N-cholamine tagging of carboxyl groups enables their selective analysis in human serum by ^{1}H{^{15}N}-HSQC. The reaction of ^{15}N-cholamine with carboxylates is shown in (A) and the ^{1}H{^{15}N}-HSQC contour plot of a tagged human serum is illustrated in (B). (1) Aconitic acid; (2) adipic acid; (3) alanine; (7) aspartic acid; (8) betaine; (9) citric acid; (11) cystine; (12) formic acid; (15) glutamic acid; (17) glycine; (20) histidine; (21) 3-hydroxybutyric acid; (24) isocitric acid; (28) lactic acid; (29) leucine; (32) malic acid; (37) phenylalanine; (40) pyroglutamic acid; (45) threonine; (46) tryptophan; (47) tyrosine; (48) valine. Reprinted with permission from F. Tayyari, G.A. Gowda, H. Gu, D. Raftery, ^{15}N-cholamine–a smart isotope tag for combining NMR- and MS-based metabolite profiling, Anal Chem, 85, 8715–8721. Copyright (2013) American Chemical Society [199].

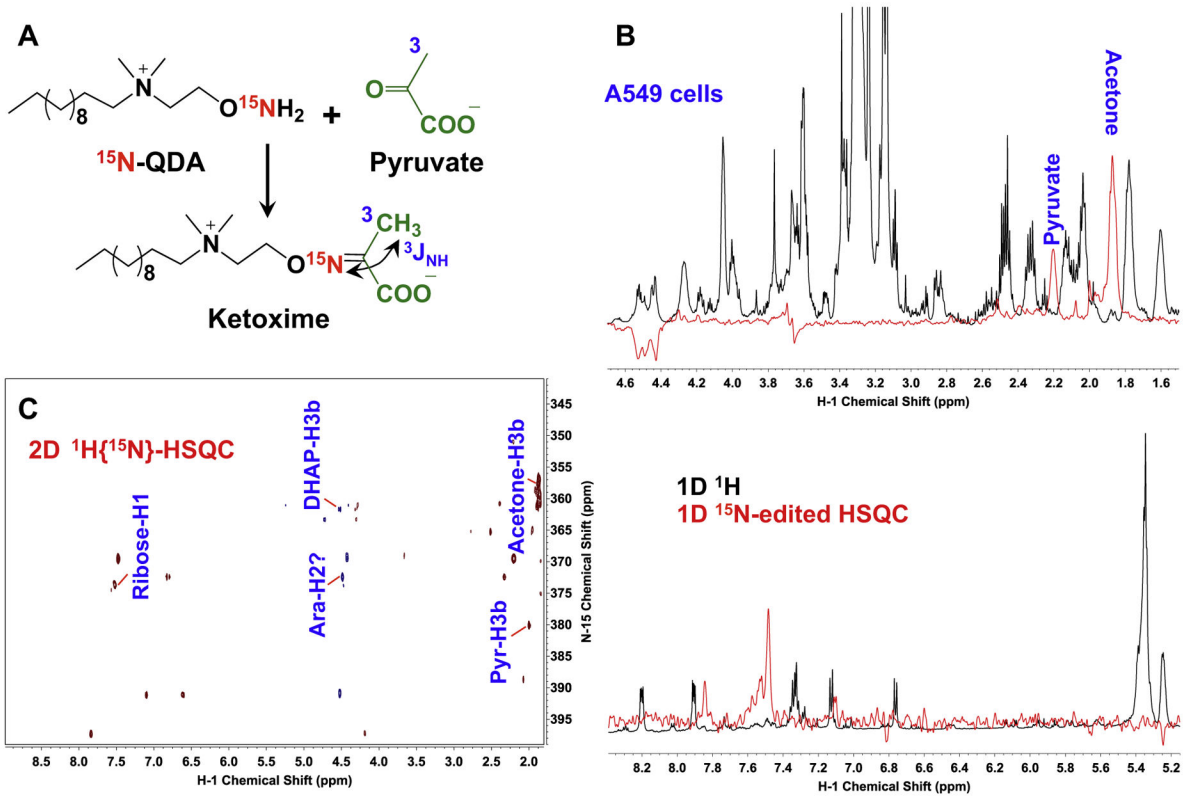

Fig. 16.

Carbonyl tagging by ^{15}N-QDA enables their selective analysis by ^{1}H{^{15}N}-HSQC. A549 cells were quenched and reacted in cold acetonitrile containing 0.3 mM ^{15}N-QDA (N-(2-^{15}Naminooxyethyl)-N,N-dimethyl-1-dodecylammonium) to form QDA adducts of carbonylated metabolites such as pyruvate in (A). The tagged extract was analyzed by both 1D (B) and 2D ^{15}N-edited HSQC (C, adapted from Fig. 5 of A.N. Lane, S. Arumugam, P.K. Lorkiewicz, R.M. Higashi, S. Laulhé, M.H. Nantz, H.N.B. Moseley, T.W. M. Fan, Chemoselective detection and discrimination of carbonyl-containing compounds in metabolite mixtures by ^{1}H-detected ^{15}N nuclear magnetic resonance, Magnetic Resonance in Chemistry, 53 (2015) 337–343 with permission from John Wiley & Sons [142]) at 14.1 Tesla. DHAP: dihydroxyacetone-3-phosphate; Pyr: pyruvate; Ara: arabinose.

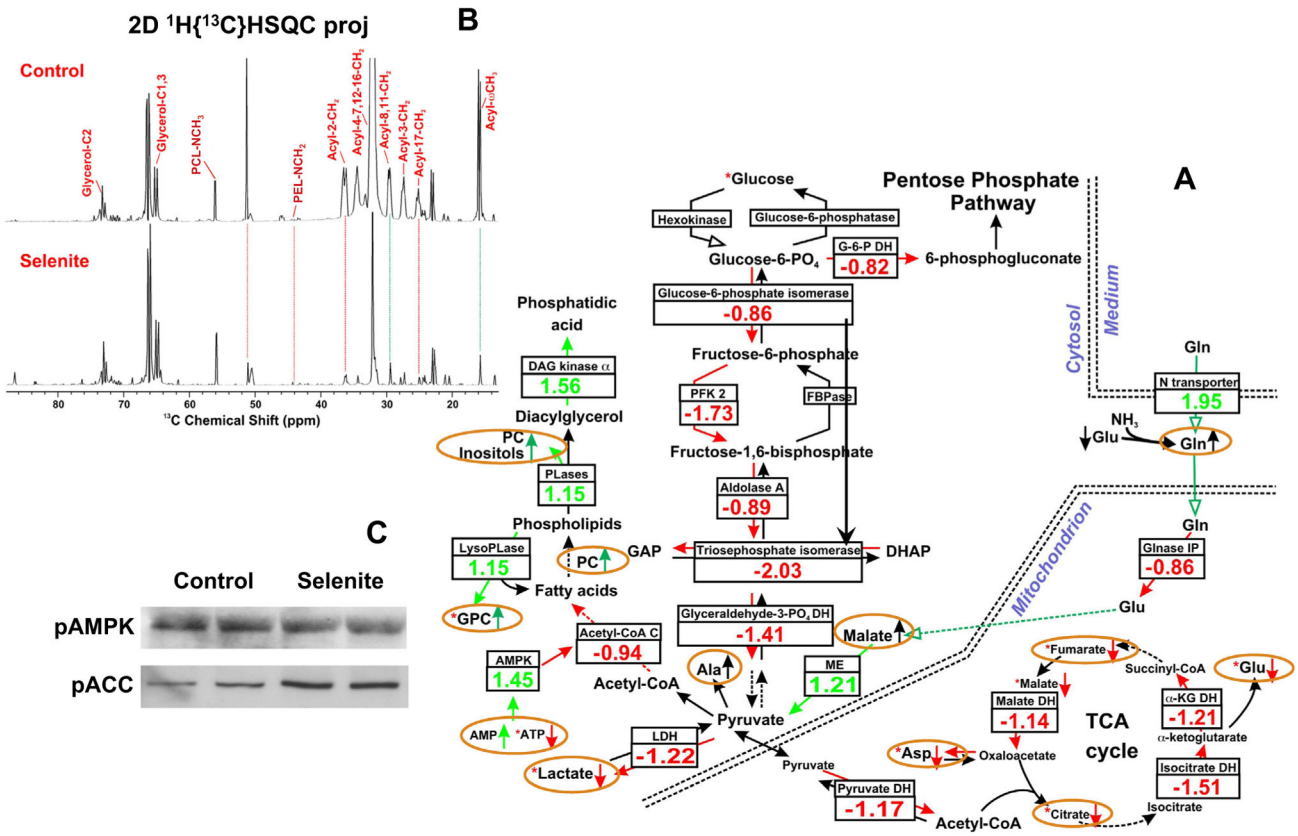

Fig. 17.

Metabolomics-edited transcriptomic analysis for selenite-induced perturbations of glycolysis, pentose phosphate pathway, TCA cycle, glutaminolysis, and fatty acid metabolism in A549 cells. Panel (A) shows the pathways perturbed in selenite-treated A549 cells, based on SIRM analysis, which was used to interrogate parallel transcriptomic data for relevant gene expression changes. The signal log ratio of selenite treated to control mRNA expression is listed below each protein into which the mRNA was translated. Negative and positive values indicate a decrease and increase in expression, respectively. → indicates down regulation of genes, inhibition of protein activity, or depletion of ^{13}C-labeled metabolites (denoted by *). → indicates up regulation of genes, activation of protein activity, or accumulation of labeled metabolites. → indicates trace reactions, transport processes, and changes in concentration of unlabeled metabolites. The open green arrows indicate glutaminolysis of unlabeled Gln taken up from the medium and subsequent oxidation to generate unlabeled malate. Dashed arrows indicate multiple reaction steps. Acetyl-CoA C: Acetyl-CoA carboxylase (ACC); AMPK: 5′-AMP-activated protein kinase; DAG: diacylglycerol; DHAP: dihydroxyacetone phosphate; FPBase: fructose bisphosphatase; Glnase IP: glutaminase interacting protein; G-6-P DH: glucose-6-phosphate dehydrogenase; GAP, glyceraldehyde-3-phosphate; GPC, glycerophosphorylcholine; α-KG DH: α-ketoglutarate dehydrogenase; LDH: lactate dehydrogenase; LysoPLase: lysophospholipase; ME: malic enzyme; Malate DH: malate dehydrogenase; N transporter: neutral amino acid transporter; OAA: oxaloacetate; PC: phosphorylcholine; PFK2: phosphofructokinase 2; PLases: phospholipases; Pyruvate DH: pyruvate dehydrogenase (adapted from [386] with

permission). Selenite-reduced fatty acyl synthesis is evident in the 1D ^{13}C projection spectrum of 2D $^{1}H\{^{13}C\}$-HSQC analysis of A549 lipids shown in (B). PCL: phosphatidylcholine lipids; PEL: phosphatidylethanolamine lipids. The Western blot analysis for the protein level of phosphorylated or inactivated ACC (pACC) and AMPK (pAMPK) in response to selenite treatment is shown in (C), where selenite-induced increase in pACC and decrease in pAMPK levels relative are evident. This data suggests inactivation of AMPK by phosphorylation underlies enhanced ACC phosphorylation or inactivation by AMP.

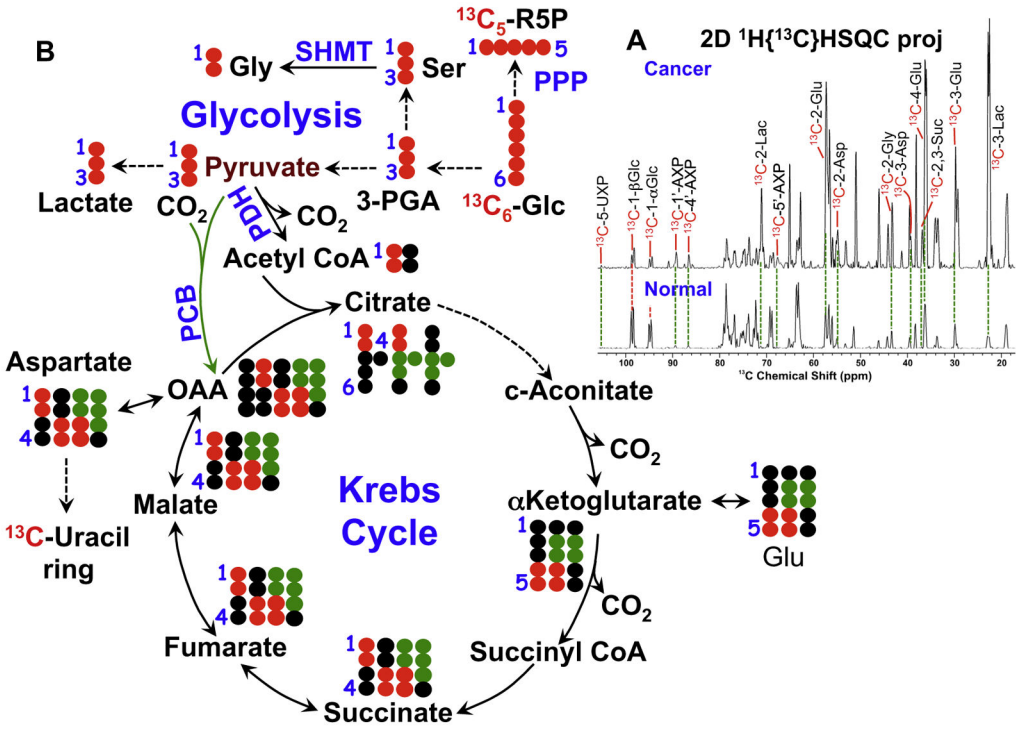

Fig. 18.

2D $^1H\{^{13}C\}$-HSQC NMR analyses reveal *in vivo* metabolic reprogramming in human lung tumor tissues resected from an NSCLC patient infused with $^{13}C_6$-glucose (adapted from Fan et al. [97]). U-$^{13}C_6$-glucose was infused into the patient 2–3 h prior to resection and cryopreservation of cancer and surrounding benign (normal) tissues. The liquid N_2-frozen tissues were pulverized and extracted for polar metabolites, which were analyzed by 2D $^1H\{^{13}C\}$-HSQC at 14.1 T. The 1D ^{13}C projection spectrum is shown in (A), where the increase in ^{13}C abundance of various metabolites at different carbon positions is evident in cancer versus paired benign tissues. The pathway scheme in (A) traces ^{13}C atoms from $^{13}C_6$-glucose into intermediates of glycolysis, pentose phosphate pathway (PPP), the Krebs cycle, Ser-Gly pathway, and uracil biosynthesis. Based on this scheme and ^{13}C abundance data in (A), the cancer tissue displays enhanced capacity for all of these pathways. ●: ^{12}C; ●, ●: respective ^{13}C tracing of pyruvate dehydrogenase (PDH) or pyruvate carboxylase (PCB)-initiated Krebs cycle reactions; Lac: lactate; GSH/GSSG: reduced/oxidized glutathiones; Glc: glucose; G6P: glucose-6-phosphate; UDPGGlcNAc: UDP-N-acetylglucosamine; UDPG: UDP-glucose; UXP: uracil nucleotides; AXP: adenine nucleotides; SHMT: serine hydroxymethyl transferas.

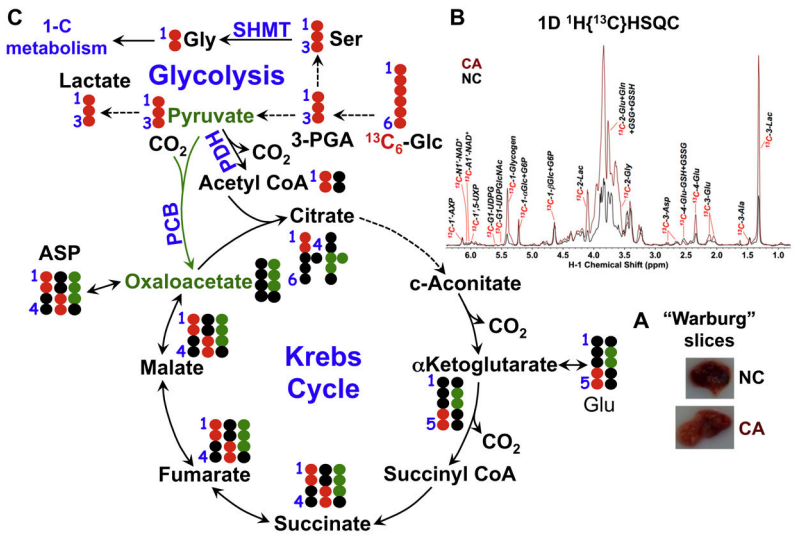

Fig. 19.

NSCLC tissue slices maintain distinct metabolic reprogramming. Paired cancerous (CA) and non-cancerous (NC) lung tissues (A) freshly resected from an NSCLC patient were treated with U-$^{13}C_6$-glucose for 24 h at 37 °C/5% CO_2. The tissue extracts obtained were analyzed by 1D $^1H\{^{13}C\}$-HSQC at 14.1 T (B). The elevated buildup of various ^{13}C metabolites in CA versus NC tissues is consistent with enhanced glycolysis (cf. ^{13}C-Lac), the Krebs cycle initiated by PDH (^{13}C-4-Glu) or PCB (^{13}C-2 or 3-Glu), onecarbon metabolism (^{13}C-2-Gly), and pentose phosphate pathway/nucleotide biosynthesis (^{13}C-1′-AXP, (^{13}C-N1′ or A1′-NAD^+), as depicted in ^{13}C tracing of these pathways in (B). Such distinct metabolic reprogramming in CA lung tissue slices recapitulates that of human lung cancer tissues *in vivo* (cf. Fig. V.B.2). See Fig. V.B.2 for abbreviations.

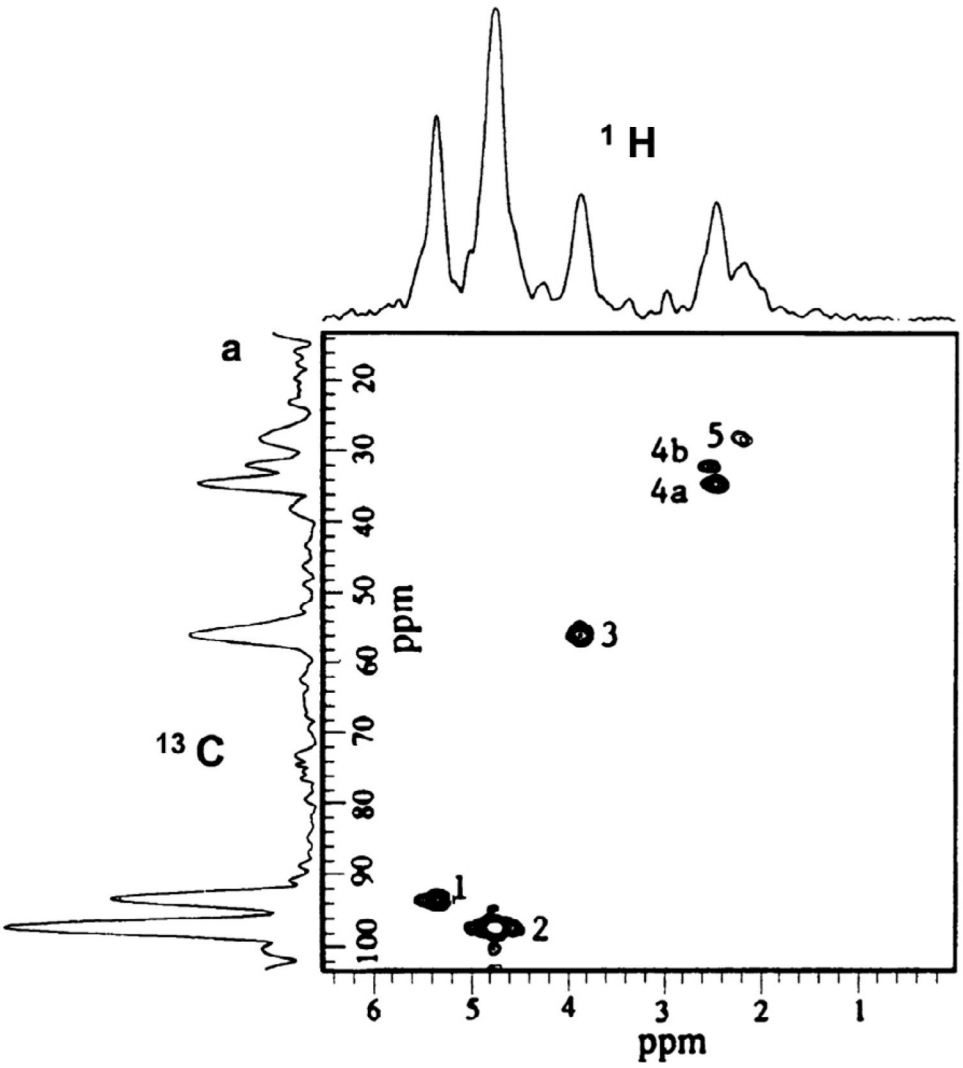

Fig. 20.

In vivo 2D $^{1}H\{^{13}C\}$ge-HMQC analysis of cat brain. The ^{13}C-edited 2D ^{1}H spectrum acquired *in vivo* from a cat brain resolves resonances of ^{13}C-4-Glu (4a) from ^{13}C-4-Gln (4b), which cannot be achieved with 1D ^{1}H methods. Also resolved are resonances of ^{13}C-3-Glu/Gln (5), ^{13}C-2-Glu/Gln (3), ^{13}C-1-α-glucose, and ^{13}C-1-β-glucose; the latter three would be difficult to detect without the better water suppression afforded by the 2D method [260]. Excerpted from MAGMA, 17 (2004) 317–338, *In vivo* 2D magnetic resonance spectroscopy of small animals, P. Meric, G. Autret, B.T. Doan, B. Gillet, C. Sebrie, J.C. Beloeil, Fig. 14a with kind permission from Springer Science and Business Media.

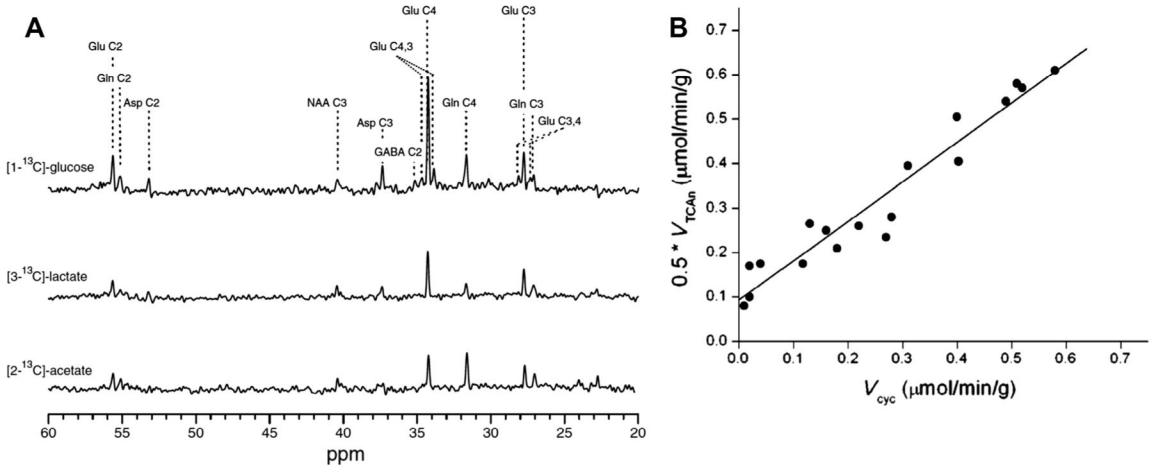

Fig. 21.

In vivo 1D ^{13}C NMR analysis of human brain metabolism. The ^{13}C spectra in (A) were acquired *in vivo* from the midline occipital/parietal lobe of a human volunteer infused with $^{13}C_1$-1-glucose, $^{13}C_1$-3-lactate, or $^{13}C_1$-2-acetate. The differences in ^{13}C incorporation from these tracer substrates into Glu and Gln are evident. With glucose and lactate as precursors, a major fraction of ^{13}C appeared in Glu C4, which is consistent with primary location of glucose and lactate metabolism in brain neurons. In contrast, the acetate tracer led to much higher ^{13}C enrichment in Gln C4, which supports acetate metabolism via the Krebs cycle in brain astrocytes. Based on the time course analysis of *in vivo* ^{13}C NMR data such as those in (A), the rate of neuronal Krebs cycle (V_{TCAn}) and Glu/Gln cycle (V_{cyc}) can be estimated as a function of brain electrical activity. Panel (B) plots V_{TCAn} versus V_{cyc} from 11 studies and shows a 1:1 linear relationship. These results indicate that the Glu/Gln cycle for the Gln neurotransmitter production constitutes a major metabolic flux for brain energy metabolism and that >80% of neuronal oxidative ATP production is coupled to neuronal signaling [262]. Reproduced from Figs. 2 and 3 of D.L. Rothman, H.M. De Feyter, R.A. de Graaf, G.F. Mason, K.L. Behar, ^{13}C MRS studies of neuroenergetics and neurotransmitter cycling in humans, NMR in biomedicine, 24 (2011) 943–957 with permission from John Wiley & Sons Inc.

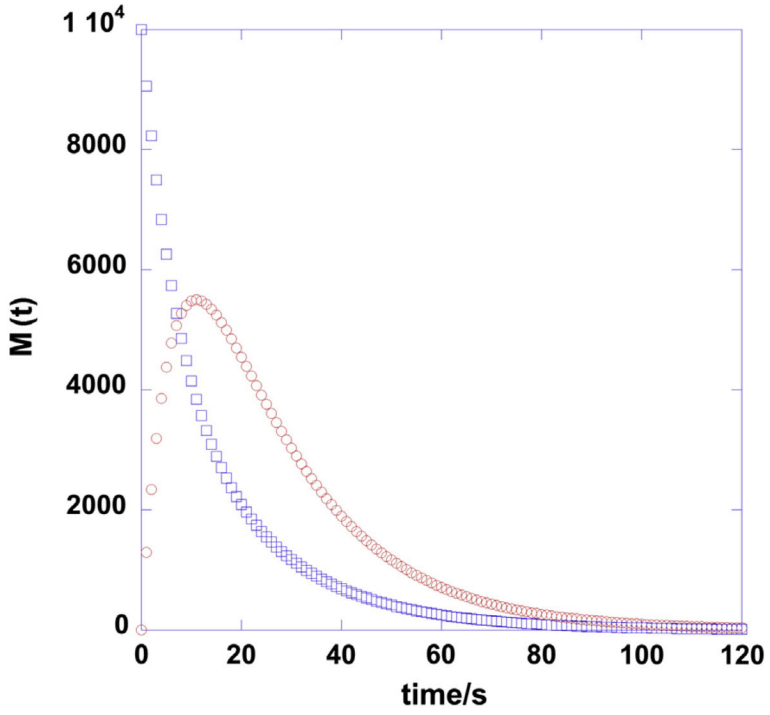

Fig. 22.

Two site exchange. Magnetization time courses were calculated for two-site exchange A ⇔ B with $k_1 = k_{-1} = 0.05\ s^{-1}$ and T_1 values for A and B of 20 s. Blue squares = M_A; red circles = M_B. The equilibrium and initial magnetizations of A were set to unit and 10,000, respectively. The modified Bloch equations (3A) and (3B) were solved as described in the text, and the curves were generated using Kaleidagraph (Synergy Software). The solutions to this system are: $M_B(t) = k_1\langle M_A\rangle[\exp(\lambda_1 t) - \exp(\lambda_2 t)]/(\lambda_1 - \lambda_2)$.

$M_A(t)=[(\varepsilon-\lambda_2(M_A^0-\langle M_A\rangle))\exp(\lambda_1 t)+(\lambda_1(M_A^0-\langle M_A\rangle-\varepsilon)\exp(\lambda_2 t)]/(\lambda_1-\lambda_2)$. $2\lambda_{1,2} = -\rho_A + \rho_B + k_1 + k_{-1} \pm [(\rho_A + \rho_B + k_1 + k_{-1})^2 - 4(\rho_A\rho_B + \rho_A k_1 + \rho_B k_{-1})]$.

$\varepsilon=-(\rho_A+k_1)M_A^0+k_{-1}\langle M_B\rangle+\rho_A\langle M\rangle$. where M_A^0 is the initial (hyperpolarized) magnetization of A.

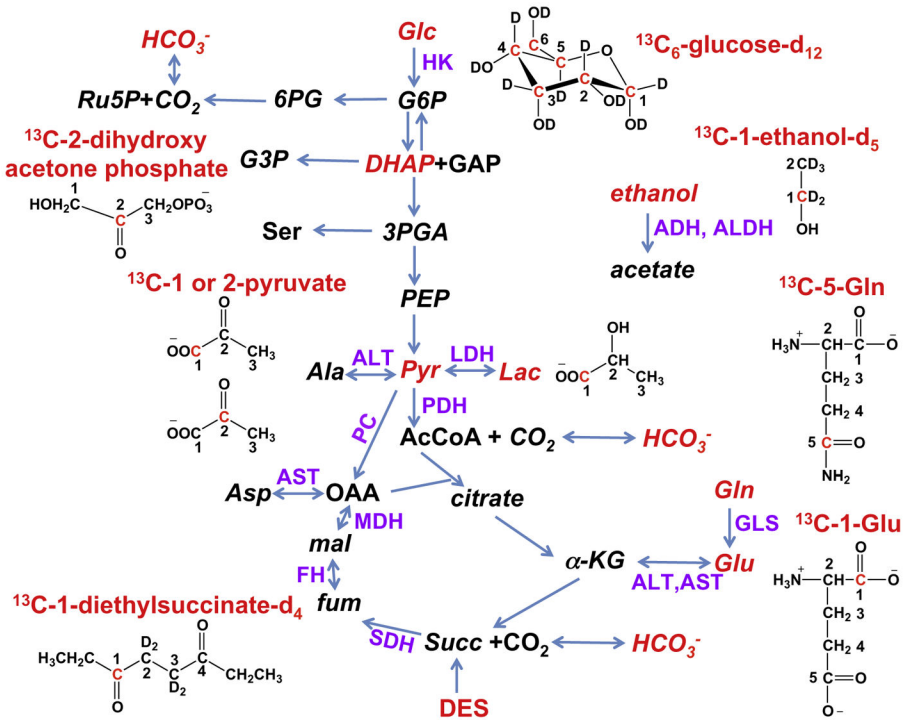

Fig. 23.

Central Metabolism probed by hyperpolarized ^{13}C enriched precursors. Metabolites in red have been ^{13}C hyperpolarized at one or more atoms, and those in italics have been observed as products of hyperpolarized substrates via different pathways. These include glucose (Glc) oxidation to pyruvate (Pyr) via glycolysis, subsequent pyruvate metabolism via the Krebs cycle and lactic fermentation, anaplerosis via pyruvate carboxylation to oxaloacetate (OAA), and glucose metabolism via the pentose phosphate pathway from glucose-6-phosphate (G6P), 6-phosphogluconate (6PG) to ribulose-5-phosphate (Ru5P). Also shown are anaplerosis via glutaminolysis or Gln conversion to Glu and then to α-ketoglutarate (αKG) for entry into the Krebs cycle and ethanol oxidation to acetate via alcohol dehydrogenase (ADH) and aldehyde dehydrogenase (ALDH). DHAP: dihydroxyacetone phosphate; GAP: glyceraldehyde-3-phosphate; 3PGA: 3-phosphoglycerate; PEP: phosphoenolpyruvate; Lac: lactate, Succ succinate; DES: diethylsuccinate; fum: fumarate; mal: malate; HK: hexokinase; LDH: lactate dehydrogenase; ALT: alanine pyruvate aminotransferase; PDH: pyruvate dehydrogenase; SDH: succinate dehydrogenase; FH: fumarate hydratase; MDH: malate dehydrogenase; AST: aspartate/oxalacetate aminotransferase; PC: pyruvate carboxylase; GLS glutaminase.

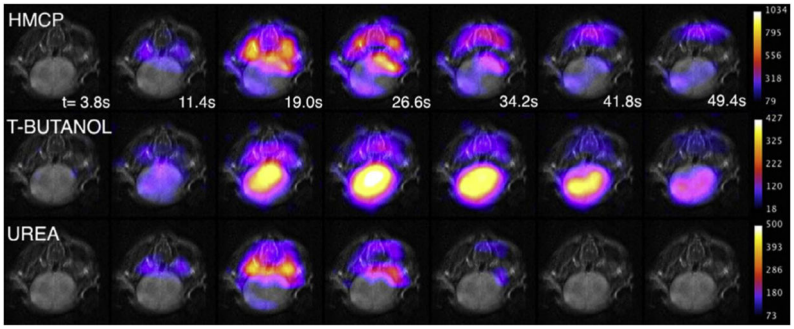

Fig. 24.

Magnetic resonance imaging of three co-hyperpolarized ^{13}C agents in mouse brain. ^{13}C-Urea, ^{13}C-1-hydroxymethylcyclopropane (HMCP), and ^{13}C-2-*t*-butanol were simultaneously hyperpolarized before infusing into normal and transgenic TRAMP mice bearing prostate cancer. A multiband frequency encoding and balanced steady-state free precession (SSFP) MRI method was used to acquire ^{13}C images of the dynamic distributions of these three agents in mouse tissues. The axial tripolarized images of mouse brain (color) are overlaid on the T_2 images (gray), which show the remarkable speed at which *t*-butanol crosses the blood–brain barrier, unlike urea and HMCP A parallel set of dynamic images of prostate tumor tissues compared with those of normal tissues enabled measurement of tissue permeability for the three agents. Tumor tissues were shown to have a higher permeability to urea and HMCP than normal brain and liver. Such a capability can be readily extended to investigating the efficiency of therapeutic drug delivery to target tumor tissues [343]. Reproduced from Fig. 5 in C. von Morze, R.A. Bok, G.D. Reed, J.H. Ardenkjaer-Larsen, J. Kurhanewicz, D.B. Vigneron, Simultaneous multiagent hyperpolarized (13)C perfusion imaging, Magn Reson Med, 72 (2014) 1599–1609. With permission from John Wiley & Sons, Inc.